

---

Dissertations, Theses, and Masters Projects

Theses, Dissertations, & Master Projects

---

2000

## Low damage processing and process characterization

Xianmin Tang

*College of William & Mary - Arts & Sciences*

Follow this and additional works at: <https://scholarworks.wm.edu/etd>



Part of the [Electrical and Computer Engineering Commons](#), [Industrial Engineering Commons](#), and the [Plasma and Beam Physics Commons](#)

---

### Recommended Citation

Tang, Xianmin, "Low damage processing and process characterization" (2000). *Dissertations, Theses, and Masters Projects*. Paper 1539623979.

<https://dx.doi.org/doi:10.21220/s2-nzw7-th19>

This Dissertation is brought to you for free and open access by the Theses, Dissertations, & Master Projects at W&M ScholarWorks. It has been accepted for inclusion in Dissertations, Theses, and Masters Projects by an authorized administrator of W&M ScholarWorks. For more information, please contact [scholarworks@wm.edu](mailto:scholarworks@wm.edu).

## **INFORMATION TO USERS**

**This manuscript has been reproduced from the microfilm master. UMI films the text directly from the original or copy submitted. Thus, some thesis and dissertation copies are in typewriter face, while others may be from any type of computer printer.**

**The quality of this reproduction is dependent upon the quality of the copy submitted. Broken or indistinct print, colored or poor quality illustrations and photographs, print bleedthrough, substandard margins, and improper alignment can adversely affect reproduction.**

**In the unlikely event that the author did not send UMI a complete manuscript and there are missing pages, these will be noted. Also, if unauthorized copyright material had to be removed, a note will indicate the deletion.**

**Oversize materials (e.g., maps, drawings, charts) are reproduced by sectioning the original, beginning at the upper left-hand corner and continuing from left to right in equal sections with small overlaps. Each original is also photographed in one exposure and is included in reduced form at the back of the book.**

**Photographs included in the original manuscript have been reproduced xerographically in this copy. Higher quality 6" x 9" black and white photographic prints are available for any photographs or illustrations appearing in this copy for an additional charge. Contact UMI directly to order.**

**UMI<sup>®</sup>**

**Bell & Howell Information and Learning  
300 North Zeeb Road, Ann Arbor, MI 48106-1346 USA  
800-521-0600**



# Low Damage Processing and Process Characterization

---

A Dissertation

Presented to The Faculty of the Department of Applied Science  
The College of William and Mary

In Partial Fulfillment  
Of the Requirements for the Degree of  
Doctor of Philosophy

---

By

**Xianmin Tang**

May 2000

UMI Number: 9982021

**UMI**<sup>®</sup>

---

**UMI Microform 9982021**

**Copyright 2000 by Bell & Howell Information and Learning Company.**

**All rights reserved. This microform edition is protected against  
unauthorized copying under Title 17, United States Code.**

---

**Bell & Howell Information and Learning Company  
300 North Zeeb Road  
P.O. Box 1346  
Ann Arbor, MI 48106-1346**

**Copyright**

**by**

**Xianmin Tang**

**2000**

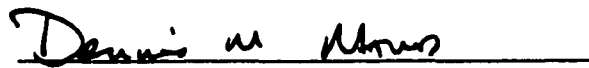
## APPROVAL SHEET

This dissertation is submitted in partial fulfillment  
of the requirements for the degree of

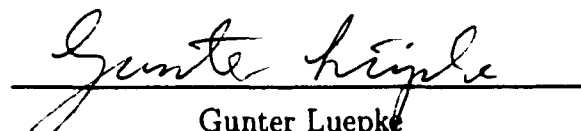
Doctor of Philosophy.

  
Xianmin Tang

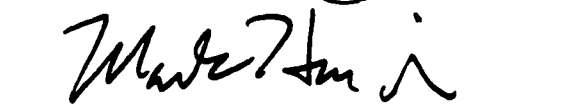
Approved, May 2000

  
Dennis Manos

  
Brian Holloway

  
Gunter Luepke

  
Anne Reilly

  
Mark Hinders

Dedicated to my parents  
and  
my wife



# Contents

<b>Acknowledgments</b>	<b>ix</b>
<b>List of Figures</b>	<b>xi</b>
<b>List of Tables</b>	<b>xv</b>
<b>Abstract</b>	<b>xv</b>
<b>Chapter 1 Introduction</b>	<b>2</b>
1.1 Why We Study Charge-free Processing . . . . .	2
1.2 Charge-Free Sources . . . . .	4
1.2.1 Free Expansion Gas Sources . . . . .	5
1.2.2 Plasma Source Neutralized Streams . . . . .	6
1.2.3 Charge-exchange Sources . . . . .	6
1.3 Review of Operation Mechanism for the Low-Energy Neutral Sources	7
1.3.1 Plasma . . . . .	8
1.3.2 High Density Plasma Sources . . . . .	11
1.3.3 Sheath Theory . . . . .	13
1.3.4 Neutralization Mechanism . . . . .	16
1.4 Previous work - Monte Carlo Simulation . . . . .	19
1.5 Purpose of this Work . . . . .	20
1.6 Organization of Dissertation . . . . .	21
<b>Chapter 2 Plasma Discharge Characterization</b>	<b>23</b>
2.1 Introduction . . . . .	23
2.1.1 Langmuir probe studies . . . . .	23
2.1.2 Optical Emission Studies . . . . .	25
2.1.3 Actinometry . . . . .	29

2.2	Experimental Setup . . . . .	30
2.3	Results and Discussion . . . . .	32
2.3.1	Langmuir probe studies . . . . .	32
2.3.2	Optical Emission Studies . . . . .	35
2.4	Summary . . . . .	47
<b>Chapter 3 Time-resolved electrostatic probe studies of a pulsed inductively coupled plasma</b>		<b>48</b>
3.1	Introduction . . . . .	48
3.2	Experiment . . . . .	51
3.2.1	Setup . . . . .	51
3.2.2	Probe theory and data analysis . . . . .	55
3.3	Results and Discussion . . . . .	60
3.3.1	Langmuir probe measurement results for cw rf plasma . . . . .	60
3.3.2	Single probe measurement for pulsed plasma . . . . .	60
3.3.3	Double probe measurement for pulsed plasma . . . . .	64
3.4	Summary . . . . .	75
<b>Chapter 4 Global Average Simulation of a Inductively-Coupled Plasma Source</b>		<b>76</b>
4.1	Introduction . . . . .	76
4.2	Spatially Averaged Simulation Model Setup . . . . .	78
4.2.1	Assumptions . . . . .	78
4.2.2	Steady-state model . . . . .	80
4.2.3	Pulsed Operation . . . . .	89
4.3	Results and Discussion . . . . .	90
4.3.1	CW plasma . . . . .	90
4.3.2	Pulse-Modulated plasma . . . . .	94
4.4	Summary . . . . .	101
<b>Chapter 5 Stripping and cleaning of photo-resists using low energy neutrals</b>		<b>102</b>
5.1	Introduction . . . . .	102
5.2	Experiment . . . . .	104
5.2.1	Equipment setup . . . . .	104
5.2.2	Experiment methods . . . . .	107
5.3	Results and Discussion . . . . .	108

5.3.1	Neutral cleaning with the collimator . . . . .	108
5.3.2	Cleaning rate measurements . . . . .	111
5.3.3	Trench cleaning studies by the neutral beam . . . . .	118
5.4	Summary . . . . .	121

**Chapter 6 Neutral Stream Characterization of a Surface Reflection**

	<b>Materials Processing Source</b>	<b>122</b>
6.1	Introduction . . . . .	122
6.2	Experiment Setup and Methods . . . . .	125
6.2.1	Vacuum system . . . . .	125
6.2.2	Torsion balance . . . . .	126
6.3	Theory of torsion balance operation . . . . .	128
6.3.1	Suspension wire rotation angle measurement . . . . .	131
6.3.2	Torsion constant calibration . . . . .	132
6.3.3	Torsion balance damping . . . . .	133
6.4	Results and Discussion . . . . .	134
6.4.1	Neutral Energy and Flux Measurement . . . . .	134
6.5	Summary . . . . .	141

**Chapter 7 Process damage assessment of a low energy inductively coupled plasma-based neutral source**

		<b>142</b>
7.1	Introduction . . . . .	142
7.2	Experiment . . . . .	144
7.2.1	CW, Pulsed ICP plasma setup and Surface reflection neutral-ization source . . . . .	144
7.2.2	Damage Measurement . . . . .	144
7.3	Results . . . . .	146
7.3.1	Class 1: Neutral Damage Measurements without PMMA overlayer . . . . .	146
7.3.2	Class 2: Damage with PMMA overlayer . . . . .	151
7.4	Discussion . . . . .	152
7.4.1	Class 1 . . . . .	152
7.4.2	Class 2 . . . . .	156
7.5	Summary . . . . .	157

<b>Chapter 8 Conclusion</b>	<b>158</b>
8.1 Summary . . . . .	158
8.2 Future Work . . . . .	159
<b>Bibliography</b>	<b>161</b>
<b>Vita</b>	<b>181</b>

# Acknowledgments

First and foremost, I would like to sincerely thank my advisor Dr. Dennis Manos for these years of patient work with me. I was exceptional lucky to have him as my advisor. His overwhelming knowledge, scientific tenacity, and optimism contributed invaluable to this work. I am also in debted to his constant willingness to help.

I would like to thank Dr.Q. Wang in Keithley Instruments, Inc. for his unconditional help to my research. I am also indebted to Dr.Chris Nichols and to Dr.Agus Ananda for their help with my research. Special thanks also goes to Dr.James Stevens of Sandia labs, Dr.Steven Rossnagel and Dr.Paul Muller of IBM. Dr.Steve Cook and Dr.Mark Hoffbauer of Los Alamos Labs are owed for their contribution in building the torsion balance. Two REU students, Andrew Cady and Ed Cox also put their efforts into allowing this project to succeed. I would also like express my appreciation to Karen Berquest and Richard Proper, who were always willing to help.

Thank my committee memebers, Dr.Mark Hinders, Dr.Brian Holloway, and Dr.Gunter Lupeke of Applied Science, and Dr.Anne Reilly of Physics for agreeing to serve. I especially appreciate their career advice and encouragement during my stay here. I would also like to thank my friends here, Dr.Tom Venhaus, Dr.Joseph

Ametepe, Jessie Diggs, Lingling Wu, Dr. Jim Mckeen, Eugene Malyarenko, Shelly Huang, Adam Friedeman, and Caro Kalil for all the fun we have had together.

Thanks also go to Kathee Card and Marcy Borges for taking care of all sorts of problems for me .

Thank my parents for bringing me into this wonderful world and guiding me all these years. I would also thank my brother, Dr. X.Z. Tang and my sister-in-law, Tian Liu, whom I can always count on. The most special thanks go to my wife, Min Xiang. Without her, I would never be able to achieve this.

# List of Figures

1.1 Morphological damage by non-ideal processing technology (adopted from [2]) . . . . .	3
1.2 The schematic drawing of the neutral stream generation . . . . .	7
1.3 Plasma density Log $n_e$ Vs Electron temperature Log $T_e$ . $\lambda_{de}$ , Debye length (adopted from[15]) . . . . .	9
1.4 Maxwellian energy distribution function . . . . .	10
1.5 Schematic drawings of different high density plasma sources (adopted from [16]) . . . . .	12
1.6 Schematic drawing of plasma sheath in contact with a wall, $\lambda_i$ , ion mean free path and $\Phi_p$ , plasma potential. . . . .	14
1.7 Auger surface neutralization scheme . . . . .	17
1.8 Resonance surface neutralization scheme . . . . .	17
2.1 Single Langmuir probe characteristic I-V curves . . . . .	24
2.2 Schematic drawing of the photon emission . . . . .	26
2.3 The schematic drawing of the set up for Langmuir probe and OES studies	31
2.4 Plasma density as a function of the discharge pressure from single probe, Ar discharge, 500W . . . . .	33
2.5 Electron temperature as a function of the discharge pressure from single probe, Ar discharge, 500W . . . . .	33
2.6 Plasma density as a function of the discharge power in Ar discharges . . . .	34
2.7 Electron temperature as a function of the rf power in Ar discharges . . . .	34
2.8 Typical Ar discharge spectrum . . . . .	36
2.9 Energy diagram of Ar atoms . . . . .	36
2.10 $O_2$ discharge spectrum at 3.56mTorr, 400 W . . . . .	38
2.11 The ratio of $O_{777}/Ar_{750}$ intensity as a function of rf power . . . . .	39
2.12 Electron Temperature as a function of the rf power from OES studies . . . .	40

2.13	The ratio of $O_{777}/Ar_{750}$ intensity as a function of rf power from actinometry result . . . . .	41
2.14	$Ar + O_2$ plasma as a function of the oxygen composition in the source region (500W, 6.74mTorr) . . . . .	42
2.15	Optical emission spectra of $Ar + O_2 + CF_4$ plasmas as a function of the discharge gas composition . . . . .	44
2.16	Optical emission spectra of $Ar + O_2$ plasmas as a function of the reflector bias	46
3.1	Schematic drawings of Langmuir probe setup for the pulsed plasma characterization, (a) single probe. (b) double probe. . . . .	52
3.2	Plasma density (A) and electron temperature (B) from double probe measurements for the cw Ar Plasma at 7.8 mTorr with two fitting methods. . . . .	61
3.3	Single Langmuir probe measurements of $n_e, T_e$ for an Ar pulsed plasma at 1000Hz.(average power: 65W, duty cycle: 50%, 7.8mTorr. Note: The coil current scale is arbitrary) . . . . .	62
3.4	Calculated plasma density as a function of pulse frequency from the double probe measurement. (a) 200 Hz, (b) 1kHz,(c) 5kHz, and (d) 10 kHz. Note: the coil current scale is arbitrary. . . . .	65
3.5	Calculated electron temperature as a function of pulse frequency from the double probe measurement. (a) 200 Hz, (b) 1kHz,(c) 5kHz, and (d) 10 kHz. Note: the coil current scale is arbitrary. . . . .	67
3.6	Time averaged plasma density as a function of the pulse frequency from double probe measurements (65 W,7.8mTorr, 50 % duty cycle) . . . . .	69
3.7	Measurements of double probe ion saturation current as a function of duty cycles with the same time-averaged power.(60W,7.8mTorr,Ar plasma) . . . . .	73
3.8	Two cycles of time profiles of $I_{sat}$ at various locations in a 65 W pulsed plasma having 64 % duty cycle.Numbers 1-5 represent the radial positions that the data are collected.(Ar plasma, 7.8 mTorr) . . . . .	74
4.1	Calculated positive ion density, $\times 10^{16}m^{-3}$ as a function of cw rf power for $Ar + O_2$ discharge, $Ar/O_2=1:10$ , 8mTorr . . . . .	90
4.2	Negative ion density, $\times 10^{16}m^{-3}$ as a function of cw rf power for $Ar + O_2$ discharge . . . . .	92
4.3	Calculated positive ion density, $\times 10^{16}m^{-3}$ as a function of discharge pressure for $Ar + O_2$ discharge,400 W . . . . .	93
4.4	Calculated negative ion density, $\times 10^{16}m^{-3}$ as a function of discharge pressure for $Ar + O_2$ discharge,400w . . . . .	93



4.5	Calculated electron temperature as a function of discharge pressure for Ar + O <sub>2</sub> discharge . . . . .	94
4.6	Calculated electron temperature transition for pulsed Ar discharges at 1kHz	95
4.7	Calculated particle density transition for pulsed Ar discharges at 1kHz . .	96
4.8	Time-average electron temperature as a function of duty cycles . . . . .	97
4.9	Time-average positive ion density as a function of duty cycles . . . . .	98
4.10	Time-average positive ion density as a function of pulse frequencies . . . .	98
4.11	Positive ion density as a function of pulse frequencies for Ar + O <sub>2</sub> mixture discharges,800W, 7.8mTorr . . . . .	99
4.12	Particle species density as a function of pulse frequencies in Ar+ O <sub>2</sub> mixture discharges,800 W,7.8mTorr . . . . .	100
4.13	Electron temperature transient in pulsed Ar+ O <sub>2</sub> mixture discharges with nonzero rf power input during the pulse-off period, pulse-on power is fixed at 600W. . . . .	100
5.1	Schematic drawing of the low energy neutral beam . . . . .	104
5.2	Schematic drawing of the ion and electron deflection neutral collimator . .	106
5.3	Comparison of the post-cleaned samples exposed to the neutral beams. 7 mTorr, Ar: 3.23sccm, O <sub>2</sub> :9.32sccm, bias:-15 V, 500W. Left sample was exposed without MgF <sub>2</sub> window, right sample was exposed with MgF <sub>2</sub> window.	109
5.4	XPS spectra of the cleaning results for Si wafers with patterned photoresist residue . . . . .	110
5.5	Stripping rates as functions of the rf power and total pressure.(Bias:-13.4 V, Ar: 3.66 sccm,O <sub>2</sub> : 8.23 sccm.) . . . . .	112
5.6	Neutral stream cleaning rates as a function of the rf power. (8mTorr,bias:-18.4V with collimator) . . . . .	113
5.7	PMMA removal rate as a function of the reflector bias.(7.8mTorr,Ar:3.66sccm, O <sub>2</sub> :8.23sccm) . . . . .	115
5.8	Calculated plasma potentials as a function of the rf power from the Langmuir probe data . . . . .	116
5.9	Scanning electron microscopy micrographs of trenches with different aspect ratios using the neutral source . . . . .	119
5.10	Angle-resolved XPS spectra of carbon peaks after neutral processing . . .	120
6.1	Vacuum system for the neutral beam characterization . . . . .	125
6.2	Schematic drawing of the torsion balance . . . . .	129

6.3	Neutral flux and energy measurement as a function of the rf power for pure Ar and $O_2$ plasmas. (Ar plasma:4.54mTorr; $O_2$ plasma:5.6mTorr, the reflector bias: -25 V) . . . . .	137
6.4	Ar neutral energy and flux as a function of the reflector bias in Ar plasmas ( 500 W, 5.77mTorr, 8.75 sccm) . . . . .	138
6.5	Etch yield as a function of neutral translational energy (reproduced with permission from J.Cross[107]) . . . . .	139
6.6	Comparison of the stripping rates as a function of the rf power.(stripping rates at different pressures were measured under following experimental conditions: the reflector bias: -13.4 V; Ar:3.66 sccm; $O_2$ : 8.33sccm) . . . . .	140
7.1	Quasi-static and high frequency CV results of neutral stream processing with and without the collimator. (a) As-received, (b) Sample with the collimator,(c)Sample without the collimator (130 w, $O_2$ , $V_b = -20$ V). . . . .	146
7.2	Quasi-static and high frequency CV results of exposure to neutral streams with without $MgF_2$ window (8.9mTorr, $O_2$ , $V_b = -20V$ , 5 min.) . . . . .	147
7.3	The flatband voltage shift and average fast neutral energy as a function of the reflector bias in neutral stream. (8.40mTorr, $O_2$ , 130 w, 5min) . . . . .	148
7.4	The positive effective charge increase and reflector current as a function of the rf power. ( $O_2$ , $V_{reflector} = -20$ V,8.90mTorr) . . . . .	149
7.5	Numerical values of positive charge density ( $\times 10^{-7} C/cm^3$ ) increase at different locations after neutral processing(130 w, bias:-20 V, 5min, note: this data has not been corrected for the contribution from UV photons) . . . . .	150
7.6	Quasi-static and high frequency CV results of the MOS samples exposed to neutral streams. (7.32mTorr,130 W,bias:-25V,(a) $O_2/Ar = 1 : 1$ , (b) $O_2$ ) . . . . .	151

# List of Tables

4.1	Reactions for Ar discharges included in the global model[43]	84
4.2	Reaction rate sets for Argon-Oxygen plasmas	86
7.1	Comparison of the photo-resist ashing process damage by different plasma processes	152

# Abstract

Two novel plasma sources (one neutral source and one pulsed inductively coupled plasma source) and their ashing process characterization were investigated. The primary goal of this dissertation was to characterize these source properties and develop corresponding applications. The study includes process damage assessment with these two sources and another continuous wave (13.56MHz) plasma source. A global average simulation of the pulsed discharges was also included.

The time-resolved plasma density and electron temperature from the double probe analysis were compared with single Langmuir probe results with sheath displacement corrections in pulsed discharges (200Hz  $\sim$  10kHz). The good agreement between the equivalent resistance method and nonlinear regression method indicates that the equivalent resistance method can be used effectively to analyze the double probe data. The transient behaviors of the plasma density and electron temperature are in accord with the simple model of the discharge.

The hyper-thermal neutral source based on the surface reflection neutralization techniques was shown to provide enough fast neutrals for ashing applications. The surface roughness of the post-cleaned wafer was less than 10 Å. Ex-situ and in-situ measurements yield typical removal rates of about 10 Å/s without stream collimation. The removal rates at increasing pressures show a trade-off between creating higher density plasma, leading to a large initial neutral flux and attenuation of neutrals due to collisions. Both optical emission and Langmuir probe studies indicate a mode transition as the rf power is increased. Changing the reflector plate changes the neutral energy without changing the discharge composition. A novel technique, combining momentum and heat flux measurements shows that neutral stream energy is 3~6 eV and the neutral flux is on the order of  $3 \times 10^{15} \text{ cm}^{-2} \text{ s}^{-1}$ . The derived etch rates from the measured neutral flux and energy values and the experimental rates are in good agreement. Quasi-static capacitance-voltage measurements demonstrate that the low energy neutral source induces much less damage than other plasma sources. Most of the neutral process damage is caused by uv photons escaping from the plasma source zone. The process-induced damage vary with the reflector bias and rf power.

## Low Damage Processing and Process Characterization

# Chapter 1

## Introduction

### 1.1 Why We Study Charge-free Processing

As device sizes shrink to levels well below the current  $0.25\ \mu\text{m}$  features, many problems associated with plasma processing such as the loss of critical dimensions, contamination, and charging [1] will be exacerbated. For example, in etching processes low-energy ions can hit the sidewall before they can reach the bottom of narrow features, which results in loss of profile control, leading to vias or trenches which are difficult to fill in subsequent steps (Fig. 1.1) [2]. Even the impingement of ions and electrons on surfaces at much lower energies, may have an inherent capacity to damage materials by charge trapping or coulomb excitations [3,4]. It is believed that the main source of the device damage is caused by charging and that the damaged device could only be annealed to yield acceptable performance for short periods of time. The charging damage induced by non-uniformity, resulting from non-uniformities in gas feeds, capacitive or inductive power coupling, or external dc magnetic or electric fields

can lead to variations in the ion current or the space potential across the wafer. The resultant currents flowing through the wafer will damage the delicate semiconductor junctions or insulator layers. Such damage can also occur during process start up or shut down transients or transients induced by arcing or discharge concentration on the chamber walls.

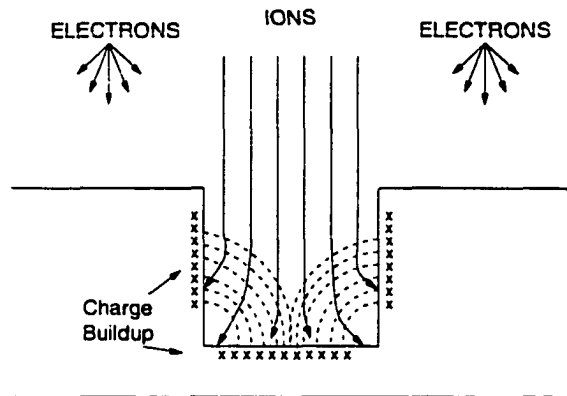


Figure 1.1: Morphological damage by non-ideal processing technology (adopted from [2])

Many previous efforts focused on improving the plasma uniformity. However, charge induced damage continues to be observed even in uniform plasmas for high aspect ratio trench etching. For example, a new type of damage (electron shading damage) [5], caused by the difference in angular distribution between ions and electrons, becomes the main concern as the feature sizes further decrease. In addition, other components in plasmas such as UV photons from the plasma source region will continue to be a source of damage [6] and this type of damage will increase as the feature size decreases. The use of new materials also poses great challenges for plasma source development. For example, in the ashing process involving low  $\kappa$  dielectric materials, the inclusion of the high energy ions causes large drifts in  $\kappa$  [7]. Though

some alternatives, such as “downstream” or “remote” plasmas [8], have been developed for cleaning or stripping processes, a charge-free processing scheme is needed to eliminate this problem and to get ready for the even more fragile devices.

By etching or stripping with neutral atoms and molecules one can avoid much of the damage that results from the charging of insulator layers. If the beam energy can be tuned to be just above the threshold for specific chemical activation of each step, it is possible to completely eliminate implantation, displacement, and other damage. The optimal energy for such a general purpose source is between 1 and 10 eV, though there may be a need for higher energy sources for certain etching steps. Besides etching and ashing or stripping via neutral beams, these low energy processes are also promising for deposition or modification of new materials because of their potential to reduce the latent damage in materials while maintaining the advantages of energetic bombardment.

## 1.2 Charge-Free Sources

Various types of neutral beam sources are now under development and have been described in detail by Manos *et al.* [9]. These include the free expansion source, plasma source neutral streams, and charge-exchange sources. The major problem with neutral beams is the difficulty of producing high fluxes in the energy range between 1 and 20 eV. Previous systems with high fluxes have been achieved at energies either below 0.5 eV or above 200 eV. Following the discussion of Manos *et al.* [9], we briefly review main advantages and disadvantages of each type of neutral sources in the following section.



## 1.2.1 Free Expansion Gas Sources

### Effusive Beams

The effusive sources are operated at relatively low pressure ( $< 1$  Torr). Temperatures of 1100 to 1750 K are required to achieve 50% dissociation of various reactive atoms. However, these effusive sources suffer from several drawbacks:

- Low pressure operation limits intensity;
- These sources are moderately divergent, displaying an approximately cosine dependence on angle from the central beam direction;
- These sources require very high pumping speed.

### Nozzle Beams

Nozzle beams increase the flux intensity by raising the gas reservoir pressure. Such beams generally have a  $\cos^n(\theta)$  angular distribution, where  $n=2$  to 6 is achievable. Intense nozzle beams having energies of approximately 1 eV can be achieved using this method. Higher energies can also be achieved by resonant or non-resonant laser heating of the working gases. However, laser and plasma heated nozzles are all susceptible to spatter melting and evaporation due to the large heat fluxes to the cone-shaped skimmer. In addition, resonant laser driven dissociation and heating schemes are specifically coupled to the particular optical levels of certain atoms and thus do not provide adequate species tunability. The use of laser heating also shares two other generic problems common to all high-intensity nozzle beams:

- These sources are point sources which are not useful in large area processing;
- The neutral energy is not easily tuned.

## 1.2.2 Plasma Source Neutralized Streams

This type of source consists of an ion beam extracted from a plasma, capable of providing high fluxes at low energy by the addition of electrons from an emitter at the exit. Although the stream is “neutral”, it is only by virtue of containing equal number of positive and negative charges. It is not a real “charge-free” source.

## 1.2.3 Charge-exchange Sources

Neutral beam sources using charge exchange are mainly plasma driven ion beam sources followed by a gas neutralizer cell. Typical sources are based on grid neutralization. But the intensity of such ion beam sources is severely limited at low energy by the Child-Langmuir law. This low intensity ion beam must then be charge-exchange neutralized. Even if an intense low energy (10 eV) ion beam can be produced, the charge-exchange efficiency is very low at low energies so the resulting neutral beam will be weak. Besides the lack of intensity, current grid sources also have other severe problems such as melting and contamination. Free expansion plasma sources, on the other hand, are based on the creation of a dense plasma which expands freely, either along magnetic field lines or into a field-free region. Successful sources based on the above mechanism have been reported by Cuthbertson *et al.*, Goecker *et al.*, and Nichols *et al.* [10–13]. Small area neutral sources can deliver a plasma beam with an ion current density of approximately  $4A/cm^2$  at energies below 10 eV. Broad-area high-density sources such as RFI (radio frequency induction) configured for free expansion also provide superior performance [13], [12]. Because an ICP (inductively coupled plasma) source can provide independent control of ion energy and plasma

density, with a special reflector design, this type of neutral source can provide low neutral energy and high neutral flux. Previous Monte Carlo simulations [14] concluded that such a source should be able to deliver enough fast neutrals for photoresist cleaning application. These applications will be discussed in detail in this dissertation.

### 1.3 Review of Operation Mechanism for the Low-Energy Neutral Sources

In this chapter, a brief review of the operation mechanism for our source and its related plasma physics is presented. Fig. 1.2 shows a schematic drawing of the operation mechanism of the neutral stream source developed at the College of William and Mary [13]. The surface reflection-based neutral source is made up of an RFI

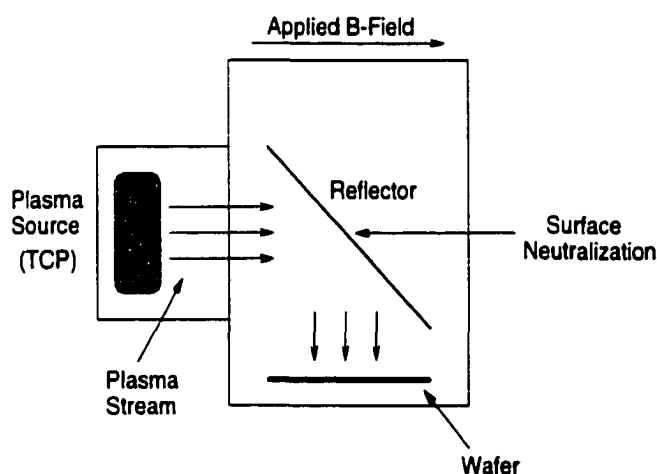


Figure 1.2: The schematic drawing of the neutral stream generation

source and an angled tungsten reflector plate. The tungsten reflector plate can be

biased at 0 to -50 V to extract ions from plasma source region. Other reflector materials have also been tested in the experiments. A small magnetic field ( $< 50$  Gauss) is used to confine the plasma, which helps to guide the ions towards the reflector plate. This magnetic field can also reduce the sputtering of the rf coupling window. The resultant fast neutrals reflecting from the plate transit to the wafers. Because of the ease of the size scale-up for ICP sources, this design can provide a much broader neutral stream than other neutral sources. The fundamentals of the neutral reflection mechanism has been described previously in Cuthbertson 's thesis [11]. We will revisit these mechanisms later in this chapter.

### 1.3.1 Plasma

A plasma is a partially- or fully-ionized gas with equal amounts of positive and negative charges. This “quasi-neutral” state is generally called “the fourth state of matter”. For plasmas of interest in materials processing, the possible applicable range is shown in Fig. 1.3 [15]. For the low pressure and high density plasma sources we are interested in, electrons are generally not in thermal equilibrium with ions and neutrals or with the chamber walls because of their small mass. Electrons are more mobile than ions and can be preferentially heated by the applied electric field. The electrons exchange energy with ions and background gases through inelastic and elastic collisions. The fraction of ionization is only about 1 to 5% even in these “high-density” plasma sources. As a consequence of this very low charged to neutral particle ratio, collisions of particles with neutrals are very important. This creates a discharge of plasma density on the order of  $10^{10} - 10^{12} cm^{-3}$ , and an electron temperature of

1-10 eV, while the ion temperature is only about 0.025-0.25 eV. The electron energy

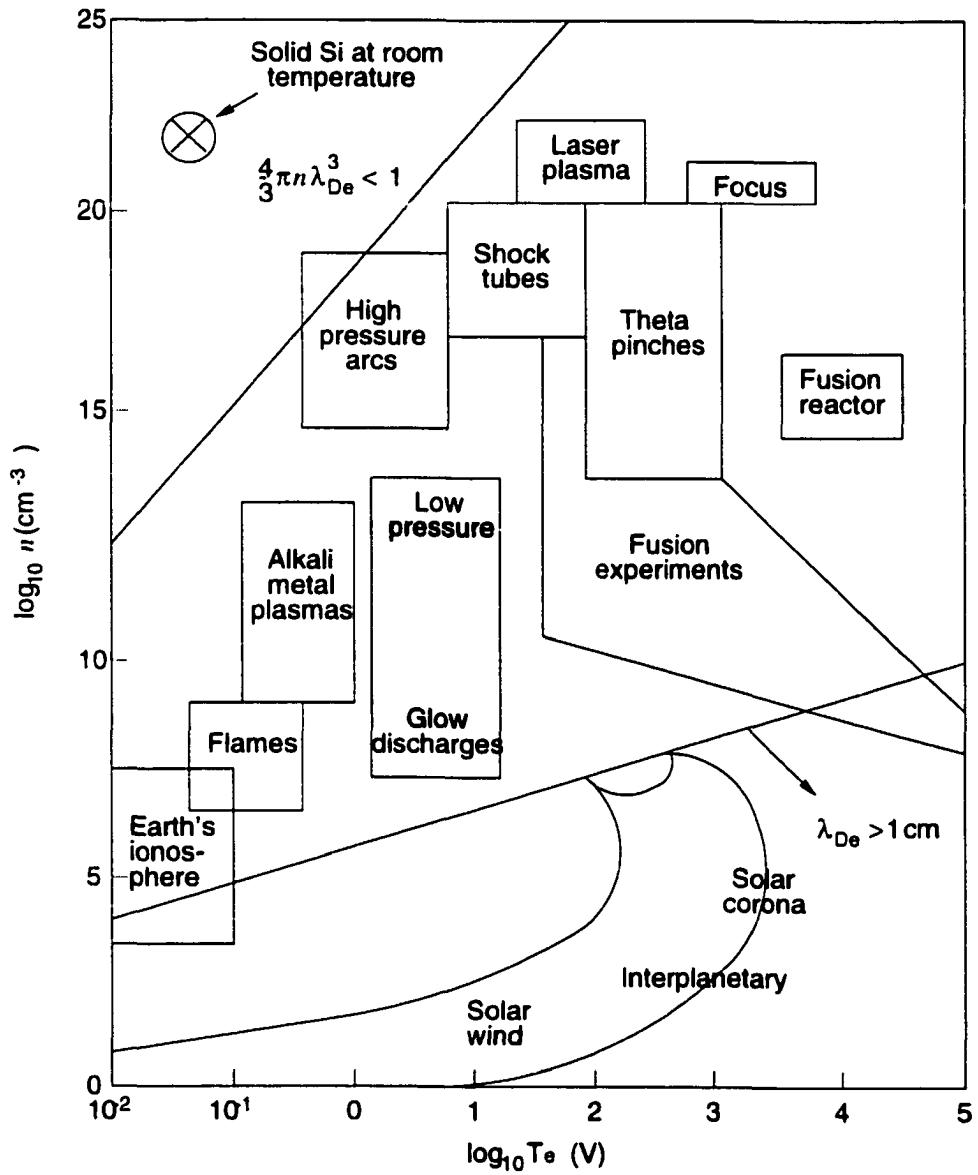


Figure 1.3: Plasma density  $\log n_e$  Vs Electron temperature  $\log T_e$ .  $\lambda_{de}$ , Debye length (adopted from [15])

can have quite different energy distributions determined by the excitation mechanism and the discharge geometry. The common form is a Maxwellian (or nearly Maxwellian) energy distribution function. Fig. 1.4 shows Maxwellian energy distribution functions with three different energies. It is well known that the high energy part of this distribution in Fig. 1.4 contributes the dominant part of the ionization, dissociation, and excitation in the discharge. However, for discharges with large numbers of metastable states, low energy electrons may also make significant contributions to ionization or excitation.

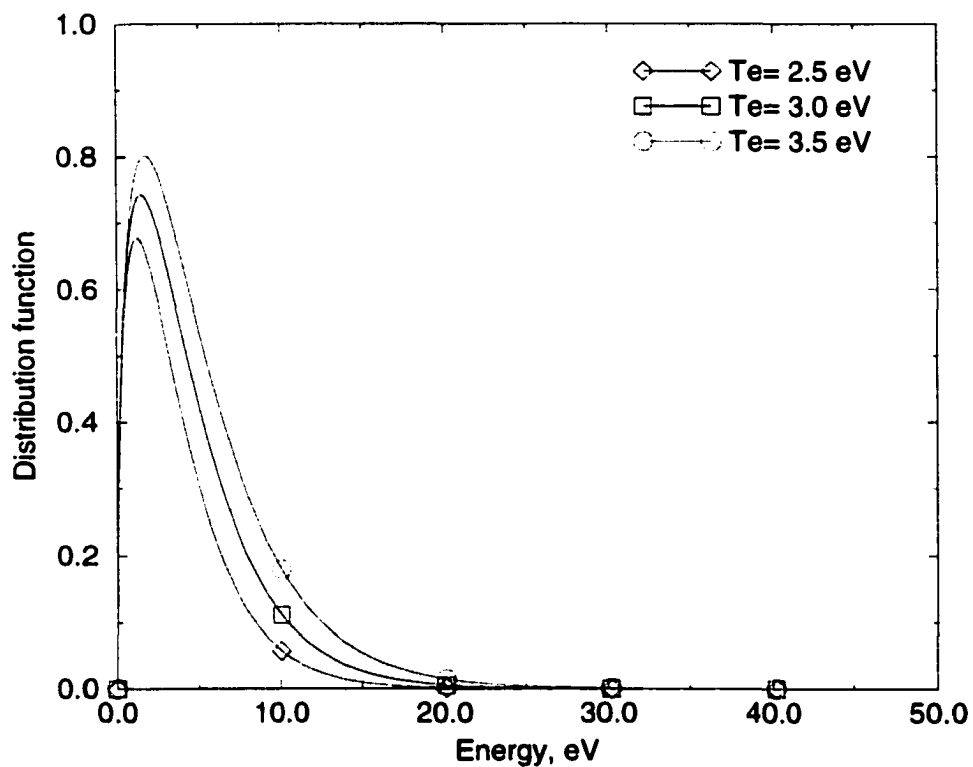


Figure 1.4: Maxwellian energy distribution function

### 1.3.2 High Density Plasma Sources

The generation of a large neutral flux relies mostly on the source's ability to generate high density ions. In conventional rf systems such as a capacitively driven rf diode, ion energy, density, and flux are linked. The combination of low ion flux and high ion energy leads to a relatively narrow processing window for many applications. This limitation pushes the development of a new generation of low pressure, high density sources. Four types of these generic sources [16] are shown schematically in the Fig. 1.5. One common feature of these sources is that the rf or microwave power is coupled to the plasma across a dielectric window, rather than by direct connection to an electrode in a rf diode. This non-capacitive power transfer is the key to achieving low voltage across plasma sheaths at the electrode and wall surfaces. With a separate rf bias on the wafer holder, independent control of the ion flux and ion bombarding energy is possible. Because of the ease of the scale-up, these high density sources are used as the ion sources in the neutral stream setup. An inductive circuit element (a spiral-like copper coil), adjacent to a discharge region in our set up, couples energy from an rf power source to an ionized gas. An additional resonant circuit is used to tune the inductor so that an electrical resonance at the rf driving frequency is obtained. The plasma acts as a single turn, lossy conductor operating as the secondary of a transformer. Rf power is therefore said to be applied to the plasma by "transformer coupling". The radio-frequency (13.56 MHz) current applied to the coil in the ICP plasma source produces an oscillating magnetic field which induces an electric field described by:

$$\nabla \times E = -\frac{1}{c} \frac{\partial B}{\partial t} \quad (1.1)$$

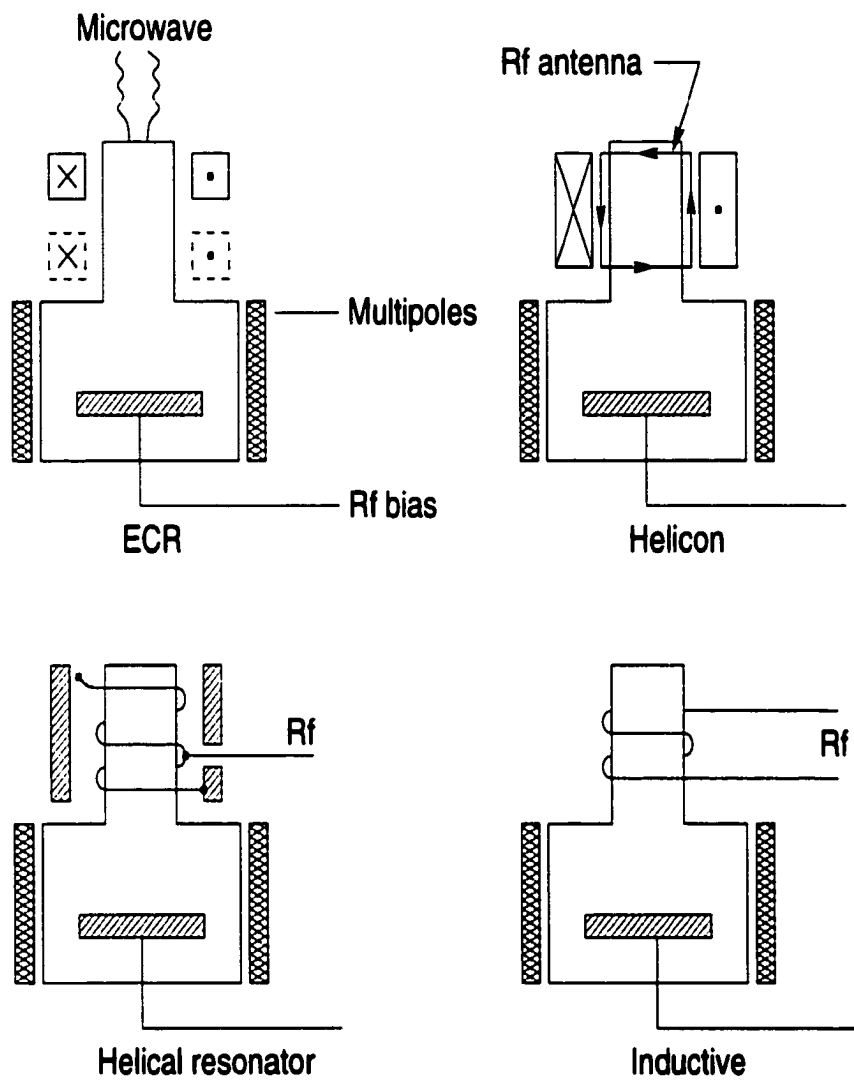


Figure 1.5: Schematic drawings of different high density plasma sources (adopted from [16])



where  $E$  and  $B$  are the electric field and magnetic induction, respectively. The induced magnetic field in cylindrical systems is :

$$B(r, \theta, z, t) = B(r)e^{\frac{z}{\delta}}e^{-i\omega t} \quad (1.2)$$

where  $\delta$  is the plasma skin depth,  $\delta = \frac{c}{\omega_{pe}}$ , where  $\omega_{pe}$  is the electron plasma frequency and  $c$  is the speed of light. The azimuthal electric field can be extracted from the measurements of the magnetic field:

$$E \simeq \phi \frac{B_r(r) \exp(-z/\delta)}{i\omega \epsilon \mu_0 \delta}. \quad (1.3)$$

Loop, or capacitive electrostatic probes, and other electric measurements have shown that the discharges can be made sufficiently uniform (2.5 % and 3.5%) by the addition of multi-cusp magnetic fields over 8 in. wafers. The plasma density can be increased by magnetic confinement on the order of tens of Gauss. Magnetic confinement for the spiral-coupler source also serves to lower the plasma potential. A lower plasma potential results in a lower bombardment energy of the chamber walls and coupling window. This attenuates contamination of the substrate via chamber sputtering. Experimental measurements for the ICP plasma source are presented in Chapter 2.

### 1.3.3 Sheath Theory

Formation of a plasma sheath when the plasma interacts with an immersed object contributes to the extensive use of the plasma sources. At the edge of bounded plasmas, a potential exists to contain the more mobile charged species which is needed to maintain the discharge. Fig. 1.6 shows the schematic drawing of plasma-wall interaction [15]. For a typical positive-ion plasma, the electrons are more mobile

than the ions. The plasma will therefore charge positively with respect to a grounded wall. This region between the plasma and wall is called the sheath, with a separation of time scales such that electrons respond rapidly to the time variation of electric fields while ions respond slowly. Without such a sheath region in a quasi-neutral

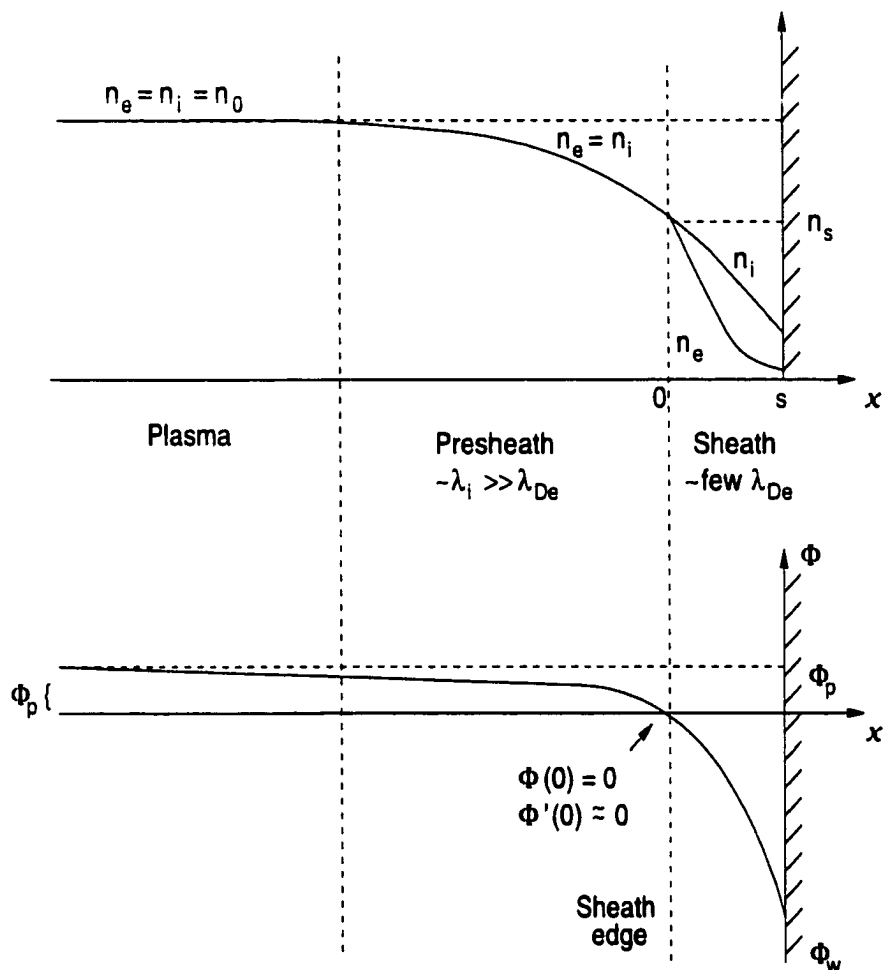


Figure 1.6: Schematic drawing of plasma sheath in contact with a wall,  $\lambda_i$ , ion mean free path and  $\Phi_p$ , plasma potential.

plasma, the electric field and potential should be zero everywhere by Poisson's equa-

tion. To analyze the sheath we assume a Maxwellian electron energy distribution, cold ions,  $n_e(0) = n_i(0)$  at plasma sheath interface, and that the boundary flows obey following ion energy conservation and continuity equations:

$$\frac{1}{2}Mu^2(x) = \frac{1}{2}Mu_s^2 - e\Phi, \quad (1.4)$$

$$n_i(x)u(x) = n_{is}u_s, \quad (1.5)$$

where  $n_{is}$  is the ion density at the sheath edge, and  $M$ ,  $m$  are the ion mass and electron mass, respectively. Solving Poisson's equation, subject to these constraints, the sheath potential at a floating unbiased wall is found to be:

$$\Phi_w = -T_e \ln\left(\frac{M}{2\pi m}\right)^{\frac{1}{2}}. \quad (1.6)$$

For argon discharges, with an initial ion energy of  $T_e/2$  at the sheath-presheath edge, argon ions would bombard an unbiased object with an energy of  $5.2 T_e$ . Electrodes with potentials on them, either dc or rf, can be bombarded with much higher energies. These electrodes will also draw a substantial net current. For electro-negative discharges, the ratio  $\Phi_p/T_e$  is found to be very nearly 1/2 if  $\gamma = T_e/T_i > 30$ . Sheath voltages are often driven to very large multiples of  $T_e$ . If only ions are present in the sheath, a "matrix sheath" is achieved where the sheath thickness is given by

$$s = \lambda_{de} \left(\frac{2V_o}{T_e}\right)^{\frac{1}{2}}. \quad (1.7)$$

where  $\lambda_{de}$  is the Debye length. In the steady state, a self-consistent solution gives the well known Child law for space-charge-limited current:

$$j_o = \frac{4}{9}\epsilon_o \left(\frac{2e}{M}\right)^{\frac{1}{2}} \frac{V_o^{3/2}}{s^2}. \quad (1.8)$$

Under conditions where a large number of collisions occur for mobile ions in the sheath, the collisional form of the Child law in which the ion mean free path,  $\lambda_i$ , is independent of ion velocity is:

$$J_o = \frac{2}{3} \left(\frac{5}{3}\right)^{3/2} \epsilon_o \left(\frac{2e\lambda_i}{\pi m}\right)^{1/2} \frac{V_o^{3/2}}{s^{5/2}}. \quad (1.9)$$

These equations can be used to develop plasma diagnostics and other applications.

### 1.3.4 Neutralization Mechanism

The surface neutralization and reflection scheme is used to achieve a high-intensity neutral flux when the plasma freely streams along magnetic field lines from the source to a conducting target plate downstream. The plate can be biased relative to the plasma at a voltage from 0 to -50 volts. Cold ions in the plasma ( $T_i < 1$  eV) are accelerated through the sheath established between the plasma and the plate. These ions strike the plate with the potential difference of the sheath (a few eV to tens of eV depending on the bias voltage and the plasma potential) and are neutralized by resonant or Auger processes to reflect predominantly as neutral particles. These processes have been thoroughly characterized for a large number of choices of ion and plate species [11]. Radiative processes are not considered in this source [11]. Two types of neutralization dominate in the reflection source while the radiative process is at a much large time scale and will not be considered in this source. The resonant and Auger processes [14] occur within several Å of the surface, where the wave functions of the electrons in the metal begin to become appreciable. Resonance neutralization is a one electron process in which an electron in the conduction band tunnels into an excited level of the incoming atom, illustrated by transition 1 in the electron energy

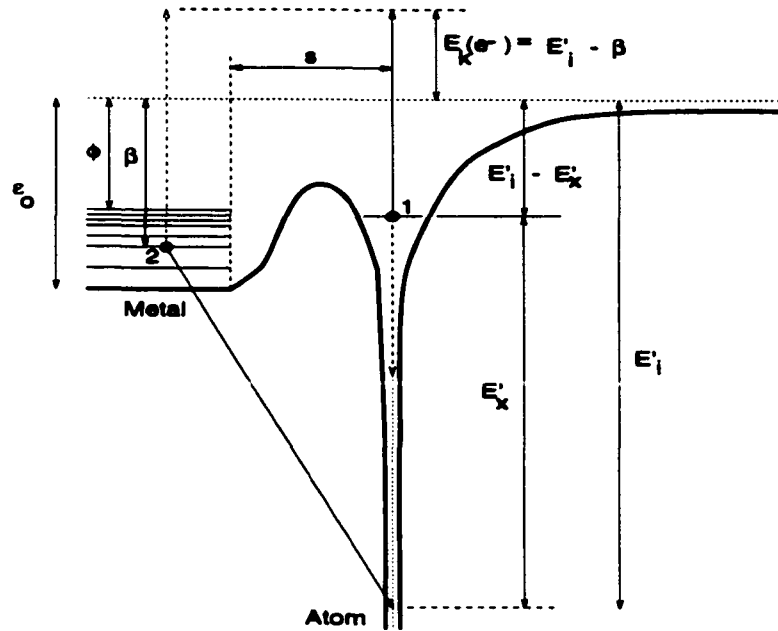


Figure 1.7: Auger surface neutralization scheme

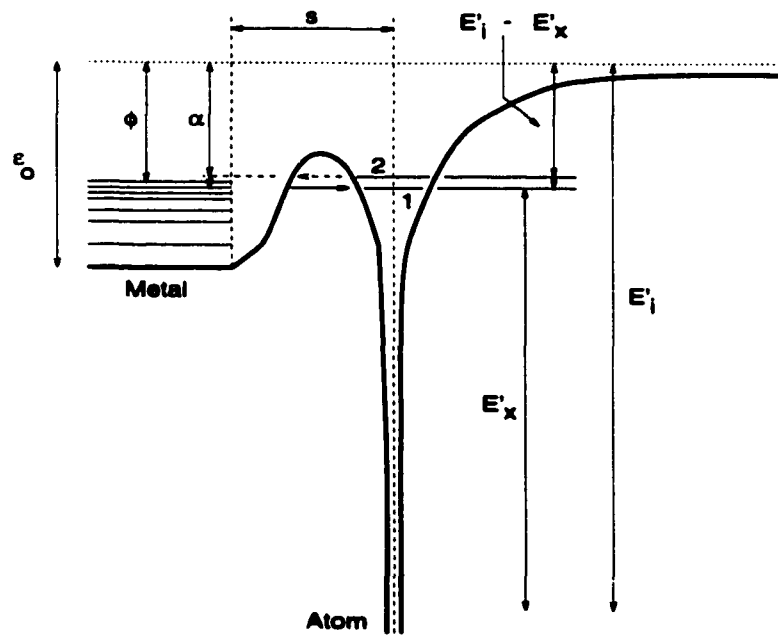


Figure 1.8: Resonance surface neutralization scheme

diagram of Fig 1.8. The vacuum energy level at the top represents the potential at the metal surface. Since by the Franck-Condon principle no kinetic energy is transferred to the atom during an electronic transition, the electron must come from a filled level in the solid at the same energy as the excited state. Such a transition can thus occur only if the effective ionization energy of the excited state is greater than the work function of the metal.

Auger neutralization is a two electron process. As the ion approaches, an electron tunnels from the metal into the atomic ground state of the ion, while the potential energy thus released excites a second metal electron from another level in the conduction band. This second electron may be ejected from the solid if it happens to be directed toward the surface. These processes can be characterized by transition probabilities (per unit time) depending on the distance of the particle from the surface. These probabilities are very large for low energy ions so low energy ions of high ionization potential approaching the surface almost always end up as ground state neutral atoms upon striking the surface. After a close collision with surface atoms, the incident atom might also be reflected back from the surface in a neutral excited state. But an excited atom is subject to similar Auger de-excitation processes as it moves away from the surface. Thus the fractions of low-energy noble gas ions reflected from metals as ions or metastable atoms are very low, typically well under  $10^{-3}$ . Following surface collision process with the reflector plate, the incident particle loses energy by inelastic loss to the electrons and by imparting the recoil energy to the surface atoms. The latter is responsible for the reflection of the incident atom. A hyper-thermal projectile encountering a surface composed of much heavier atoms is

very likely to experience large-scale collisional deflection from the surface.

## 1.4 Previous work - Monte Carlo Simulation

Earlier work [14] in our group was performed to simulate the neutral generation and transportation in our source. That Monte Carlo simulation model assumed time-independent plasma density spatial profiles in the source region:

$$n(r, z) = n_o \left(1 - \left(\frac{z}{L(x, y)}\right)^2\right)^{n_l} \left(1 - \left(\frac{r - r'}{r_o}\right)^2\right)^{n_r} \quad (1.10)$$

where  $n_o$  is the maximum plasma density at  $z = 0$ .  $n_r$  and  $n_l$  are radial and axial shape parameters, respectively,  $r'$  is the radius of the power deposition toroid, and  $R$  and  $L(x, y)$  are the radius and length of the plasma column, respectively. The parameters  $n_l$  and  $n_r$  are determined from the power and particle balance, respectively. Neutral particles are launched from the reflector plate using a sampling procedure. The angular distribution of launched particles is assumed to be of the form  $f(\theta) = N_\theta \cos^{n_\theta}(\theta)$  where  $N_\theta$  is the normalization constant,  $n_\theta$  is the degree of the angular distribution, and  $\theta$  is the launch angle with respect to the reflector normal. The reflector neutral energies are sampled from an energy distribution of the form:

$$f(E) = N_E \left[1 - \left(\frac{E - E_c}{E_w}\right)^2\right]^{n_e}. \quad (1.11)$$

where  $E$  is the neutral energy in eV,  $N_e$  is a normalization constant,  $E_c$  is the mean launch energy,  $E_w$  is the width of the energy distribution at the base, and  $n_e$  is the degree of the energy distribution.  $E_c$  is determined from the applied reflector bias and the neutral energy reflection coefficient  $r_b$ , which varies depending on the particular

reflector materials/feedstock gas combination. A probability array is constructed from the relative collision frequencies for each process under consideration (elastic, charge-exchange, ionization ) as a function of energy:

$$P_{i,j} = \sum_i^N \frac{\nu_{i,j}}{\nu_{max}} + \frac{\nu_{max} - \nu_{imax}}{\nu_{max}}, \quad (1.12)$$

where  $i$  = energy index,  $j$  = process index,  $N$  = number of processes,  $\nu_{i,j}$  is the collision frequency for the  $j$ th process at energy  $i$ ,  $\nu_{imax}$  is the maximum collision frequency at energy  $i$ ,  $\nu_{imax} = \sum_{j=1}^N \nu_{i,j}$  and  $\nu_{max}$  is the maximum collision frequency over the entire energy range. The simulation begins by selecting a site on the reflector plate and determining the number of particles to launch from that position. The particles are launched according to the assumed angular and energy distributions. The pressure, plasma density, and ion/neutral reflection parameters are the primary parameters varied to assess the performance of this design. The simulation studies indicated a trade-off caused by pressure increase between the initial high intensity beam and the attenuation of neutral transit in the down stream. Simulations also indicated a narrow tunable energy range for the reflected neutrals.

## 1.5 Purpose of this Work

The purpose of this work was to evaluate the process performance of our neutral stream source to our pulsed plasma source and to compare their process damage. There were a number of deliverable goals and tasks required to achieve a more through understanding of pulsed operation of this source. Among them were:

- Characterize ICP plasma source to achieve a better understanding of contin-



uous wave (cw) plasma discharge chemistry and physics (Chapter 2).

- Develop electrostatic probe diagnostics to characterize low damage process-pulsed discharge (Chapter 3).
- Simulate pulsed discharges of Ar and oxygen mixtures to enhance the understanding of plasma chemistry and mechanism of pulsed processes (Chapter 4).
- Evaluate ashing performance of low-energy neutral stream source and compare to Monte Carlo simulation results (Chapter 5).
- Perform the neutral energy and flux measurements to explain the relationship between the experimental rates and neutral stream parameters (Chapter 6).
- Assess the neutral process-induced damage and compare with other process-induced damage (Chapter 7).

## **1.6 Organization of Dissertation**

Because the parameters in the plasma source zone interlink with the rates of etch and clean processes and because damage occurs in the source zone, the process results will be presented interleaved with source characterizations. Chapter 2 presents a brief review of plasma diagnostics and their application in the continuous wave ICP plasma source. Most of the discussion centers on the optical emission method and its application to plasma discharge studies.

In Chapter 3, we present a double probe setup capable of measuring the pulsed plasma properties. We also discuss pulsed plasmas as a function of the pulse frequency and duty cycles. In Chapter 4, we discuss a global average model for simulation of both cw and pulsed plasma discharges.

In Chapter 5, ashing studies with the neutral beam source are performed. Many experimental issues will also be discussed in this chapter. The experimental results are also compared with the simulation results. In Chapter 6, we present a novel method to measure the neutral energy and flux. This method combines a micro-torsion balance and a calorimeter to measure both the energy and the flux of the neutral stream. Using the neutral flux value and energy-dependent etch-yield values, the calculated stripping rates are compared to experimental results. In Chapter 7, we compare the process damage caused by different plasma processes and discuss the process damage as a function of the reflector bias and rf power.

# Chapter 2

## Plasma Discharge Characterization

### 2.1 Introduction

There are various methods, such as Langmuir probes, optical emission, mass spectrometry, microwave interferometry, and laser induced fluorescence methods to characterize the plasma discharge. In this study, Langmuir probes and optical emission methods were used to measure plasma parameters such as electron temperature and plasma density. Mass spectrometry was used to measure the dissociation rate of molecular gases and also to provide a survey of process gas purity and contamination species.

#### 2.1.1 Langmuir probe studies

Langmuir probes are metal probes, inserted into a discharge and biased positively or negatively to draw electron or ion current. These probes are completely surrounded by a plasma sheath. These probes are usually quite small and under

suitable conditions, produce only minor local perturbations to the plasma. Fig. 2.1 shows a typical current vs voltage plot from a single Langmuir probe. At the probe voltage  $V_p = V_s$ , the probe is at the plasma potential and draws current mainly from the more mobile electrons, designated as positive current flowing from the plasma into the probe.  $V_f$  is the potential at which an insulated probe, does not draw a net current [17]. To minimally disturb the plasma and also for the ease of construction, Langmuir probes are often made up of the thin wires with radii smaller than the

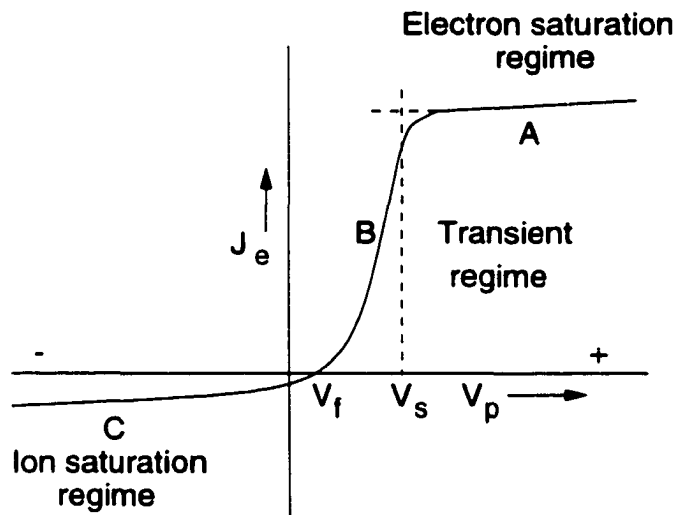


Figure 2.1: Single Langmuir probe characteristic I-V curves

Debye length  $\lambda_{de}$ . Different probe geometries, such as planar and cylindrical probes have been used extensively in the plasma discharge characterization. The probe analysis varies depending on the ratio between the Debye length and probe size. Accurate results have to take the ion temperature, ion trajectories, and probe geometries into account. Additional complications also arise because of different experimental configurations. For example, in an rf driven plasma, the probe has to float with the

plasma to eliminate the effects of the oscillating potential. In our general analysis, a Maxwellian energy distribution is assumed for all data analysis though some deviations are expected in experiments. More details of single probe setup in cw plasmas were included in Nichols's thesis [14].

### 2.1.2 Optical Emission Studies

Optical emission spectroscopy is another useful method to investigate chemically complex discharges. Compared to the Langmuir probe measurement, it is a non-invasive method and provides excited species information in the discharge. The wavelength-resolved optical emission also may be spatially resolved perpendicular to the line of sight. In our studies we used a spatial average along the line of sight. The observed emission intensity is a convolution of the species density for the optical wavelength being monitored, the electron energy distribution function, and the cross section for electron impact excitation of the optical level. Fig. 2.2 illustrates the direct electron impact excitation of the ground state of atom A to an excited state  $A^*$ , followed by subsequent emission at frequency  $\omega$  to some lower energy state  $A_f$ . The emission wavelength is determined from:

$$\lambda = \frac{2\pi c}{\omega}. \quad (2.1)$$

The emission should be sharply peaked at  $\lambda$ , usually with a small intrinsic line width associated with the spontaneous emission rate from level  $A^*$ . Eqn. 2.2 can be used to calculate the emission intensity at the wavelength  $\lambda$ . The intensity,  $I_{A_i,j,k}$ , of emission is from the  $i$ th atomic species or state at wavelength  $\lambda(j,k)$  accompanying the transition between the  $k$ th and  $j$ th levels. Population of the initial excited level

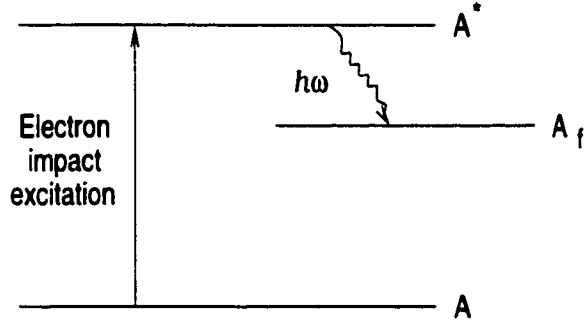


Figure 2.2: Schematic drawing of the photon emission

occurs by electron impact excitation of the atom from a lower state  $A_i$  (its ground state, or a metastable state) to the excited state  $A_k$ . The net intensity measured by a spectrometer can be calculated from [15]

$$I_{A_i,j,k} = 4\pi\alpha(\lambda_{j,k})n_{A_i}Q_kB_{j,k} \int_{v_{0,A_i,k}}^{\infty} \sigma_{A_i,k}(v)v^3 f_e(v)dv, \quad (2.2)$$

where  $\alpha(\lambda_{j,k})$  is the spectrometer sensitivity at  $\lambda_{j,k}$ .  $n_{A_i}$  is the number density of  $A_i$ ,  $\sigma_{A_i,k}(v)$  ( $= 0$  for  $v < v_{0,A_i,k}$ ) is the effective cross section for an electron with speed  $v$  to excite a transition from level  $A_i$  to  $A_k$ . This includes cascading from levels above  $A_k$  that are populated by electron impact excitation from  $A_i$ . Other parameters above include the quantum yield,  $Q_k$ , for emission of a photon whereby the excited state  $A_k$  spontaneously relaxes to any lower state given by :

$$Q_k = \frac{\tau^{-1}}{\tau^{-1} + K_q P} \quad (2.3)$$

where  $\tau$  and  $K_q$  are the radiative lifetime and effective quenching rate constant for  $A_k$  by all species at total pressure  $P$ . For emitters with very short radiative lifetimes, and at the low pressure used in this study,  $Q_k = 1$ . In Eqn.2.2,  $B_{j,k}$  is the branching

ratio for the transition  $A_k \rightarrow A_j$ , defined as:

$$B_{j,k} = \frac{i_{A_j,k}}{\sum i_{A_k}}. \quad (2.4)$$

The assumed electron energy distribution is Maxwellian:

$$f_e(v) = \left(\frac{m_e}{2\pi kT_e}\right)^{3/2} \exp\left(-\frac{m_e v^2}{2kT_e}\right), \quad (2.5)$$

where  $m_e$  is the electron mass and  $T_e$  is the Maxwellian electron temperature. The total emission at  $\lambda_{j,k}$  is determined by summing over the electron impact excitation processes from all lower states,  $A_i$ .

### Electron Temperature and Particle Density Measurements

Similar to the Langmuir probe method, the optical emission method can also be used to measure the electron density and mean electron temperature,  $n_e$  and  $T_e$  of the plasma. In the coronal equilibrium regime,  $T_e$  may be determined from optical measurements using the following expression: [18]

$$\frac{I^+}{I_o} = C_1 T_e^{0.75} \exp[-(E_g + E_i - E_n)/T_e] \quad (2.6)$$

where  $I^+$  and  $I_o$  denotes the ion and neutral emission intensity;  $E_i$  the ionization energy of the atom;  $E_g$  the energy of the excited level of the singly charged ion relative to the ion ground state; and  $E_n$  the energy of the excited neutral atom relative to the neutral ground state.  $C_1$  is a parameter depending on the energy levels involved and on the collision cross-sections.

An plasma frequently had metastable densities that exceed a fraction equal to  $10^{-5}$  of the ground state density in the gas [19]. The electron excitation cross

sections of metastable species into higher levels can be 100 or 1000 times as large as the corresponding cross sections for excitation of ground state atoms. Because electron temperatures in such systems are frequently low (less than a few eV), there are orders of magnitude more electrons with sufficient energy for excitation out of metastable levels (about 1.5eV for Ar) than there are with enough energy to excite atoms out of the ground state (about 13 eV for Ar). For example, an emitting  $2p_x$  level of the rare gases "A" can be populated through electron impact excitation either from the ground state or the metastable state:



or through radiative cascades from higher states initially excited by electron impact. The resultant intensity of the observed emission of the excited states of A, i.e. from  $A^*$  is proportional to

$$I_{A^*} \propto n_{A^*} \propto \sum_i n_i \int_0^\infty \nu \sigma_{i,A^*}(E) f(E) dE \quad (2.9)$$

where the sum represents the excitation of emitting  $A^*$  states from any i states, which may be a ground state of species A or a molecule AB that undergoes the dissociative excitation process:



A technique described by Malyshev *et al.* [19] measures the electron temperature by adding trace amounts of rare gases (He, Ne, and Ar) into the discharge and comparing



observed atomic emission intensities with those extracted from a computational model including the contribution from metastable states. If the  $A^*$  state is primarily excited from the ground state, then the equation can be rewritten and the emission intensity is proportional to the number density of ground state of A.

### 2.1.3 Actinometry

The actinometry method, as described by Coburn and Chen [20] has been used to measure the active species in the discharge [21–27]. A small amount of a rare gas (usually Ar) is added to the discharge and the emission from a species of interest (A) with an unknown number density is divided by that of the rare gas to account for variability of  $n_e$  and  $T_e$ . By choosing the Ar emitting level such that the cross section for excitation  $\sigma_{Ar,Ar^*}$  is similar to  $\sigma_{A,A^*}$  one may write:

$$\frac{I_A}{I_{Ar^*}} \propto \frac{n_{A^*}}{n_{Ar^*}} \quad (2.11)$$

$$\frac{n_A \int_0^\infty \nu \sigma_{A,A^*}(E) f(E) dE}{n_{Ar} \int_0^\infty \nu \sigma_{Ar,Ar^*}(E) f(E) dE} \approx a \frac{n_A}{n_{Ar}} \quad (2.12)$$

where  $a$  is a constant. The similarity of the two cross sections allows approximate canceling of the integrals and thereby eliminates the dependence on  $n_e$  or  $T_e$ . Hence, the relative density of species A can be obtained from the ratio of corresponding emissions, since the density of Ar is easily controlled and therefore, can be taken as known. However, reliable actinometry measurements require the following experimental conditions be fulfilled:

- The excitation of the emitting level comes only (or mostly) from the ground state. Since the excitation of 2P Paschen levels of the rare gases often occurs through

the metastable states, the emitting level must be chosen such that this contribution is negligible under all conditions of interest.

- The cross sections for studied species and actinometer gas as function of energy must be similar in magnitude and velocity dependence. Changes in  $T_e$  and EEDF (electron energy distribution function) will appear if there are any differences, and must be accounted for in the model.

- Because of possible re-absorption of emitted radiation, at partial pressures higher than 0.5-1 mTorr in Ar discharges, only emission lines terminating on  $1s_2$  or  $1s_4$  states should be monitored. The density of metastable  $1s_3$  or  $1s_5$  is high enough to give self-absorption under these conditions and thus may not be used [19]. The  $7504\text{\AA}$  ( $2p_1$ ) and  $7515\text{\AA}$  ( $2p_5$ ) lines are nearly free of contributions from metastables and hence are the best ones to use in actinometry.

## 2.2 Experimental Setup

Experiments were performed in the apparatus shown in Fig 2.3 which will be discussed later in detail. The plasma source chamber is an 8" CF six-way cross pumped by a 450 l/s Fomblin-prepared, turbomolecular pump. A 3-1/2 turn water-cooled copper coil antenna was coupled to the main chamber through a 25mm thick quartz window. An angled tungsten plate, biased at variable negative voltages, served as a reflector plate from which ions bounce as neutrals. The current collected by the plate measures the net ion flux proportional to the resulting neutral flux as experimental conditions are changed. The system was tuned with a  $\pi$ -LCR matching network. A variable power supply (0-800W) was used in continuous wave (CW) rf power exper-

iments. Typical operating conditions in the source were:  $1 \times 10^{-3} \text{ torr} < P < 10^{-2} \text{ Torr}$ ;  $Q_{Ar} = 1 \sim 10 \text{ sccm}$ ,  $Q_{O_2} = 1 \sim 10 \text{ sccm}$ ;  $V_{bias} = 0 \sim -35 \text{ volts}$ ,  $P_{RF} = 50 \sim 600 \text{ W}$ .

Plasma density and electron temperature were measured using Langmuir probes. Langmuir probes (both double and single probe) were placed in a mini flange which is 3 inches away from the ICP (inductively coupled plasma) coil. Several viewports were used for the plasma emission studies. The same ports could be used to mount a Hiden mass spectrometer for gas composition analysis.

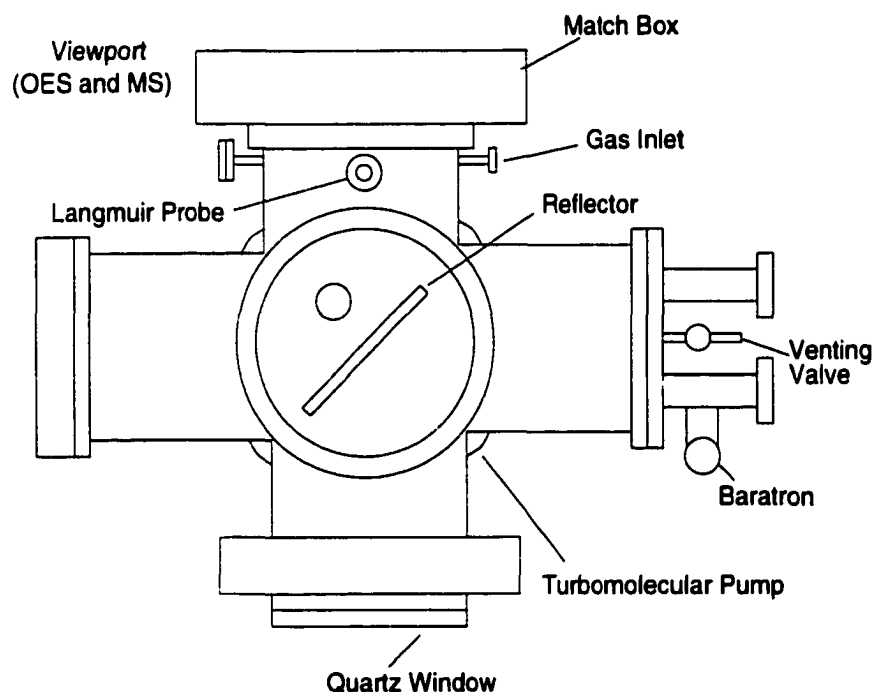


Figure 2.3: The schematic drawing of the set up for Langmuir probe and OES studies

The particle species line-integral intensities in the source chamber were measured using three different optical spectrometers. A 0.5 m monochromator (Acton SP300i) was used with three different gratings (300, 600, 1200 grooves/mm) and a 256x1024 CCD camera as a detector. This monochromator views the plasma perpen-

pendicular to a mirror axis on the mid-plane. The collected data were corrected for the wavelength response of the grating and CCD camera using a tungsten calibration lamp. In these experiments, the entrance slit of the monochromator was  $20\mu m$  yielding a resolution full width at half maximum of  $1\text{ \AA}$ . The quartz fiber coupler transmission was calibrated down to  $200\text{ nm}$ . Another single grating,  $1200\text{ grooves/mm}$ , spectrometer was used to monitor particle density at a second location. A third spectrometer, fitted with a Princeton 1460 OMA was used to monitor the plasma species density.

## 2.3 Results and Discussion

### 2.3.1 Langmuir probe studies

Fig 2.4 and Fig 2.5 show the plasma density and electron temperature, respectively as a function of the discharge pressure in Ar discharges. The electron temperature increases as the discharge pressure decreases. On the other hand, the plasma density increases as the pressure increases. As the pressure increases, the electron temperature decreases because of the increased number of collisions inside the plasma. The increase of the plasma density with the pressure is attributed to the increase of the neutral species at higher discharge pressure. The plasma density and



electron temperature as a function of the rf power are shown in Fig. 2.6 and Fig. 2.7, respectively. The plasma density increases nearly linearly with rf power while the

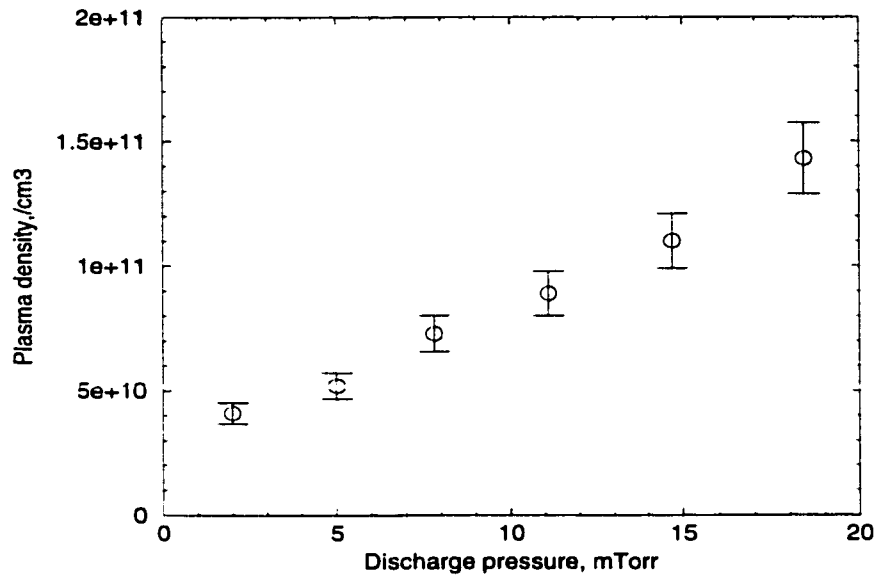


Figure 2.4: Plasma density as a function of the discharge pressure from single probe, Ar discharge, 500W

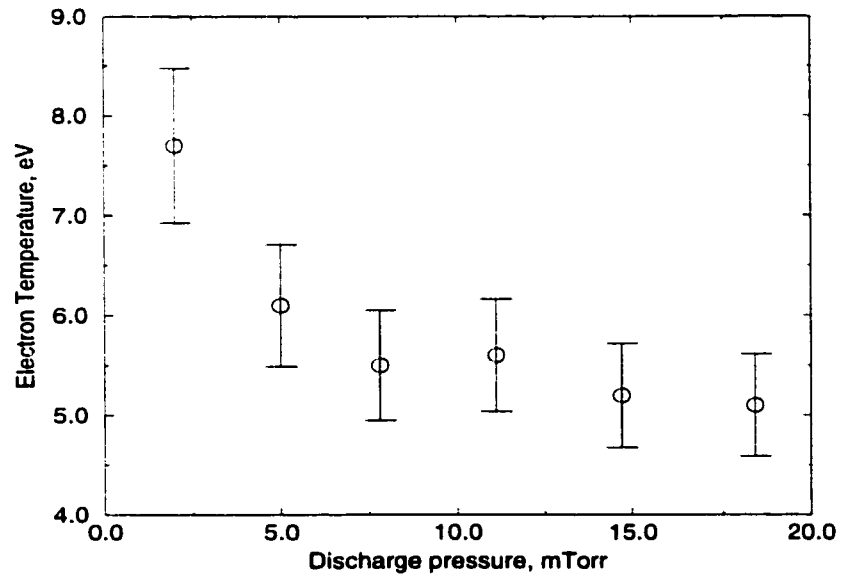


Figure 2.5: Electron temperature as a function of the discharge pressure from single probe, Ar discharge, 500W

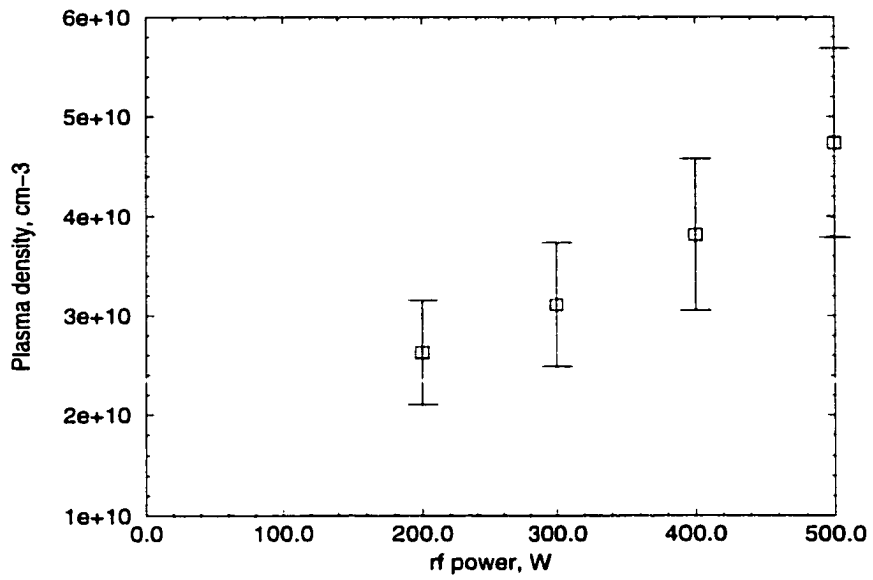


Figure 2.6: Plasma density as a function of the discharge power in Ar discharges

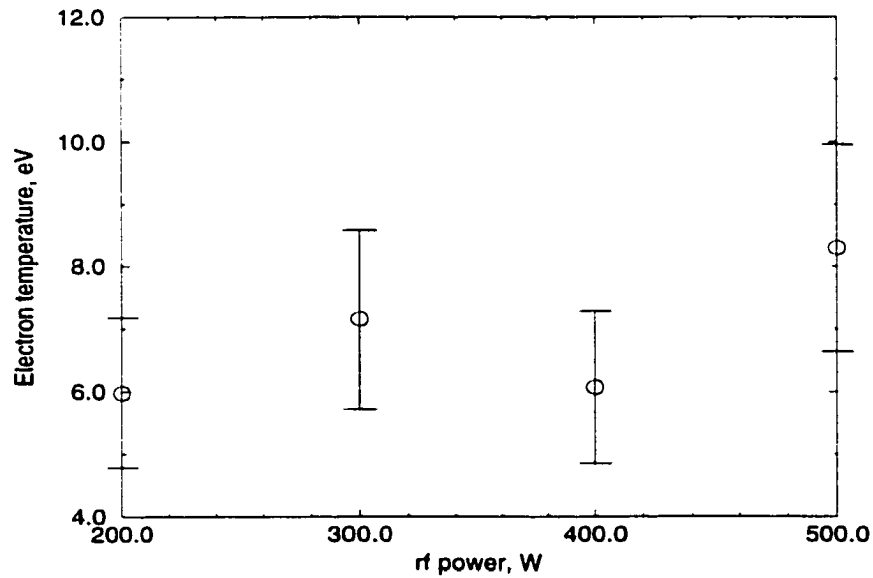


Figure 2.7: Electron temperature as a function of the rf power in Ar discharges

temperature stays the same when the rf power is over 200 W. This phenomena may be explained by a simple uniform discharge model. By equating the total surface particle loss to the total volume ionization, we can write: [15]

$$n_o u_b (2\pi R^2 h_L + 2\pi R L h_R) = K_{iz} n_g n_o \pi R^2 L. \quad (2.14)$$

$$\frac{K_{iz}(Te)}{u_b(Te)} = \frac{1}{n_g d_{eff}}, \quad d_{eff} = \frac{1}{2} \frac{RL}{Rh_L + Lh_R}. \quad (2.15)$$

Thus  $T_e$  is independent of the plasma density and input power. However,

$$n_o = \frac{P_{abs}}{e u_b A_{eff} \varepsilon_L}, \quad A_{eff} = 2\pi R(Rh_L + Lh_R). \quad (2.16)$$

where  $u_b$  is the Bohm velocity for ions.  $R$  and  $L$  are the diameter and length of the discharge chamber, respectively.  $h_L$  and  $h_R$  are parameters defined in Chapter 4.  $\varepsilon_L$  is the average collisional energy loss per electron-ion pairs and is a function of  $T_e$ . Because  $T_e$  does not change with rf power,  $\varepsilon_L$  does not change with rf power. Thus the plasma density is approximately linear with the rf power while the electron temperature stays the same. Similar results were achieved from both the double probe measurement and optical emission results. More discussion about modeling dependence of  $n_e$  and  $T_e$  will be given in chapter 4.

## 2.3.2 Optical Emission Studies

### Ar Discharges

The Ar discharge is one of the simplest and so has been investigated extensively to understand the plasma discharge mechanism. One interesting application of the Ar discharge is its use in actinometry. Fig. 2.8 shows a representative spectrum of a

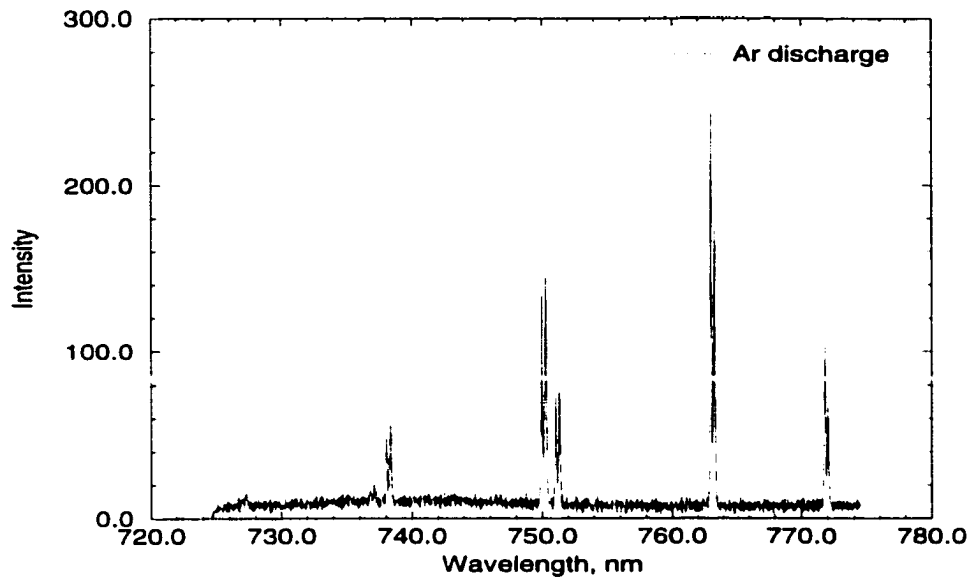


Figure 2.8: Typical Ar discharge spectrum

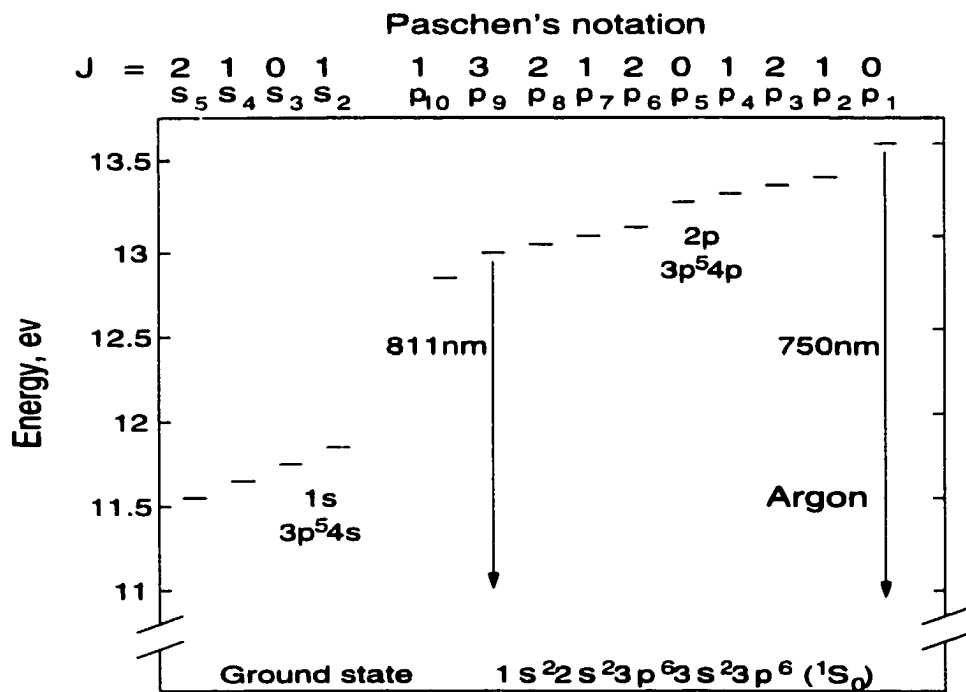


Figure 2.9: Energy diagram of Ar atoms



500 W Ar discharge spectrum at 6.4mTorr. Fig 2.9 shows the corresponding energy diagram of Ar atoms. One of most important features is the existence of large number of metastable species in Ar discharges which complicate the analysis. The first excited electronic configuration in Ar is  $3p^54s$  giving four levels. The  $J=0(1s_3$  in Paschen's notation) and the  $J=2(1s_5$  in Paschen's notation) levels are both metastable, with lifetimes over 1.3 sec. The next set of ten excited levels arise from the  $3p^54p$  configuration ( $2p_1$  through  $2p_{10}$  in Paschen's notation). Processes such as electron-atom ionization, excitation, and elastic scattering and charge transfer processes are included in the discharge analysis. Ionization from metastables is of great concern. As mention earlier, Ar 750nm and 751 nm emission lines are used frequently in following studies because of negligible contributions from metastables to the final optical emission.

## **$O_2$ Discharges**

Compared to the Ar spectrum, the  $O_2$  spectrum is much more complicated because of large number of vibration and rotation states in the molecular structure. Fig 2.10 shows a pure oxygen spectrum at 500 W at 7 mTorr. Besides the direct channels,  $O_2$  plasma radiation can also be emitted by transitions between the electronic levels, between vibrational levels of the same electronic states, or between rotational levels of electronic states. Corresponding to these channels, much more complicated processes take place in oxygen discharge. These include molecular dissociation, dissociative ionization, dissociative recombination, electron attachment, and volume recombination between the positive and negative ions. Previous studies indicate that the 844nm line can be used in oxygen discharge to represent true atomic oxygen

concentration because of a smaller contribution from dissociative excitation.

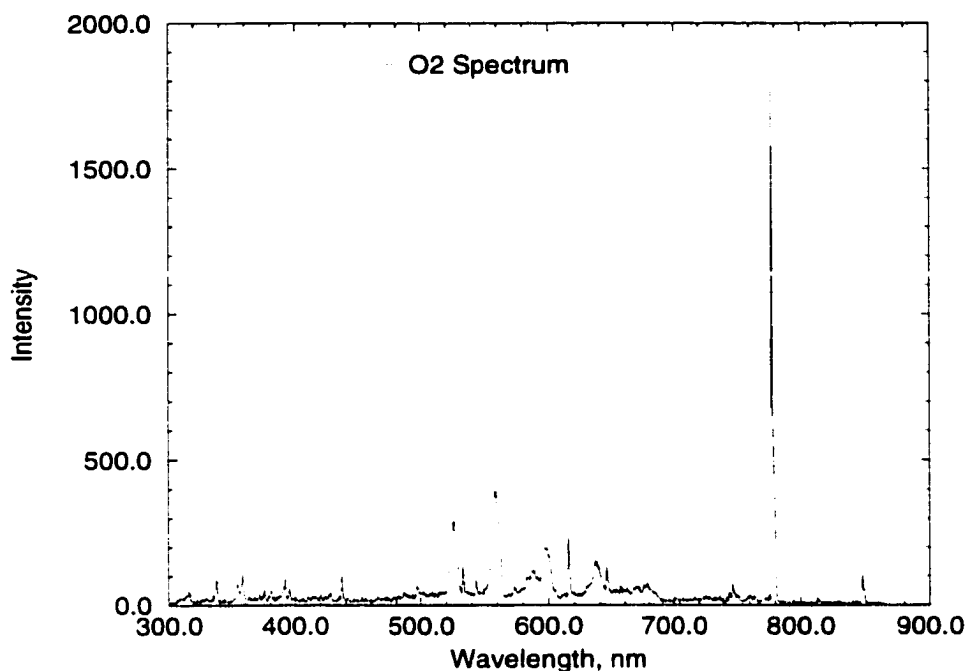


Figure 2.10:  $O_2$  discharge spectrum at 3.56mTorr, 400 W

### Ar + $O_2$ mixture

Fig 2.11 shows the OES (optical emission spectroscopy) results of the plasma source region taken as a function of the rf power for  $Ar + O_2$  plasmas. The intensities of oxygen and argon emission both increase with the rf power. The intensity ratio  $O_{777nm}(3p^5p)/Ar_{750nm}(3p^54p)$  increases sharply as the rf power increases from 100 W to 200 W. Assuming that the only atomic processes of importance for an upper level,  $k$ , are electronic impact excitation of ground state atoms and that this upper level  $k$  can only decay radiatively, then the observed relative line intensity for a transition

from level  $k$  to a particular lower level  $j$  is given by [25]:

$$I_{k \rightarrow j} = n_e n_g \langle \sigma v \rangle_{g \rightarrow k} B_{k \rightarrow j} \Omega / 4\pi, \quad (2.17)$$

where  $B_{k \rightarrow j}$  is the branching ratio [28] and  $\Omega$  is the acceptance solid angle for the detection system. Thus the ratio of two neutral Ar lines (419nm and 451nm) used in our experiments is calculated as

$$\frac{I_{k \rightarrow j}}{I_{m \rightarrow n}} = \frac{\langle \sigma v \rangle_{g \rightarrow k} B_{k \rightarrow j}}{\langle \sigma v \rangle_{g \rightarrow m} B_{m \rightarrow n}}, \quad (2.18)$$

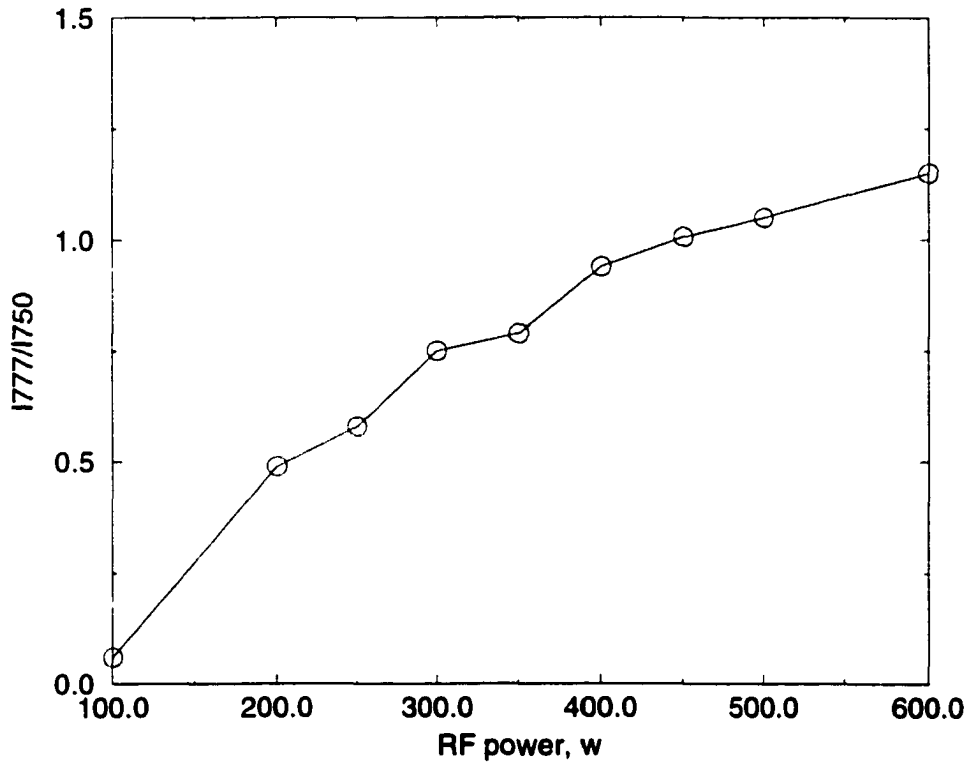


Figure 2.11: The ratio of  $O_{777}/Ar_{750}$  intensity as a function of rf power

where if a Maxwellian electron energy distribution  $f_e(v)$  is assumed, the average

electron impact excitation rate can be written:

$$\langle \sigma v \rangle_{g \rightarrow k} = \frac{1}{n} \int f_e(\nu) \sigma_{g \rightarrow k}(\nu) \nu d^3 \nu. \quad (2.19)$$

Using the neutral Ar excitation cross section data provided by Feltsan [29], Zape-sochnyi [30] and Ballou [31] *et al.* and the assumption of a Maxwellian electron energy distribution, the electron temperature in Ar plasmas is derived (Fig. 2.12).

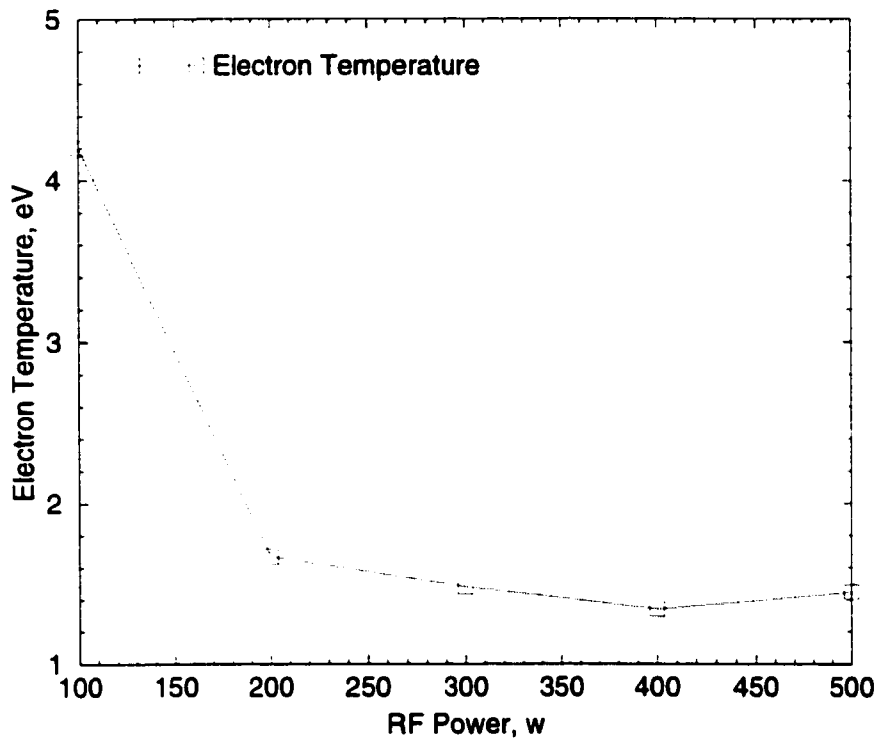


Figure 2.12: Electron Temperature as a function of the rf power from OES studies

The electron temperatures measured by the independent methods of probes (Chapter 3) and emission spectroscopy show the same behavior, indicating a mode jump from capacitively to inductively coupled mode as the rf power increases from 100 to 200W. A sudden increase of the plasma emission intensity is also visible through the

quartz window. Considering errors in the OES analysis caused by inaccuracies in the cross section data and the known errors of the probe analysis, the values of electron temperature are in relatively good agreement. Fig. 2.13 shows actinometry results for

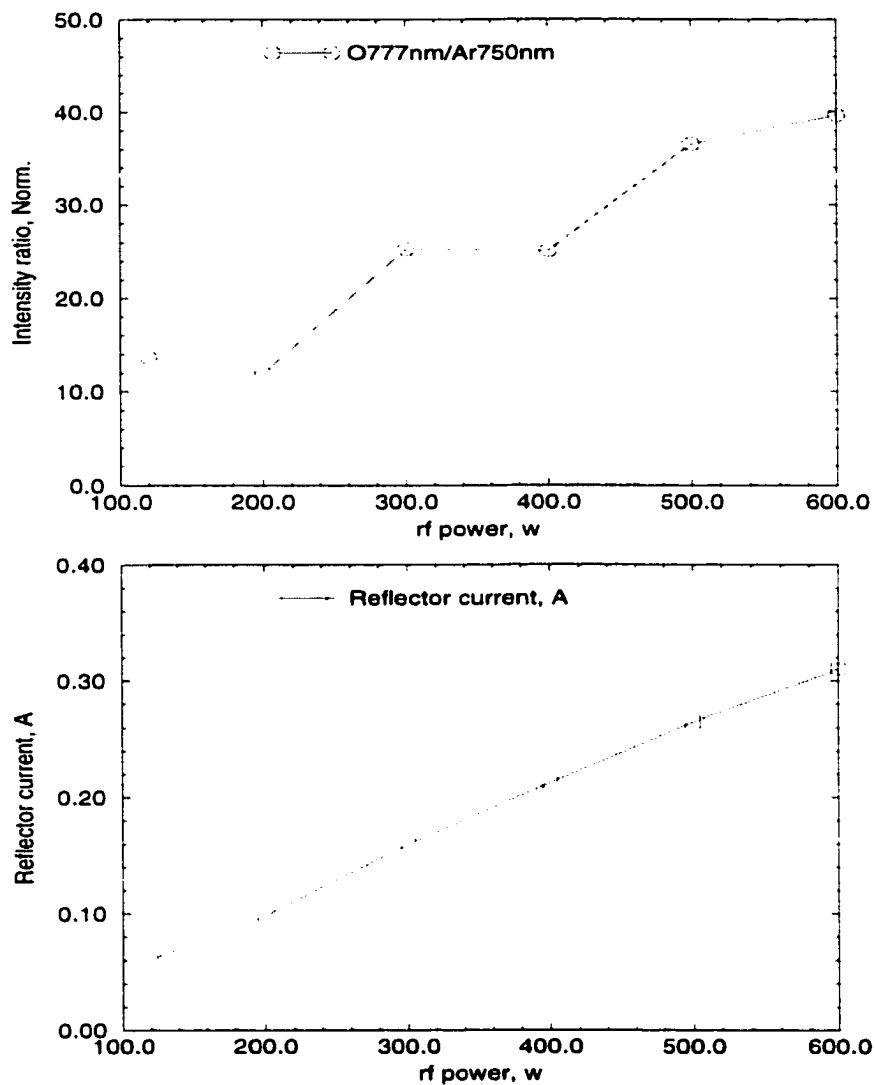


Figure 2.13: The ratio of  $O_{777}/Ar_{750}$  intensity as a function of rf power from actinometry result

$Ar + O_2$  plasmas as a function of the rf power. The ratio of  $I_{777nm}/I_{750nm}$  increases

with the rf power. This represents an increase of atomic O density as the rf power increases. The corresponding current to the reflector plate also increases because the plasma electron density increases with the rf power. Actinometry results varying discharge pressures between 2 m Torr and 20 m Torr show that the  $O_{777nm}$  emission intensity has a single minimum at 5 m Torr.

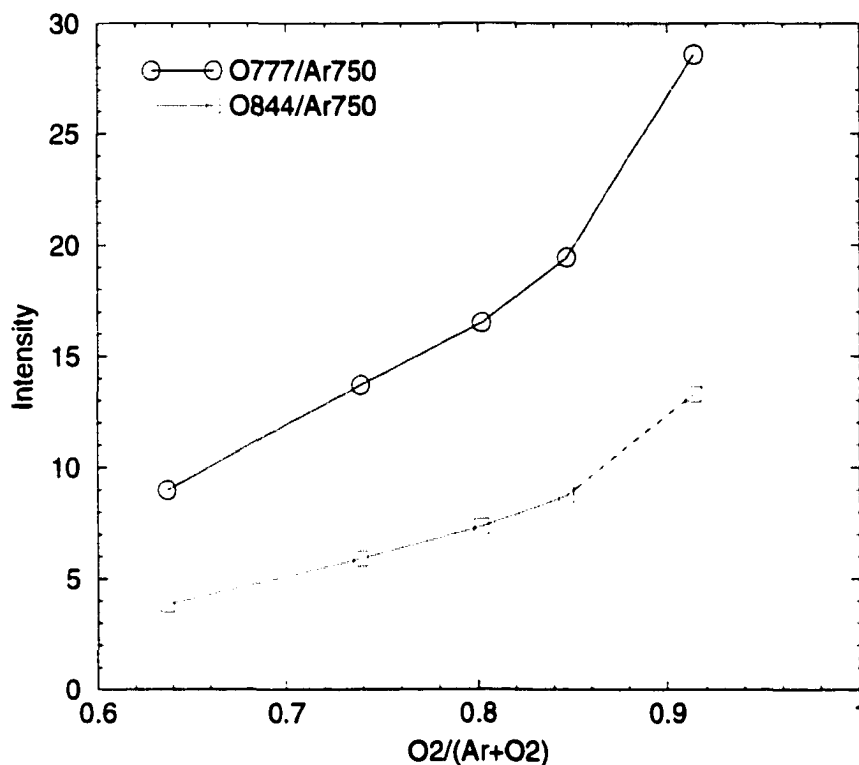
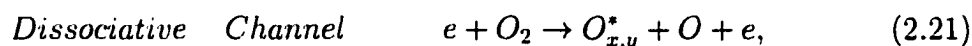
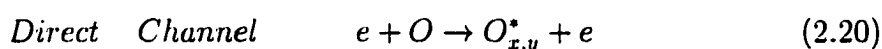


Figure 2.14:  $Ar + O_2$  plasma as a function of the oxygen composition in the source region (500W, 6.74mTorr)

With the addition of higher percentages of argon into the discharge chamber, the assumptions for actinometry may not be valid. In such cases, therefore, we plot both ratios of  $O_{777nm}(3p^5p)$  and  $O_{844nm}(3p^3p)$  lines to the  $Ar_{750nm}$  as functions of

percentage of oxygen in the mixture, while maintaining a fixed pressure. The ratios for both oxygen lines increase with increasing oxygen content. The initial increase is nearly linear as might be expected from a simple model where electron impact dissociation is followed by ionization of the atoms. The sudden jump to higher than linear dependence associated with increasing to greater than 85%  $O_2$  indicates a possible change in kinetics. Our result in Fig. 2.14 that the  $O_{777nm}$  and  $O_{844nm}$  lines behave similarly, is not always obtained in the plasma discharge studies [24]. The validity of using the  $O_{777nm}$  line to characterize the ground state O atom density must be examined in detail for each case [32]. The primary contributions to forming the excited state radiation are



where  $O_x^*$  indicates the upper state of 777Å line, and  $O_y^*$  indicates the upper state of the 844Å line. The excitation cross-sections for processes 2.20 and 2.21 have been measured [33,34]. Direct excitation cross-section for both  $O_x^*$  and  $O_y^*$  peaks at about 13 eV and rapidly falls off. The peak value for  $O_y^*$  is more than three times higher than that for  $O_x^*$ . Dissociative excitation has a threshold near 13~14 eV and rises slowly to broad maximum well above 70 eV. The cross-section for the dissociative channel for  $O_x^*$  crosses the direct channel at 20~25 eV. Dissociative excitation for  $O_y^*$  crosses direct excitation for  $O_x^*$  at about 30 eV, but is well below that for  $O_y^*$  direct excitation for values of energy out beyond 200eV. In our discharges with average electron energies below 14 eV and without significant higher energy tails during the

inductive portion of the discharge, the direct channel dominates and both emission lines are observed to be equally useful for inferring the ground state oxygen atom density. Our photo-resist cleaning results (Chapter 5) showed that the stripping rate increased with oxygen percentage, consistent with increasing atomic O concentration as more oxygen is added. For some stripping and cleaning applications, F atoms are helpful, so we also performed similar studies of  $CF_4/O_2/Ar$  mixtures, where the oxygen content was varied from 0 to 35%. As expected [35] F atom concentration increases with the rf power (Fig. 2.15) and can be dramatically increased by oxygen addition. The atomic oxygen concentration also increases with the rf input power.

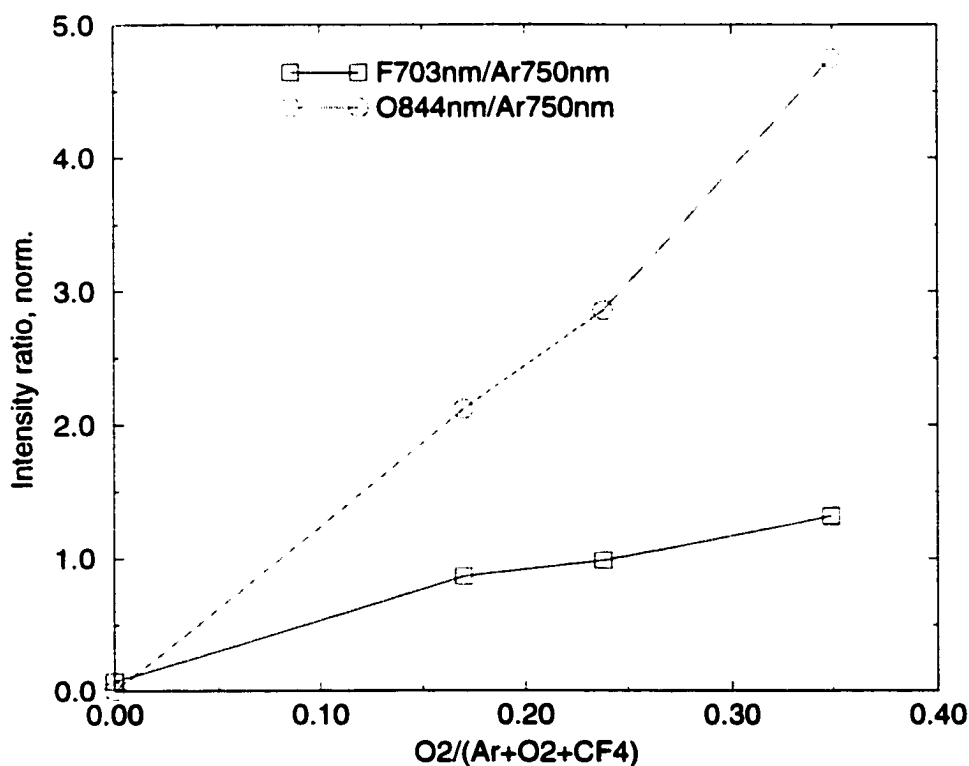


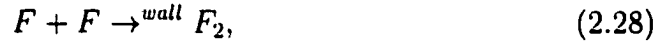
Figure 2.15: Optical emission spectra of  $Ar + O_2 + CF_4$  plasmas as a function of the discharge gas composition



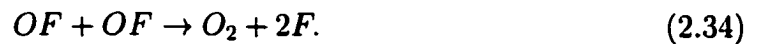
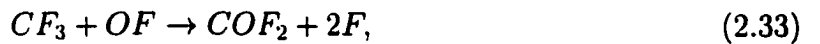
Without oxygen, F atoms in this discharge are mainly contributed by following reactions:



and fluorine atoms are lost by following reactions:



With the addition of the oxygen, one possibility is that oxygen reacts with fluorine-containing species to liberate the fluorine atoms. The reactions may occur on surfaces or in the gas phase. Mogab *et al.* [35] proposed the following reactions to account for the F density variation with the oxygen composition.



The expected decrease of F atom density as oxygen composition further increases is caused by a low dissociation rate of  $CF_4$  because electron energy decreases from a larger value (6~8.3eV) in pure  $CF_4$  discharge to a lower value (4.5~6eV) in pure  $O_2$  discharge. Thorough studies of reflected neutral F atom energy or angular distributions, or detailed studies of etch rates on materials of interest are needed.

A concern in the operation of a surface reflection neutral stream source is whether variation of the reflector bias changes the composition of the plasma or the neutral stream. Fig. 2.16 shows optical spectra of an  $Ar + O_2$  discharge as a function of the reflector bias. No detectable changes are observed. A downstream quadrupole

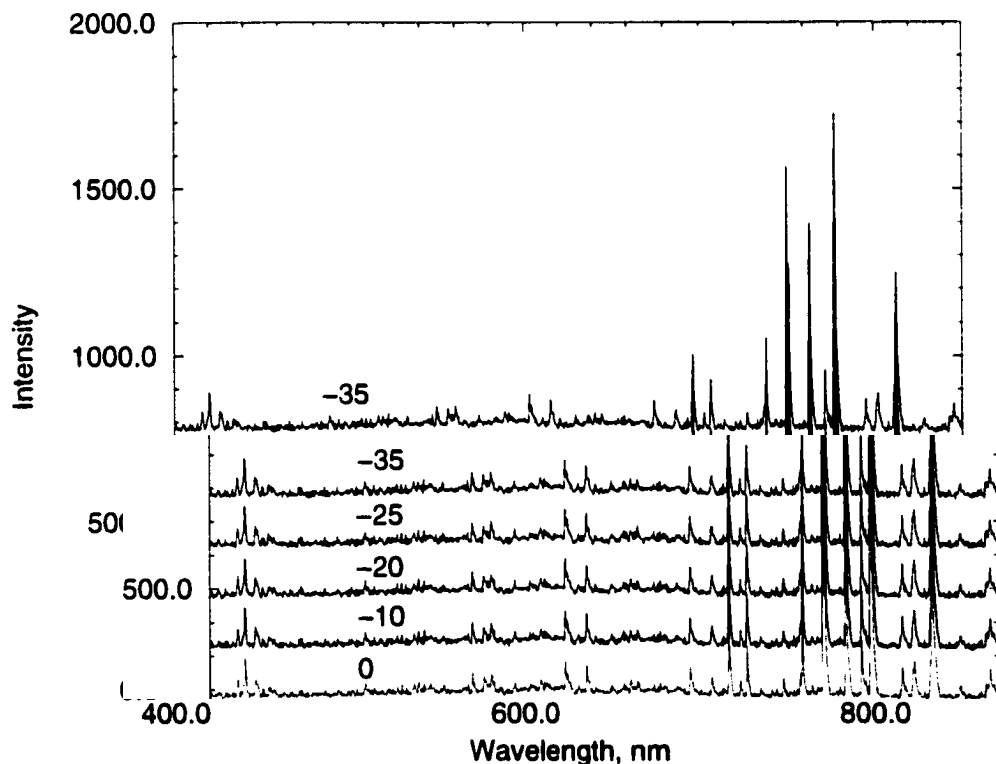


Figure 2.16: Optical emission spectra of  $Ar + O_2$  plasmas as a function of the reflector bias

mass spectrometer was used to examine the discharge composition as a function of the reflector bias. We note that results from mass spectroscopic studies also agree with the optical studies.

## **2.4 Summary**

In this chapter, a brief review the plasma diagnostic methods such as Langmuir probe and optical emission in the ICP source was presented. Plasma density and electron temperature as a function of the discharge pressure and rf power were measured from Langmuir probe measurements. Electron temperature derived from the OES indicates a possible mode jump in the discharge. As the reflector plate bias changes, no detectable OES spectra changes were observed. This indicates that changing the reflector bias, which changes the neutral energy, does not change the discharge composition. This finding has never been confirmed before and is essential to the use of such a source in advanced processing applications.

# Chapter 3

## Time-resolved electrostatic probe studies of a pulsed inductively coupled plasma

### 3.1 Introduction

The development of new plasma sources is of fundamental importance for plasma-based material processing. The need for sources that operate at low pressure, with a high degree of plasma uniformity and high plasma density, has led to the development of the radio frequency induction (RFI) and electron cyclotron resonance (ECR) sources. The transformer-coupled plasma (TCP) source has drawn attention due to its simplicity and its ability to perform large area processing. Pulsed plasmas, combining either TCP or ECR with pulsed power, offer the prospect of better control by variations of pulse shapes, durations, and duty cycles. For example,

Samukawa [36] reported an increased selectivity for  $\text{CHF}_3$  etching  $\text{SiO}_2$  over Si, by choosing an optimized pulsed-power repetition frequency in an ECR plasma source. Shin *et al.* [37] showed an enhancement of mask selectivity in  $\text{SiO}_2$  etching with a pulsed ICP (inductively-coupled plasma) source. These sources can also reduce process-induced damage, such as that caused by electron shading [38, 39]. However, most research in this area is devoted to the study of the quality of the etching or deposition by pulsed processes. The goal of this chapter is to establish the suitability of Langmuir probes for pulsed plasma measurements and to present the experimental results with more accurate data analysis approaches in order to understand the pulsed discharge mechanism.

Few direct measurements to understand the pulsed discharge have been performed. These include studies using quadrupole mass spectroscopy [40], optical emission spectroscopy [41], and microwave interferometry [42]. Compared to Langmuir probe measurements, these diagnostic tools provide volume-averaged or line-integrated plasma densities and present minimum interference to the plasma, but they are complicated and their costs can be high.

Electrostatic probes provide simple and reliable methods to analyze local properties of the pulsed plasmas with carefully designed probe circuit and data processing. Among earlier studies, Ashida and Lieberman [43, 44] reported the use of a single Langmuir probe to compare the measurement of a pulsed ICP to a spatially-averaged simulation model. Overzet and co-workers [45] compared time-resolved single-probe measurements to microwave interferometer measurements in parallel-plate pulsed discharges at 300-500 mTorr. Another type of Langmuir probe, the double probe, has

also been used previously to measure electron temperature and the plasma density [46]. A double probe circuit for use in pulsed ECR discharges was reported by Boegger [47]. More recently, Smith and Overzet [48] reported an improved double probe system for pulsed rf plasmas inside a Pyrex tube, finding a transition to an “electron-free” (positive and negative ions only) plasma arriving at the end of the power pulse [49]. A quantitative analysis of probe data must account for the sheath thickness variation in pulsed plasmas, which leads to tedious analysis. Thus processing a large amount of probe data using standard iterative, non-linear methods requires a large amount of computation time.

The relative merits of the single and double probes have been presented previously [17, 50]. We briefly touch on the relevant points here. The perturbation of the double probe to the plasma is generally smaller than that of a single probe since both probes are maintained at negative potentials so that the total current drawn by either probe is always less than or equal to the ion saturation current. Furthermore, the double probe analysis for the electron temperature based on the straightforward extension of single probe theory is relatively easy. Unlike the single probe, the double probe is insensitive to multi-modal electron energy distributions, being dominated by the population of high-energy electrons. It is necessary, therefore, to benchmark double probe results against other measurements for  $T_e$  and  $n_e$ , such as single probes or interferometry, to establish the suitability of double probes [17]. The apparatus under study in this chapter has been the subject of extensive single probe studies [14, 51], with which the present double probe measurements have been compared. Earlier studies in our group have demonstrated good agreement between double probes and

microwave interferometer measurements in rf driven plasmas [52–55]. In this chapter, we present time-resolved Ar, TCP (13.56 MHz) plasma measurements over the pressure range from 1 m Torr to 15 m Torr at pulse repetition rates from 200 Hz to 10 kHz. Our analysis fully accounts for sheath thickness variation. The results from single and double probes, which are analyzed using both nonlinear fitting and equivalent resistance methods, are compared. Plasma density radial profiles are also presented. The temporal dynamics of the electron temperature and the plasma density are discussed in terms of current models [56–58].

## **3.2 Experiment**

### **3.2.1 Setup**

The schematic drawings of the single and double probe measurement circuits are shown in Fig. 3.1. The discharge chamber has been described in Chapter 2. An HP8116A function generator gates 13.56 MHz cw sinusoidal waves with 50 Hz–15 kHz rectangular pulses, created by either a Wavetek 20 function generator or a HP8004A pulse generator. The gated rf signal is amplified by an ENI A-300 power amplifier. The calibrated, absorbed plasma power is measured by a Pearson 110 current monitor, capacitive voltage probe, and 5 kw dummy load following the procedure described by Wainman [59] and Asida [43]. The measured rise time and the decay time from full power to zero power of the rf pulsed power circuit are both about  $2\mu\text{s}$ . A time-averaged rf power of 65 W is used in all experiments unless otherwise stated.

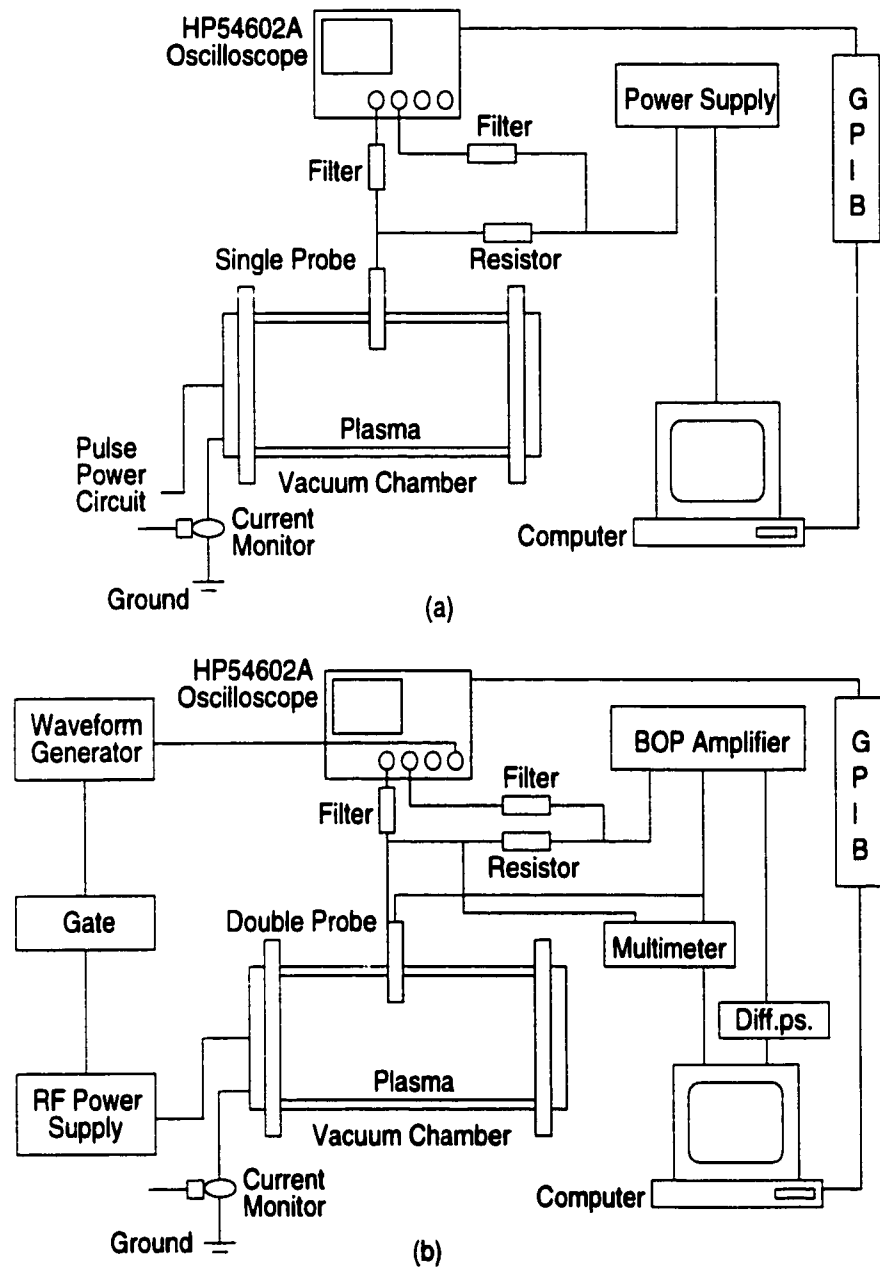


Figure 3.1: Schematic drawings of Langmuir probe setup for the pulsed plasma characterization, (a) single probe. (b) double probe.



The pulsed ICP plasma parameters are characterized by both a single probe circuit and a real-time, double probe system. They are placed about 7 cm downstream of the quartz window in the discharge chamber. The single probe is made of a cylindrical tungsten wire, seated in a ceramic tube. The double probe is made of two cylindrical W wires, 100 $\mu$ m diameter and 1cm long, seated 0.8 cm apart in a double-bore ceramic tube. The two probe tips thus were separated far enough from each other so that neither probe tip will sit in the other's sheath. Both probes can be mounted on a bellows-drive, permitting motion in the radial direction to collect the radial profiles.

Several experimental issues have been taken into consideration for pulsed rf plasma measurements:

- rf chokes are placed inside the stem to prevent the rf from distorting the I-V traces. Both probes are trapped for the fundamental, second, and third harmonics [60]. Several low pass filters are used to further eliminate the rf interference to both single and double probes. These low pass filters have over -45 db attenuation for signals at 13.56 MHz and less than -0.1 db attenuation for 50 to 15 kHz modulation signals. The collected signal is carried by coaxial cables, which provide the necessary shielding.

- Ground leads from the oscilloscope, rf power supply, and discharge chamber in the single probe circuit, are bundled up to a common clean ground. External circuit connections are shielded by additional metal foils. For double probes, no ground lead is connected to the oscilloscope input terminal or to the bias power supply output terminal; this permits the double probe circuit to float.

- The full record of time variation of the plasma is constructed pulse-to-pulse by adjusting the time gate of the measured current and voltage, in a manner analogous to a conventional box-car amplifier. The voltage applied to the probe is varied slowly to capture the dynamical development of the plasma. The applied voltage remains constant during one cycle of data acquisition so that measurements of the fast plasma transients are easier to record, avoiding probe dynamic effects. Each collected I-t waveform, at each probe bias, is constructed by accumulating 256 repetitions of the applied pulse trains, averaged in the oscilloscope. Fast Fourier transform (FFT) analysis of I-t traces reveals no detectable rf-induced noise.

- Plasma leakage and stray capacitance often limit the use of Langmuir probes, especially double probes. The direct use of a standard, stabilized dc power supply to bias the probes produces unacceptable results because of the large capacitance to the ground at each of output terminals. In our setup, a computer-controlled, bipolar amplifier, driven by a battery-powered bias circuit, provides a floating differential voltage to the probe tips. The measurement circuit capacitance is assessed in a pulsed plasma by measuring the current,  $I_{leak}$ , through the probe resistor with zero bias voltage. This stray current contributes to the probe current at the end of a power pulse period with a magnitude observed to be less than 10 percent of the total ion saturation current. The temporal structure of the stray current is highly reproducible, allowing this background offset to be subtracted from measured current in subsequent ion saturation calculations. We also evaluate stray capacitance effects by applying a 50Hz-15kHz sine-wave ( $V_{p-p} = 1V$ ) to both electrodes, measuring the resultant probe current.

- The load resistors for the single probe and double probe analysis are 5 k $\Omega$  and 900  $\Omega$ , respectively. The 5 k $\Omega$  load resistor was chosen so that we could directly compare our results to those by Ashida who use the same value while employing different data analysis approaches. For our double probe measurements, different load resistor values, 100, 500, 900, 1000, 1500  $\Omega$  have also been tested. The collected I-V traces overlap within a few percent, indicating that all of these values are smaller enough not to alter the probe load-line. A 900  $\Omega$  resistor is chosen to provide adequate gain for use in O<sub>2</sub> pulsed plasmas, which have significantly lower probe currents than Ar plasmas.

- Prior to each argon data collection sequence, the probe is biased at -65 volts for one hour to clean the surface. The time-resolved electron temperature is derived from I-V traces by transecting the I-t data matrix at different biases. The electron temperature is then input to a procedure which iterates on  $\frac{r_p}{\lambda_D}$  to extract the plasma density from the corrected ion current.

### 3.2.2 Probe theory and data analysis

The electrostatic probe theory for charged particle densities and electron temperatures in low to medium pressure plasmas is well established for dc discharges in inert gases [61, 62]. Its applications for rf plasma measurement have been reported by Hopwood [63], and Ruzic and Wilson [64], Wilson *et al.* [65], Cox *et al.* [66], Gudmundsson *et al.* [67], and Crawford [68]. Such applications have been reviewed in detail by Hershkowitz [50] and Cherrington *et al.* [69]. For completeness, we include a brief discussion of the established theory. Since the electron plasma frequency is typ-

ically much higher than the radio frequency used in an ICP plasma, the electrons will react to the rf while the ions do not because of their larger mass. Thus an rf fluctuation in the plasma potential distorts the dc characteristic. The probe measurements only provide a time-averaged I-V characteristic [70]. Godyak and Piejak [71] have demonstrated the relationship between the probe-plasma impedance  $Z_{sh}$  and the external probe circuit impedance  $Z_c$  which must be fulfilled to achieve reasonable probe I-V traces in rf plasmas. There are also hardware means to compensate externally for the signal created by the plasma, for example the use of driven rf probes [72–75].

We will briefly review the existing sheath relation and derive an expression useful for applications in pulsed plasmas. Two collisionless models, Laframboise’s orbital-motion-limited (OML) model [76, 77] and Allen, Boyd, Reynolds [78, 79] (ABR)-Chen radial motion cold ion approximation model are employed to extract the plasma parameters based on  $\frac{r_p}{\lambda_{de}}$ , where the Debye length  $\lambda_{de}$  is  $[kT_e/4\pi n_e e^2]^{1/2}$ , and  $r_p$  is the probe radius. Detailed sheath theories have been discussed extensively by Wendt [80], Godyak [81, 82], and Lieberman *et al.* [83].

In general, pulsed plasmas experience a sequence of thick sheath to thin sheath to thick sheath transitions represented by a changing ratio of  $\frac{r_p}{\lambda_{de}}$ . As a first approximation, one might try to estimate the plasma density, without electron temperature dependence, using

$$n_i = \frac{I_i}{er_p l_p \sqrt{-8e(V_{pr} - V_{pl})/m_i}}, \quad (3.1)$$

where  $I_i$  is the ion saturation current,  $m_i$  is the ion mass,  $e$  is the electron charge unit,  $r_p$  is the Langmuir probe radius,  $l_p$  is the Langmuir probe length in the plasma,  $V_{pr}$  is the probe bias and  $V_{pl}$  is the plasma potential. This approach, ignoring the electron

temperature variation, overestimates the calculated density through the entire period. In this chapter, the plasma density is calculated by employing both Laframboise's orbital motion limit theory Eqn. 3.2 and radial motion theory Eqn. 3.3 derived for single probe analysis.

$$n_i = \frac{I_i}{er_p l_p \sqrt{2\pi k T_e / m_i} J_1}, \quad (3.2)$$

where  $J_1$  is the unitless numerical correction tabulated by Laframboise for various  $\frac{r_p}{\lambda_D}$  [76]. Several iterations are necessary to recalculate  $\frac{r_p}{\lambda_D}$  to verify the validity of sheath theory in different regimes until the plasma density value converges [84]. Eqn. 3.3 may be only used after a stable thin sheath has built up.

$$n_i = \frac{I_i}{0.5eA_p u_b}, \quad (3.3)$$

$$u_b = \sqrt{eT_e / m_i}. \quad (3.4)$$

where  $A_p$  is the current collection area of the probe. The above derivation requires knowledge of the electron temperature extracted from a nonlinear regression Levenberg-Marquardt fit. Such an approach is necessary because the sheath and orbital effects associated with cylindrical probes do not result in a constant value of ion saturation current in the asymptotic region [17].

One complication using probes in pulsed plasma measurement is accounting for the sheath displacement current [85]. We subtract the sheath displacement current from the measured saturation current to derive the ion saturation current for the decay period. A good approximation of the sheath displacement current is

$$I_s = 0.5n_i A_p e \frac{ds}{dt} \quad (3.5)$$

where  $s$  is the Langmuir-Child sheath width, and  $\frac{ds}{dt}$  is the sheath edge velocity. According to Lieberman's collisionless model [83]:

$$s = 0.880\sqrt{\epsilon_0}(e/m_i)^{1/4}V_{dc}^{3/4}J_i^{-1/2}, \quad (3.6)$$

where  $V_{dc}$  is the dc sheath voltage,  $J_i$  is the measured current density. As we bias the probe at a highly negative potential, the dc sheath voltage is approximately equal to the probe bias. We can combine these existing relations to derive an expression for the single probe saturation current in terms of the current density. Hence we can write:

$$I_s = 0.44n_iA_p e \sqrt{\frac{\epsilon_0}{T_e}}(em_i)^{1/4}V_{dc}^{3/4}(dJ_i^{-1/2}/dt). \quad (3.7)$$

The double probe theory has also been well developed [86–92]. The derivation follows as a straightforward extension of the single probe theory. The general expression of the electron temperature for the double probe analysis is similar in dc and rf plasmas.

Assuming a Maxwellian electron energy probability function for the double probe system, after the removal of  $I_{eak}$ , the electron temperature can be written as:

$$T_e = \left(\frac{I_1 I_2}{I_1 + I_2}\right)\left(\frac{dI}{dV}\right)^{-1}|_{v=0}, \quad (3.8)$$

where  $I_1$  and  $I_2$  are the ion saturation currents for the two probe tips respectively and  $T_e$  is the electron temperature value in volts. The calculation of the derivative,  $\frac{dI}{dV}$  adds numerical noise to the result. The smallest  $T_e$  that can be measured is limited by the minimum bias step size.

In the equivalent resistance method, the standard double probe expression is

recast to write a simplified expression for the electron temperature: [93, 94]

$$T_e = \frac{e}{4k\Sigma I_p R_0(1 + \epsilon)}, \quad (3.9)$$

where  $R_0^{-1}$  is the slope of the current-voltage characteristic evaluated at  $V=0$  for double probes.

The complexity of the orbital motion and sheath effects is absorbed into the model parameter  $\epsilon$ . The parameter  $\epsilon$  [94] depends mainly on the ratio between the probe radius and Debye length.  $\Sigma I_p$  is the sum of the positive ion current for both probes when the differential probe voltage is zero. It is extracted from the I-V curve at  $|V| > 10$  volts. The calculation of  $R_0^{-1}$  limits the minimum electron temperature measured. Using a 12-bit or higher resolution data acquisition board can not solve this problem. The analysis will no longer be valid during the pulse-off period at low modulation frequencies (less than 500Hz), therefore results from a full non-linear fit will be presented for that regime. In our full nonlinear regression data analysis, ion saturation currents are also corrected for extraneous contributions discussed above:

$$I = I_{sat} \tanh(V/2T_e) + I_{leak} + I_{other}, \quad (3.10)$$

where  $I_{other}$  represents a constant dc offset associated with the probe setup and the floating amplifier.

## **3.3 Results and Discussion**

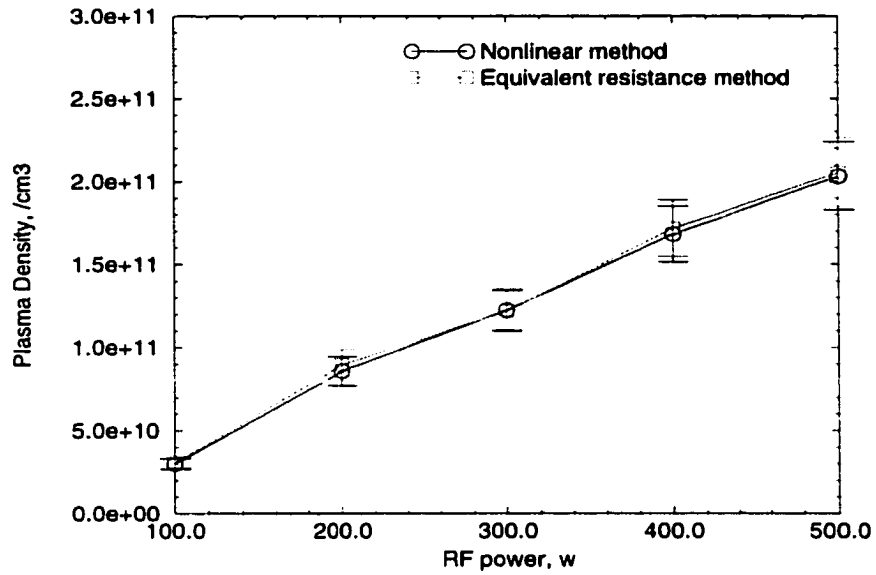
### **3.3.1 Langmuir probe measurement results for cw rf plasma**

Fig 3.2 shows results for the double probe measurement with a cw rf Ar plasma, collected at 7.8 mTorr. The agreement between the two different data interpretation methods is evident, though the nonlinear fitting requires an order of magnitude more computation time than the equivalent resistance method. The electron temperature drops precipitously between an rf power of 100 W and 200 W, associated with a transition from a capacitively-coupled mode to an inductively-coupled mode, with a concomitant increase in the electron density. The plasma density shows a linear relationship with rf power above 200 W. We have followed Lieberman's global model [43,56] to perform spatially averaged modeling of our discharge. We will not describe these calculations here since they are identical in form to the model described in those references. The spatially averaged model indicates that the electron temperature of the steady ICP plasma is mainly a function of the discharge geometry and the neutral particle density. This model also predicts that increasing the rf power increases the plasma density without much effect on the electron temperature. This agrees with our observed experimental results.

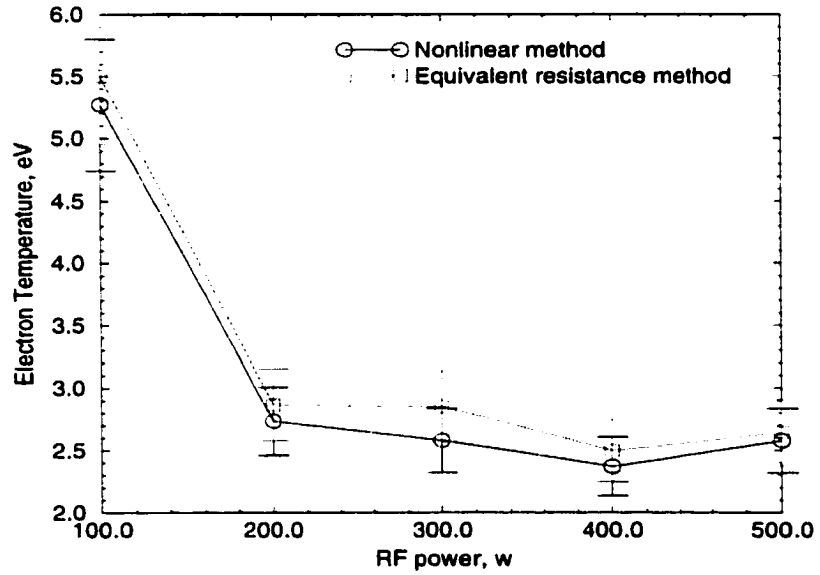
### **3.3.2 Single probe measurement for pulsed plasma**

Fig 3.3 shows the result using single probes for a pulsed ICP plasma, modulated at 1000Hz. The plasma density during power-off period has been corrected for the sheath displacement current. The results agree with Ashida's measurements [43],





A: Plasma Density



B: Electron Temperature

Figure 3.2: Plasma density (A) and electron temperature (B) from double probe measurements for the cw Ar Plasma at 7.8 mTorr with two fitting methods.

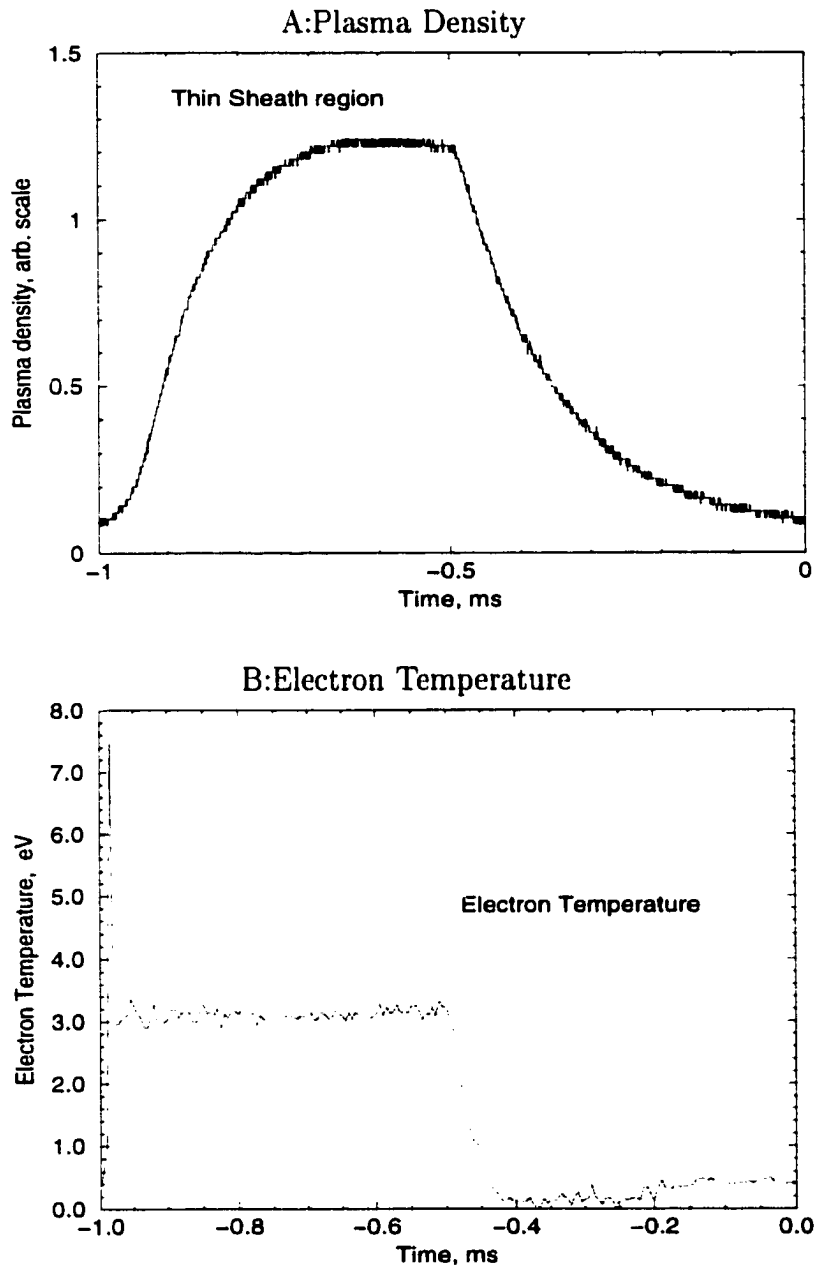


Figure 3.3: Single Langmuir probe measurements of  $n_e$ ,  $T_e$  for an Ar pulsed plasma at 1000Hz.(average power: 65W, duty cycle: 50%, 7.8mTorr. Note: The coil current scale is arbitrary)

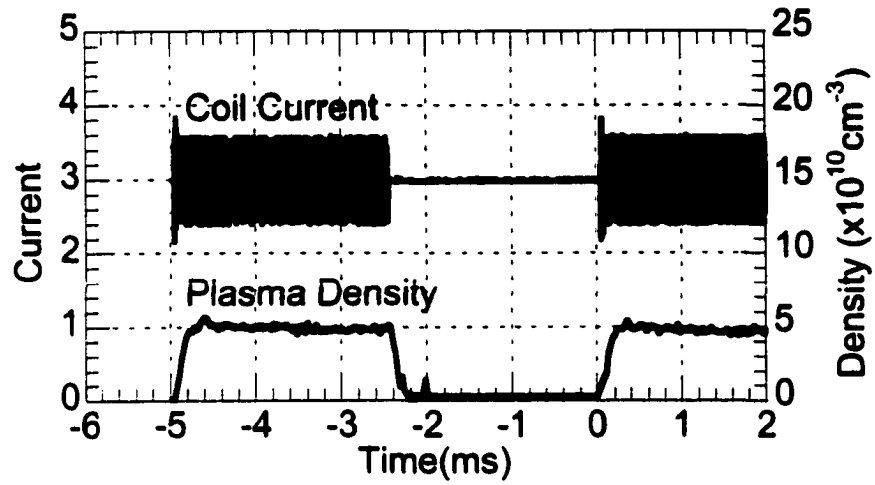
though the plasma density seems to decay slower than expected from the spatially averaged model. The sheath displacement correction causes a slight shift( about  $10 \mu s$ ) in the plasma density decay curve. The electron temperature decays much faster than the plasma density. A large electron temperature jump is observed at the beginning of the power pulse. This jump becomes less pronounced at higher pulse frequencies. We discuss this feature in detail below. The above transient electron temperature and plasma density variations agree with our spatially averaged simulation. At lower pulse frequencies ( 50-200 Hz), the plasma density appears to increase with a single rise-time at the onset of the pulse. At high frequencies, the density increases with two distinct rise times during the beginning of the pulse.

We note here that both a single and double probes have sources of systematic uncertainty which have been discussed in the various reviews mentioned above. Earlier comparisons of density and temperature to other measurement methods such as microwave interferometry or Thomson scattering indicate that the absolute accuracy of probe measurements is probably not better than  $\pm 30\sim 50\%$ , in general. After an initial, careful cleaning of the probes, contamination during the course of an experimental series did not appear to be a major issue in these studies. Returning to the same conditions after a period of hours yielded experimental traces within the noise envelope of a single trace. We cannot say that adsorbed layers do not form on the tungsten, for it is likely that they do. However, it appears that they formed quickly and remained stable in terms of their influence on ion or electron collection (including secondary electron emission effects) in these experiments. Such behavior may not be expected to happen for the general case of reactive gases.

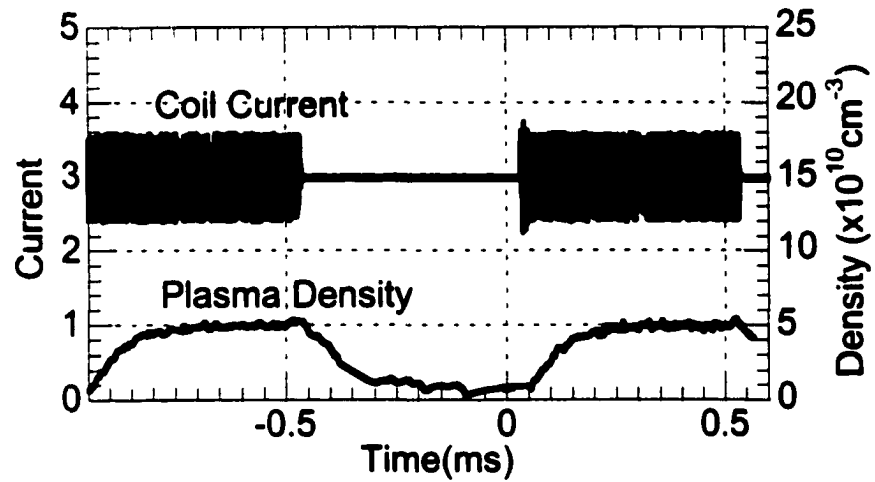
### 3.3.3 Double probe measurement for pulsed plasma

Fig. 3.4 shows experimental measurement of the plasma density for various choices of rf power modulation periods. The corresponding electron temperature variations, which are extracted from the same double probe traces, are plotted in Fig. 3.5. All of the data were taken at 50 % pulse duty cycles. The plasma current through the antenna as a function of time is also shown in these figures.

The equivalent resistance method is used for above analysis except for the result at 200Hz pulse frequency because of the measurement limit stated earlier in the experimental section. The peak electron density value of the 1kHz pulse plasma is slightly smaller than that of single probe measurements; the maximum deviation at any time is less than 15 percent. The nearly constant rise time of the density, about 0.1 ms, is consistent with a diffusional filling of the radial profiles. Therefore, in the 0-D modeling below, we do not expect to correctly capture this short time scale rise. The electron temperature value from the double probe results is comparably higher than that of the single probe. The comparison shows good agreement in trends of the plasma density and electron temperature variation for single and double probes. The short period data gives a clear measure of the density in the afterglow. For example, this can be seen in Fig. 3.4(d). In short pulses, the highest plasma density generally appears at the end of rf power pulse. The electron temperature behaves differently. The electron temperature plotted in Fig. 3.5 shows a jump at the onset of the rf power(see below). We will also discuss this jump in connection with the plasma model of Chapter 4.

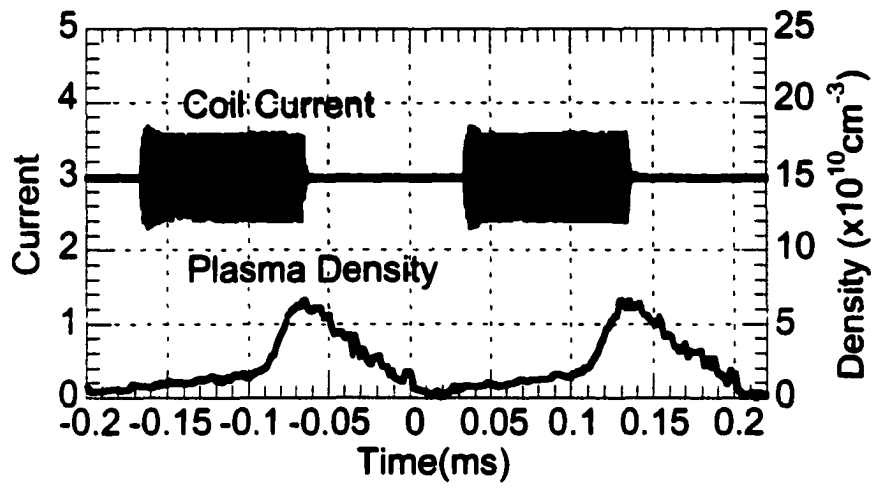


(a) 200Hz

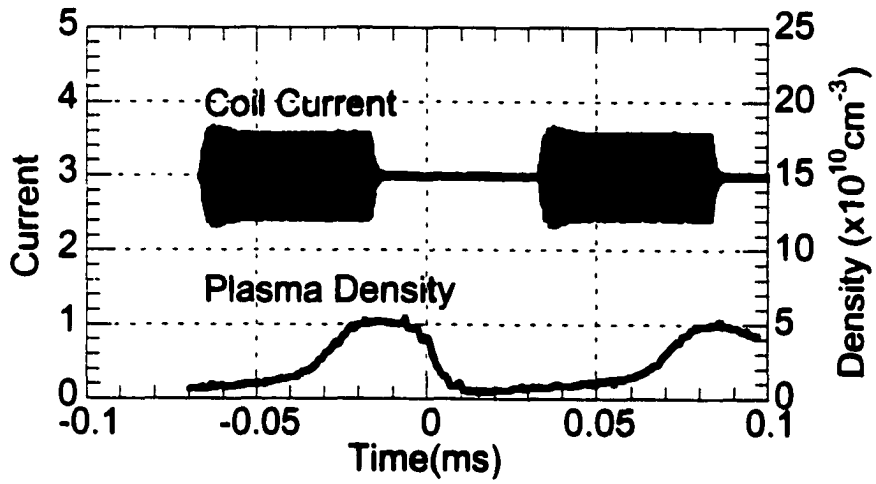


(b) 1000Hz

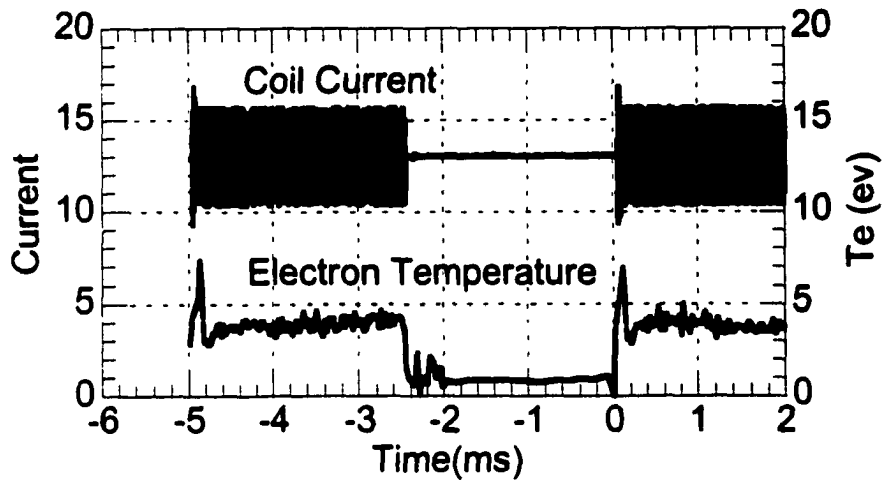
Figure 3.4: Calculated plasma density as a function of pulse frequency from the double probe measurement. (a) 200 Hz, (b) 1kHz, (c) 5kHz, and (d) 10 kHz. Note: the coil current scale is arbitrary.



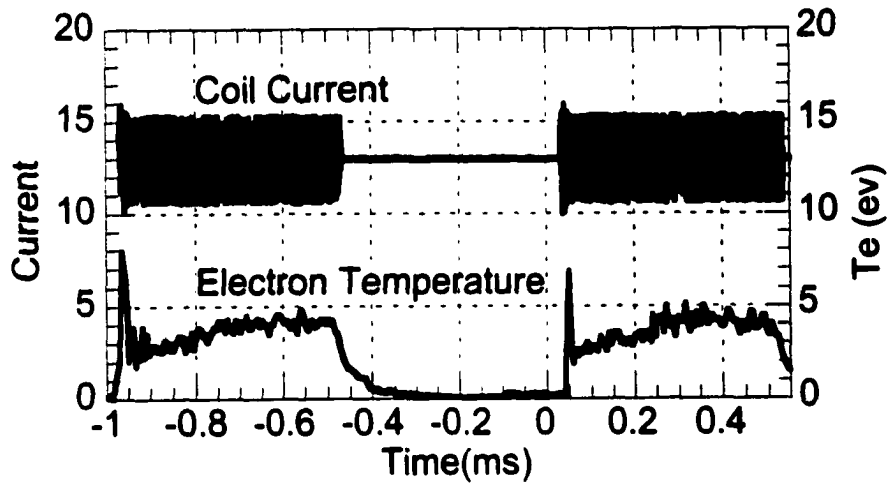
(c) 5000Hz



(d) 10kHz

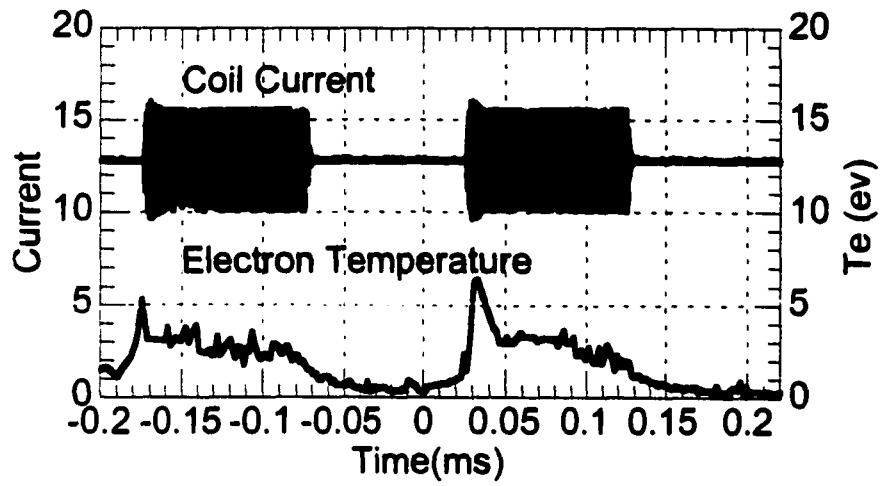


(a) 200Hz

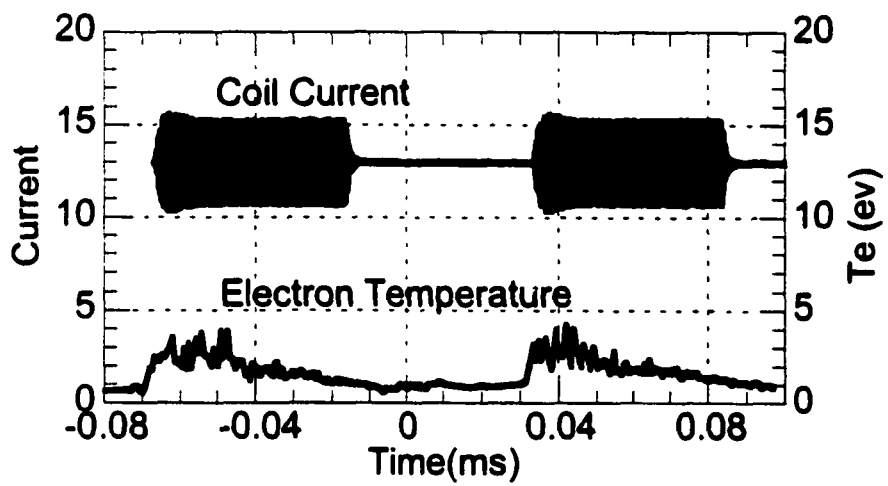


(b) 1000Hz

Figure 3.5: Calculated electron temperature as a function of pulse frequency from the double probe measurement. (a) 200 Hz, (b) 1kHz, (c) 5kHz, and (d) 10 kHz. Note: the coil current scale is arbitrary.



(c) 5000Hz



(d) 10kHz



From the double probe measurements(Fig. 3.6), the time-averaged plasma density is

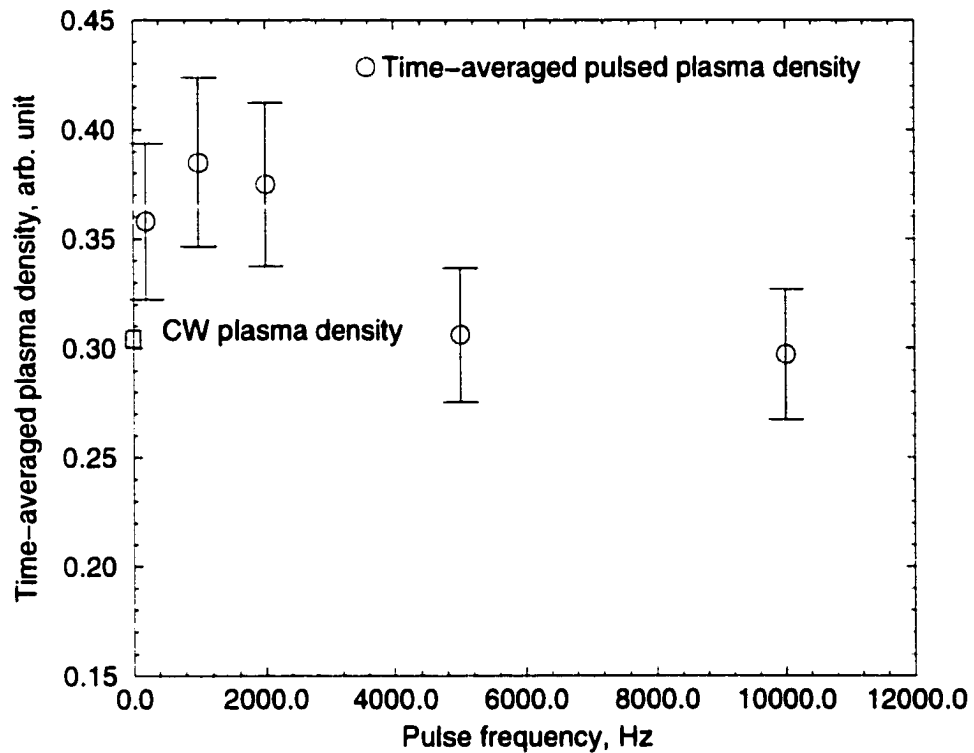


Figure 3.6: Time averaged plasma density as a function of the pulse frequency from double probe measurements (65 W,7.8mTorr, 50 % duty cycle)

a function of the pulse frequency. The time-averaged plasma density reaches a maximum at about 1000 Hz pulse frequency. As the modulation frequency increases from 1000Hz to 10 kHz, the time-averaged plasma density starts to drop. The same trend appears as the pulse frequency decreases from 1000Hz to lower frequencies. The existence of such a maximum in average plasma density has also been seen in calculations of time-averaged generation and loss rates in pulsed plasmas.

The electron temperature versus time generally follows the temporal envelope of the pulsed power for long pulses. The jump at the start of the rf power pulse shown in Fig 3.5 is due to heating by the capacitive electric fields in the low-density plasma at the start of the rf pulse. As the pulse frequency is further increased, the ions and electrons do not have enough time to be completely lost by transport to the chamber wall after the pulse. This trend persists to much higher frequency until the remnant plasma density from one pulse is carried into the following one, providing enough electrons for inductive heating without a preliminary capacitive build-up period from the start of following pulse. This sort of electron temperature jump has also been simulated by Yokozawa *et al.* [95] in pulsed ECR  $Cl_2$  plasmas. In all cases, the electron temperature starts to decay immediately after the power is turned off. For the shortest period in the measurement, the average electron temperature is lower than the value (2.6eV) for CW rf case with the same time-averaged power. Thus a pulsed plasma can have a lower time-averaged electron temperature when compared to a continuous mode plasma with the same average power.

In addition to the spatially averaged modeling, we follow the treatment of Sugai and co-workers [58] to estimate the time scale of the cooling of  $T_e$ . The electron energy balance equation is given by:

$$V \frac{\partial E}{\partial t} = P_{rf} - P_{coll} - P_{esc}, \quad (3.11)$$

where  $P_{rf}$  is the RF power input,  $P_{coll}$  is the power lost by collisions to neutrals,  $P_{esc}$  is the power lost by escaping from the plasma to the walls and  $E$  is the electron kinetic energy density averaged over the plasma volume  $E = n_e(3kT_e/2)$ .  $P_{rf}$  vanishes at the end of the pulse. Assuming that  $P_{coll} \ll P_{esc}$ , the power loss to the wall of surface

area  $A$  is given by:

$$P_{esc} = n_w u_b E_e A, \quad (3.12)$$

where  $n_w = n_e/4$  is the average electron density at the sheath edge,  $u_b = (kT_e/m_i)^{1/2}$  the Bohm velocity, and  $E_e \sim 2kT_e$  the average energy of the escaping electrons. For our cylindrical chamber,  $A = (2\pi RL + 2\pi R^2)$  and  $V = \pi LR^2$  (our setup has  $L = 8\text{cm}$ , and  $R = 7.5\text{cm}$ ). Note that since  $n_e$  and  $T_e$  are time dependent,  $P_{esc}$  is also time dependent. Substituting these relations, with the electron temperature  $T_e$  normalized to its initial value  $T_0$  at  $t = 0$ ,

$$\tau_e = 3LR(m_i/kT_0)^{1/2}/(L + R). \quad (3.13)$$

For our experiments with argon,  $kT_0 = 1.8 - 4\text{ eV}$ , which gives rise to a time constant  $\tau_e$  of 38 to 57  $\mu\text{s}$ . This is in good agreement with our measured decay time constant of 39 to 63  $\mu\text{s}$  for 200Hz  $\sim$  10kHz pulse operations.

Lieberman *et al.* [15] have analyzed the time scale of the electron density decay giving an estimate from the ambipolar diffusion equation:

$$\frac{\partial n}{\partial t} = D_a \left( \frac{\partial^2 n}{\partial r^2} + \frac{1}{r} \frac{\partial n}{\partial r} + \frac{\partial^2 n}{\partial z^2} \right) + \nu_i n, \quad (3.14)$$

where  $D_a$  is the ambipolar diffusion coefficient and  $\nu_i$  is the ionization frequency. In the limit of a small ionization rate  $\nu_i = 0$  during the pulse-off period, the decay time is roughly  $\tau_n \sim L^2/D_a$ . In our case, the plasma source has  $L = 8\text{cm}$  and the ambipolar diffusion constant  $D_a = u_i(kT_e/e)$  for  $T_e \gg T_i$ . If we use the peak magnitude of transient electron temperature  $kT_e = 3.2\text{ eV}$  from Fig.3.3(b) to estimate the decay time, the characteristic decay time constant is about 213  $\mu\text{s}$ , agreeing well with the

measured  $240\mu s$  in Fig.3.3(a). For the double probe results at 1000Hz in Fig.3.4 and Fig.3.5, the estimated decay time constant is  $195\mu s$  while the measured time constant is about  $210\mu s$ . Our spatially averaged model calculations also predict a decay time of about  $200\mu s$ , in good agreement with the measured values. Thus the plasma density is not expected to completely disappear in the after-glow regime above a pulse frequency of 5 kHz. This is verified by the plasma density measurements.

The rise time for  $T_e$  during short rf pulses is too difficult to measure with voltage-swept Langmuir probes. Our observed electron temperature jump at the beginning of the pulse for longer periods is in agreement with Ashida's data and our simulation results. The simulation reveals such a short rise time (20 nanoseconds) for the electron temperature that makes it impossible to capture the jump even using the above probe setup. As the pulse repetition rate is increased to 10kHz, the electron temperature keeps increasing for a while during the pulse-on period. However, the modulation frequency at which the highest time-averaged plasma density appears is different from Asida's results. The electron temperature, which determines the particle generation rate and affects the loss rate, is a strong function of the discharge geometry. The difference in our discharge geometry from the Ashida's ( $R=15\text{cm}$ , and  $L=7.5\text{cm}$ ) accounts for the observed difference in behavior. Fig. 3.7 shows the transient plasma density of pulsed plasmas with different duty cycles but having the same average power input of 60W.

At the same discharge pressure, the plasma peak density at the end of the pulse is a function of the duty cycle. For the same time-averaged rf power, the smaller the duty cycle, the higher the plasma peak density. An rf power pulse with a small duty

cycle for the same time-averaged power in Fig. 3.7 implies a larger rf power input during the on-period of the pulse. As expected, since plasma density appears to be a

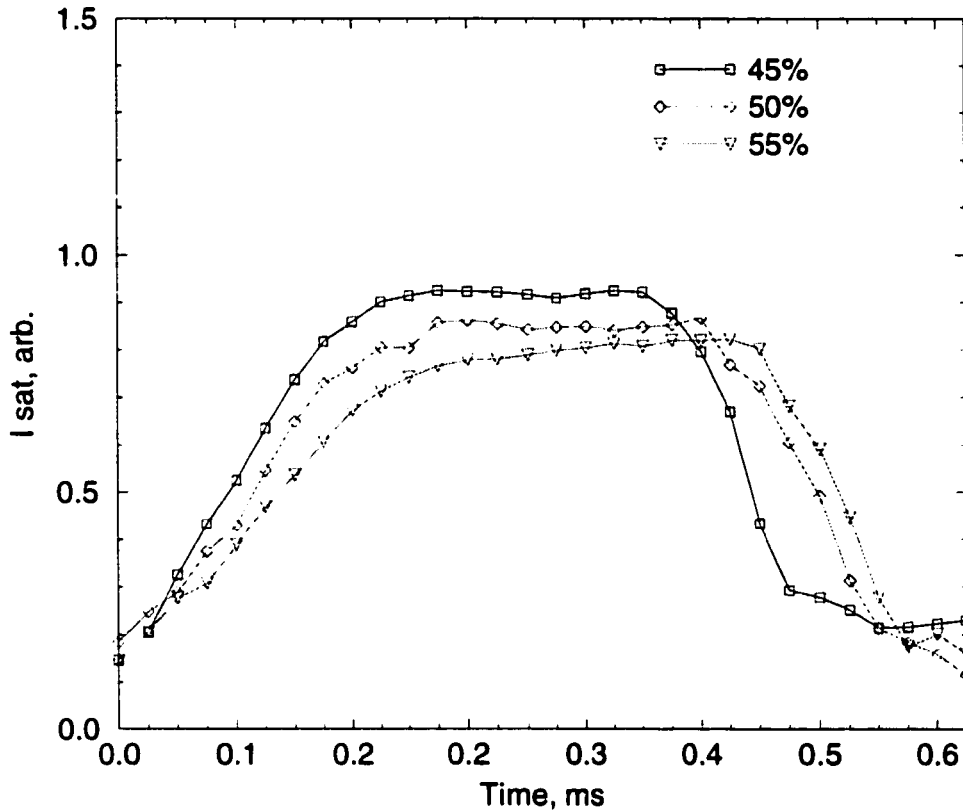


Figure 3.7: Measurements of double probe ion saturation current as a function of duty cycles with the same time-averaged power.(60W,7.8mTorr,Ar plasma)

linear function of the rf power input, we observe a higher plasma density at shorter duty cycles. Electron temperature measurements with different duty cycles show that the electron temperature jumps at the start of each pulse, but the average electron temperature does not vary much for the duty cycles used in our experiments. With approximately same average electron temperature, we do not expect much difference

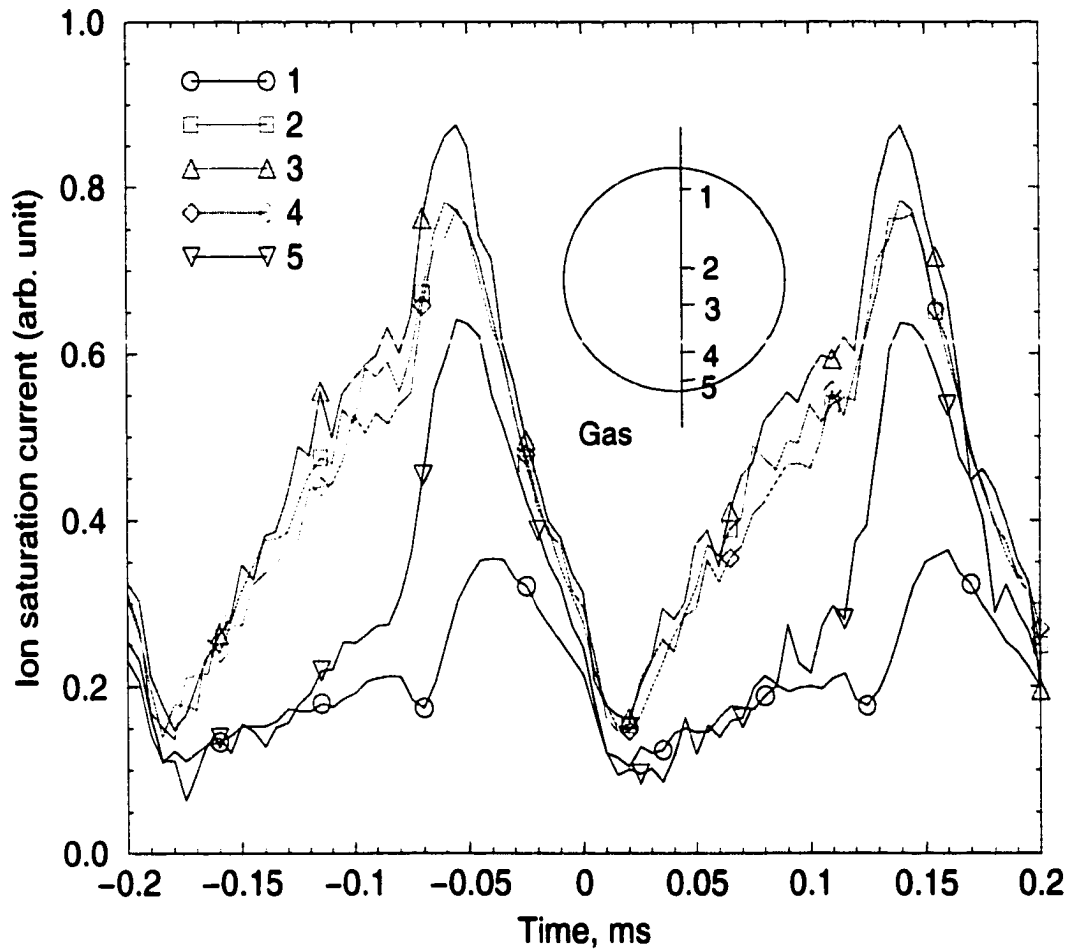


Figure 3.8: Two cycles of time profiles of  $I_{sat}$  at various locations in a 65 W pulsed plasma having 64 % duty cycle. Numbers 1-5 represent the radial positions that the data are collected. (Ar plasma, 7.8 mTorr)

in decay time between different duty cycles. Though the capacitive transients can lead to a relatively high electron temperature at the beginning of the pulse, the particle density during that phase is very low, so the integrated fluence of fast electrons is low. Also, judicious selection of frequency can minimize this transient electron

heating. Hence it is possible to achieve a high average plasma density and relatively low electron temperature by adjusting the duty cycle and the pulse frequency simultaneously. The radial profile of time-resolved ion saturation current distribution is shown in Fig. 3.8.

The plasma density shows non-uniformity mainly caused by an asymmetric gas inlet from the chamber sidewall. This non-uniformity is possibly compounded by having a toroidal electron heating region adjacent to the quartz window [63,96,97].

### **3.4 Summary**

Our experiments using both single and double probes have shown that the double probes can be used reliably to characterize pulsed TCP plasma properties over a range of pulse frequencies from 200 Hz to 10 kHz. Single probe data analysis, with sheath displacement current correction and utilization of both orbital-motion-limited and radial motion theories, shows good agreement with double probe measurements. The equivalent resistance method used for the double probe analysis agrees with results from the full non-linear fit and requires much less computation time. Using these powerful tools we have been able to examine the most important aspects of the use of pulsed rf in our neutral source. The time scales of the plasma density and electron temperature decay for an argon pulsed plasma, are in accord with simple models of the discharge. Results demonstrate the plasma density and electron temperature can be partially decoupled in a pulsed plasma. This decoupling permits additional control for ion-assisted or neutral-assisted etching and deposition.

# Chapter 4

## Global Average Simulation of a Inductively-Coupled Plasma Source

### 4.1 Introduction

Transformer-coupled-plasma (TCP) sources, which typically operate at low pressures of 1-20 m Torr and high input powers of 1-3 kW, are more preferable than conventional parallel plate reactors. The power absorption in a TCP source is typically inductive although, as indicated in earlier section of this dissertation, there is a contribution from capacitive coupling which can dominate at low rf power. Utilization of modulated power has attracted much attention recently. Pulsed process induces much less damage to the wafer by changing the pulse shape, duty cycles, and periods [36]. In addition, pulsing the plasma can increase the etching selectivity and



can suppress the particulate formation. Sugai *et al.* [58] and Samukawa *et al.* [36] reported increased etching selectivity by controlling the duty cycles of the pulsed power. Charge build-up damage can also be reduced in pulsed ECR discharges because negative ion fluxes incident on the substrate during the afterglow of a pulsed electro-negative ECR discharge can neutralize the positive charge accumulating during the pulse-on period. Many experimental measurements have been done to analyze the pulsed discharge. Ashida *et al.* [43], Sugai *et al.* [58], and Ahn *et al.* [98] reported Langmuir probe studies of time-varying plasma density and electron temperature in pulsed ICP discharges. Such analyses offer a fundamental understanding of mechanisms governing pulsed processes and help to design better reactors and to find the operating parameters for pulsed discharges.

There are several simulation models for CW plasmas. A spatially-averaged (global) model for atomic and molecular gases, and their mixtures has been given by Lee and Lieberman *et al.* [15,56]. Compared to other simulation models, this global average model takes much less computation time and provides direct insights into the plasma discharge chemistry. A generalized power balance including energy-loss channels for electron-neutral collision processes such as rotational, vibrational, electronic excitation, dissociation, ionization dissociative attachment, and electron detachment for molecular gases is used. In addition, energy-loss processes for heavy particle collisions such as ion-ion recombination are also included. Detailed particle balances are written for all species of interest. For charged particles, the appropriate ambipolar diffusion rates are used to determine the positive-ion losses. The complete set of equations is solved self-consistently to obtain all species concentrations and electron

temperature. Using a simple version of this model, Ashida *et al.* [57] investigated the behavior of argon plasmas driven by time-modulated power in high-density plasma reactors. The time evolution of the electron temperature and the plasma density was calculated by solving the particle and energy balance equations. For pressures and absorbed powers measured, the excited Ar states affected the calculated plasma density by at most 25 % and had practically no effect on the electron temperature. Because electro-negative gases are most often used in semiconductor processing, we apply this model to simulate both pulsed  $O_2$  and  $O_2 + Ar$  mixture discharges. Because of the numerical instability caused by fast transits at the beginning and at the end of the pulses, we chose Rosenbrock methods [99] to simulate pulsed Ar,  $O_2$ , and  $Ar + O_2$  plasma dynamics.

## 4.2 Spatially Averaged Simulation Model Setup

### 4.2.1 Assumptions

The simulated discharge is confined to a cylindrical chamber with  $L = 8$  cm and  $R = 7.5$  cm. Some necessary assumptions [56] for this model are listed below:

- All particle densities  $n$  are assumed to be volume-averaged using the equation:

$$n = \frac{1}{\pi R^2 L} 2\pi \int_0^R r dr \int_0^L n(r, z) dz. \quad (4.1)$$

- The positive-ion densities in an electro-positive discharge are assumed to have a uniform profile throughout the discharge except near the wall, where the densities are assumed to drop sharply to sheath-edge densities,  $n_{is}$ . For an electro-negative discharge, the electron density  $n_e$  is assumed to be uniform throughout the discharge

except near the sheath edge, while the negative-ion density  $n_-$  is assumed to be parabolic, dropping to zero at the sheath edge. The electron density is

$$n_e = n_i - n_-, \quad (4.2)$$

with  $n_i = n_e = n_{is}$ , at the sheath edge. Only one type of negative ion is considered.

- The energy loss processes for which one ion is dissociated to form another and collisions of electrons with positive or negative ions are neglected.
- The factors  $h_L$  and  $h_R$  are assumed to be independent of the type of ions, i.e., the ion-neutral mean-free path  $\lambda$  is identical for all species in the discharge.
- The electron energy distribution function is assumed to be Maxwellian.

$$f(v) = n \left( \frac{m}{2\pi kT_e} \right)^{\frac{3}{2}} \exp\left(-\frac{mv^2}{2kT_e}\right) \quad (4.3)$$

The rate constants  $k(T_e)$  are calculated based on the cross-section values taken from available literature:

$$k(T) = \left( \frac{m}{2\pi kT_e} \right)^{\frac{3}{2}} \int_0^\infty \sigma(v) v \exp\left(-\frac{mv^2}{2kT_e}\right) 4\pi v^2 dv \quad (4.4)$$

Other types of energy distribution functions could also be used to derive corresponding rate constants.

- The ion temperature  $T_i$  is assumed to be 0.5 eV for pressures less than 1 mTorr; for higher pressures,  $T_i - T_o$  is allowed to decrease at a rate proportional to  $1/p$ , where  $p$  is the pressure, ultimately reaching the thermal neutral temperature of  $T_o = 600$  K.

## 4.2.2 Steady-state model

Godyak and Maximov [15] have solved the diffusion equations analytically and determined approximate plasma densities at the sheath edges:

$$h_L = \frac{n_{sl}}{n_e} = 0.86(3 + \frac{L}{2\lambda})^{-\frac{1}{2}} \quad (4.5)$$

at the axial sheath edge, and

$$h_R = \frac{n_{sr}}{n_e} = 0.80(4 + \frac{r}{\lambda})^{-\frac{1}{2}} \quad (4.6)$$

at the radial sheath edge.

The effective diffusion length for excited state particles is calculated from: [15]

$$\frac{1}{\Lambda} = \frac{\pi}{L^2} + (\frac{2.405}{R})^2. \quad (4.7)$$

The excited states de-excite upon striking the chamber walls, and the ground state species return to the reactor. These diffusional losses are represented by  $D_{eff}/\Lambda^2$ , where  $D_{eff}$  is the effective diffusion coefficient of the neutral species of interest, which has the expression

$$D_{eff} = \frac{1}{\frac{1}{D_{AA\cdot}} + \frac{1}{D_{kn}}}, \quad (4.8)$$

where  $D_{AA\cdot}$  is the diffusion coefficient estimated using the Chapman-Enskog equation for gas diffusivity, and  $D_{kn}$  is the Knudsen free-diffusion coefficient equal to:

$$D_{kn} = \frac{1}{3}(\frac{kT_0}{M})^{\frac{1}{2}}\Lambda. \quad (4.9)$$

The Chapman-Enskog formulas for diffusivity for the gaseous state at low density is:

$$D_{AB} = 2.2646 \times 10^{-5} \frac{\sqrt{T(\frac{1}{M_A} + \frac{1}{M_B})}}{\sigma_{AB}^2 \Omega_{D,AB}} \quad (4.10)$$

This equation is recast to another form:

$$D_{AB} = 0.0018583 \frac{\sqrt{T^3(\frac{1}{M_A} + \frac{1}{M_B})}}{p\sigma_{AB}^2\Omega_{D,AB}}, \quad (4.11)$$

in which the units are  $D_{AB}$ ,  $cm^2sec^{-1}$ ;  $T$ ,  $^{\circ}K$ ;  $p$ , atm;  $\sigma_{AB}$ , angstrom units.  $\Omega_{D,AB}$  is a dimensionless tabular function of the temperature and of the intermolecular potential field for one molecule of A and one of B. For potentials of below Leonard-Jones form:

$$\varphi_{AB}(r) = 4\epsilon_{AB}[(\frac{\sigma_{AB}}{r})^{12} - (\frac{\sigma_{AB}}{r})^6] \quad (4.12)$$

$$\sigma_{AB} = \sigma_A + \sigma_B, \quad (4.13)$$

Tables of  $\Omega_{D,AB}$  exist, [100] thus we can compute an the effective diffusion coefficient.

For Ar gas, four main sets of equations are used in the global model for the mono-atomic gas to fulfill the power balance and particle balance for all species of interest. The general form of power balance is :

$$P_{abs} = P_{ev} + P_{iw} + P_{ew} \quad (4.14)$$

where  $P_{abs}$  is the power absorbed by the system,  $P_{ev}$  is the electron energy loss due to all electron-neutral collision processes in the volume,  $P_{iw}$  is the ion energy loss to the wall, and  $P_{ew}$  is the electron energy loss to the walls while A is the surface area.

$$P_{iw} = n_s u_b (eV_s + \frac{eT_e}{2}) A. \quad (4.15)$$

$$P_{ew} = 2eT_e n_s u_b A. \quad (4.16)$$

By equating the ion and electron flux at the sheath, The sheath potential drop is

$$V_s = \frac{T_e}{2} \ln\left(\frac{M}{2\pi m}\right). \quad (4.17)$$

$$P_{ev} = en_e V \varepsilon_L \nu_{iz} \quad (4.18)$$

Radiation is included in the particle balance equations. For atomic gases, the energy loss  $\varepsilon_L$  per electron-ion pair created due to all electron neutral collision processes is: [15]

$$\varepsilon_L = \varepsilon_{iz} + \sum_{k=1}^{N_{exc}} \frac{\nu_{exc,k}}{\nu_{iz}} \varepsilon_{exc,k} + \frac{\nu_{elas}}{\nu_{iz}} \frac{3T_e}{2} \frac{2m}{M} \quad (4.19)$$

where  $\nu = \langle \sigma \nu \rangle n_n$  is the appropriate collision frequency,  $\langle \sigma \nu \rangle$  is the rate coefficient,  $n_n$  is the neutral density, and  $N_{exc}$  is the number of excitation energy-loss channels. The first term on the right-hand side is the energy loss due to the direct ionization of neutral atoms with an ionization potential of  $\varepsilon_{iz}$  (in units of eV), the second term represents the total energy loss due to excitation of neutral atoms to various excite states with threshold energies  $\varepsilon_{exc}$ , and the last term is the energy loss due to electron-neutral elastic-scattering. Since the ratios of collision frequencies equal to the corresponding ratios of rate constants independent of the atomic gas density,  $\varepsilon_L$  is a function of  $T_e$  only.

Ions are lost to the wall at a characteristic velocity:

$$u_b = \left(\frac{eT_e}{M}\right)^{\frac{1}{2}} \quad (4.20)$$

where  $e$  is  $1.6 \times 10^{-19}c$ . For molecular gases, we assume:

- Generation of multiple positive ions and negative ions are possible.

- Additional energy-loss channels such as dissociation are included.
- Particle loss channels such as volume positive-negative ion recombination,

need to be included, so that Eqn. 4.19 can be re-cast as:

$$\nu_{iz}\varepsilon_{L,i} = \sum_{j=1}^{N_{s,j}} (\nu_{iz,ij}\varepsilon_{iz,ij} + \sum_{k=1}^{n_{exc,j}} \nu_{exc,kj}\varepsilon_{exc,kj} + \nu_{elas,j} \frac{2m}{M_j} \frac{3T_e}{2}), \quad (4.21)$$

where  $n_{s,i}$  is the number of neutral species that generate the  $i$ th ions. For  $Ar^+$ ,  $N_{s,i} = 2$  ( $Ar$  and  $Ar^*$ ); for  $O^+$ ,  $N_{s,i} = 2$  ( $O$  and  $O^*$ ); for  $O_2^+$ ,  $N_{s,i} = 1$  ( $O_2$ );  $\nu_{iz,ij}$  is the ionization frequency for production of the  $i$ th ions from neutral species  $j$ ,  $\nu_{iz,i}$  is the total ionization frequency for production of  $i$ th ion,  $\varepsilon_{iz,ij}$  is the threshold ionization energy for production of the  $i$ th ion from neutral species  $j$ ,  $\varepsilon_{exc,kj}$  the threshold excitation energy for the  $k$ th level of the  $j$ th neutral, and  $\varepsilon_{L,i}$  is the total collisional energy loss process per electron-ion pair created for the  $i$ th ion. The sum over  $k$  includes all inelastic electron-neutral collisional processes that do not produce positive ions, e.g., rotational, vibration and electronic excitation, dissociation, attachment, and detachment.

### Pure Argon Discharge

In this simple case, we follow the particle density of three species in Ar discharges,  $n_{4s}$ ,  $n_{4p}$ ,  $n_i$ , and  $T_e$ [43]. In this simulation,  $n_e$  is assumed to be equal to  $n_i$ .

The particle balance equations are:

$$\frac{dn_{4s}}{dt} = \sum_i k_{col} n_j n_k - k_{rad} n_{4s} - \frac{D_{eff}}{\Lambda^2} n_{4s} \quad (4.22)$$

$$\frac{dn_{4p}}{dt} = \sum_i k_{col} n_j n_k - k_{rad} n_{4p} - \frac{D_{eff}}{\Lambda^2} n_{4p} \quad (4.23)$$

$$V \frac{dn_i}{dt} = \sum_i V k_{iz,i} n_0 n_i - (h_L A_L + h_R A_R) n_i u_b \quad (4.24)$$

where  $k_{rad}$  is the radiative constant,  $k_{col}$  represents the collisional rate constant between  $n_j, n_k$ . The corresponding power balance is expressed as

$$P_{abs}(t) = V \left[ \frac{d}{dt} \left( \frac{3}{2} e n_i T_e \right) + e n_0 n_g \sum k_i \varepsilon_i \right] + (n_{sl} A_L + n_{sr} A_R) u_b (e V_s + \frac{5}{2} e T_e) \quad (4.25)$$

Reaction rates in Table 4.1 [43] are used to solve these ODE equations.

$Ar + e \rightarrow Ar(4s) + e$	$k_1 = 5.0 \times 10^{-15} T_e^{0.74} \exp(-11.57/T_e) m^3 s^{-1}$
$Ar(4s) + e \rightarrow Ar + e$	$k_2 = 4.3 \times 10^{-16} T_e^{0.74} m^3 s^{-1}$
$Ar + e \rightarrow Ar(4p) + e$	$k_3 = 1.4 \times 10^{-14} T_e^{0.71} \exp(-13.2/T_e) m^3 s^{-1}$
$Ar(4p) + e \rightarrow Ar + e$	$k_4 = 3.9 \times 10^{-16} T_e^{0.71} m^3 s^{-1}$
$Ar(4s) + e \rightarrow Ar(4p) + e$	$k_5 = 8.9 \times 10^{-13} T_e^{0.51} \exp(-1.59/T_e) m^3 s^{-1}$
$Ar(4p) + e \rightarrow Ar(4s) + e$	$k_6 = 3.0 \times 10^{-13} T_e^{0.51} m^3 s^{-1}$
$Ar + e \rightarrow Ar^+ + 2e$	$k_7 = 2.3 \times 10^{-14} T_e^{0.68} \exp(-15.76/T_e) m^3 s^{-1}$
$Ar(4s) + e \rightarrow Ar^+ + 2e$	$k_8 = 6.8 \times 10^{-15} T_e^{0.67} \exp(-4.20/T_e) m^3 s^{-1}$
$Ar(4p) + e \rightarrow Ar^+ + 2e$	$k_9 = 1.8 \times 10^{-13} T_e^{0.61} \exp(-2.61/T_e) m^3 s^{-1}$
$Ar_m(4s) + e \rightarrow Ar_r(4s) + e$	$k_{10} = 2.0 \times 10^{-13} m^3 s^{-1}$
$Ar_r(4s) + e \rightarrow Ar + h\nu$	$A_{s,eff} = 3.0 \times 10^7$
$Ar(4p) \rightarrow Ar + h\nu$	$A_{p,eff} = 3.0 \times 10^7$
$Ar(4p) \rightarrow Ar(wall)$	$D_{eff}/\Lambda^2$
$Ar(4s) \rightarrow Ar(wall)$	$D_{eff}/\Lambda^2$
$Ar^+ \rightarrow Ar(wall)$	$2.ub_{Ar^+}(R^2 h_L + R L h_R)/R^2 L$

Table 4.1: Reactions for Ar discharges included in the global model[43]

## Pure Oxygen Discharge

Table 4.2 [56] lists the dominant known reactions for a low temperature oxygen discharge. The equations below are used to solve the singly ionized atomic



oxygen ion density,  $n_{O_i}$ , molecular oxygen ion density,  $n_{O_2i}$ , negative ion density,  $n_{O^-}$ , molecular oxygen,  $n_{O_2}$ , ground state atomic oxygen (O3P) density,  $n_O$ , excited state atomic oxygen (O1D) density,  $n_O^*$ , and electron temperature,  $T_e$ . The electron density is derived from charge neutrality (Eqn. 4.26).

$$n_e = n_{O_i} + n_{O_2i} - n_{O^-} \quad (4.26)$$

$$\frac{dn_{O_i}}{dt} = k(4)n_en_o + k(13)n_en_o^* - k(14)n_{O_i} - k_r n_{O_i} - k(6)n_{O^-}n_{O_i} \quad (4.27)$$

$$\frac{dn_{O_2i}}{dt} = k(1)n_en_{O_2} - k(15)n_{O_2i} - k(5)n_{O^-}n_{O_2i} - k_r n_{O_2i}, \quad (4.28)$$

where  $k_r$  is the rate for removal of species from the vacuum chamber by the vacuum pump.. There will be no pumping loss of negative ions because the plasma sheath will confine the negative ions into the center of the discharge during the cw power operation. The main loss channel for negative ions is volume recombination with positive ions. The plasma sheath collapses after the rf power is off, so during the plasma-off period, an additional pumping loss channel for negative ions is added into the simulation model. The corresponding particle balance equations are :

$$\frac{dn_{O^-}}{dt} = k(3)n_en_{O_2} - k(5)n_{O_2i}n_{O^-} - k(7)n_en_{O^-} - k(6)n_{O_i}n_{O^-} \quad (4.29)$$

when the rf power is on.

Reaction	rate coefficient
$e + O_2 \rightarrow O_2^+ + 2e$	$k_1 = 9.0 \times 10^{-10} T e^2 \exp(-12.76/Te) \text{cm}^3 \text{s}^{-1}$
$e + O_2 \rightarrow O(^3P) + O(^1D) + e$	$k_2 = 5.0 \times 10^{-8} \exp(-8.4/Te) \text{cm}^3 \text{s}^{-1}$
$e + O_2 \rightarrow O(^3P) + O$	$k_3 = 4.6 \times 10^{-11} \exp(2.91/Te - 1.26/Te^2 + 6.92/Te^3) \text{cm}^3 \text{s}^{-1}$
$e + O(^3P) \rightarrow O^+ + 2e$	$k_4 = 9.0 \times 10^{-9} T e^{0.7} \exp(-13.6/Te) \text{cm}^3 \text{s}^{-1}$
$O^- + O_2^+ \rightarrow O(^3P) + O_2$	$k_5 = 1.4 \times 10^{-7} \text{cm}^3 \text{s}^{-1}$
$O^- + O^+ \rightarrow O(^3P) + O(^3P)$	$k_6 = 2.7 \times 10^{-7} \text{cm}^3 \text{s}^{-1}$
$e + O^- \rightarrow O(^3P) + 2e$	$k_7 = 1.73 \times 10^{-7} \exp(-5.67/Te + 7.3/Te^2 - 3.48/Te^3) \text{cm}^3 \text{s}^{-1}$
$e + O_2 \rightarrow O(^4P) + O(^3P) + e$	$k_8 = 4.23 \times 10^{-9} \exp(-5.56/Te) \text{cm}^3 \text{s}^{-1}$
$e + O(^3P) \rightarrow O(^1D) + e$	$k_9 = 4.47 \times 10^{-9} \exp(-2.286/Te) \text{cm}^3 \text{s}^{-1}$
$O(^1D) + O_2 \rightarrow O(^3P) + O_2$	$k_{10} = 4.1 \times 10^{-11} \text{cm}^3 \text{s}^{-1}$
$O(^1D) + O(^3P) \rightarrow O(^3P) + O(^3P)$	$k_{11} = 8.1 \times 10^{-12} \text{cm}^3 \text{s}^{-1}$
$O(^1D) \rightarrow^{wall} O(^3P)$	$k_{12} = D_{eff}/\Lambda^2 \text{s}^{-1}$
$e + O(^1D) \rightarrow O^+ + 2e$	$k_{13} = 9.0 \times 10^{-9} T e^{0.7} \exp(-11.67/Te) \text{cm}^3 \text{s}^{-1}$
$O^+(g) \rightarrow^{wall} O(^3P)(g)$	$k_{14} = 2u_{b,O^+} (R^2 h_L + R L h_R) / R^2 L \text{s}^{-1}$
$O_2^+(g) \rightarrow^{wall} O_2(g)$	$k_{15} = 2u_{b,O_2^+} (R^2 h_L + R L h_R) / R^2 L \text{s}^{-1}$
$O(g) \rightarrow^{wall} \frac{1}{2} O_2(g)$	$k_{16} = \gamma_{rec} / \Lambda^2 \text{s}^{-1}$
$e + Ar \rightarrow Ar^+ + 2e$	$k_{17} = 1.23 \times 10^{-13} \exp(-18.68/Te) \text{cm}^3 \text{s}^{-1}$
$e + Ar \rightarrow Ar^* + e$	$k_{18} = 3.71 \times 10^{-14} \exp(-15.05/Te) \text{cm}^3 \text{s}^{-1}$
$e + Ar^* \rightarrow Ar^+ + 2e$	$k_{19} = 2.05 \times 10^{-13} \exp(-4.95/Te) \text{cm}^3 \text{s}^{-1}$
$e + Ar^* \rightarrow Ar + 2e$	$k_{20} = 2. \times 10^{-13} \text{cm}^3 \text{s}^{-1}$
$Ar^* + Ar^* \rightarrow Ar + Ar^+$	$k_{21} = 6.2 \times 10^{-16} \text{cm}^3 \text{s}^{-1}$
$Ar^+ \rightarrow Ar$	$k_{22} = 2.u_{b,Ar^+} * (R^2 h_L + R L h_R) / R^2 L$
$Ar^* \rightarrow Ar$	$k_{23} = D_{eff} / \Lambda^2$
$O^- + Ar^+ \rightarrow Ar + O$	$k_{24} = 2.70 \times 10^{-7} \text{cm}^3 \text{s}^{-1}$
$O_2 + Ar^* \rightarrow Ar + O_2$	$k_{25} = 1.12 \times 10^{-9} \text{cm}^3 \text{s}^{-1}$
$O + Ar^* \rightarrow Ar + O$	$k_{26} = 8.10 \times 10^{-12} \text{cm}^3 \text{s}^{-1}$
$O_2 + Ar^* \rightarrow Ar + O + O$	$k_{27} = 5.80 \times 10^{-11} \text{cm}^3 \text{s}^{-1}$
$O_2 + Ar^+ \rightarrow O_2^+ + Ar$	$k_{28} = 1.20 \times 10^{-11} \text{cm}^3 \text{s}^{-1}$
$O + Ar^+ \rightarrow O^+ + Ar$	$k_{29} = 1.20 \times 10^{-11} \text{cm}^3 \text{s}^{-1}$

Table 4.2: Reaction rate sets for Argon-Oxygen plasmas

$$\begin{aligned} \frac{dn_{O_2}}{dt} = & \text{source} + k(15)n_{O_2i} + k(5)n_{O^-}n_{O_2i} - (k(1) + k(2) + k(3) + k(8))n_en_{O_2} \\ & - krn_{O_2} + k(16)n_O/2, \end{aligned} \quad (4.30)$$

where 'source' is derived from measurement of the flow rate.

$$\begin{aligned} \frac{dn_O}{dt} = & (k(2) + k(3) + 2k(8))n_en_{O_2} + k(5)n_{O_2i}n_{O^-} + 2k(6)n_{O_i}n_{O^-} + k(7)n_en_{O^-} \\ & + k(12)n_O^* - krn_O + k(10)n_{O_2}n_O^* + k(11)n_On_O^* - k(9)n_en_O - k(4)n_en_O \\ & + k(14)n_{oi} - k(16)n_O \end{aligned} \quad (4.31)$$

$$\begin{aligned} \frac{dn_O^*}{dt} = & k(2)n_en_{O_2} + k(9)n_en_O - k(10)n_{O_2}n_O^* - k(11)n_On_O^* - k(13)n_en_O^* \\ & - k(12)n_O^* - krn_O^* \end{aligned} \quad (4.32)$$

The power balance equation is :

$$\begin{aligned} \frac{dn_e T_e}{dt} = & (P_{abs} - eV[12.6(n_en_{O_2}(k(1) + k(2)3.4n_en_{O_2} + k(4)13.6n_On_e \\ & + n_en_{O_2}k(8)5.56 + n_en_Ok(9)2.286)] - n_{oi}e6.T_eub_{oi} * A_{eff} \\ & - n_{O_2i}e6T_eub_{O_2i}A_{eff})/(3/2Ve) \end{aligned} \quad (4.33)$$

### Ar + O<sub>2</sub> Mixture

For Ar + O<sub>2</sub> plasma discharge, the discharge chemistry is more complicated. We must add reactions between Ar and oxygen (listed in Table 4.2) to the simulation

model.

The corresponding particle and energy balance equations are:

$$\frac{dn_{oi}}{dt} = k(4)n_en_o + k(13)n_en_o^* - k(14)n_{oi} - k_r n_{oi} - k(6)n_{O^-}n_{oi} + k(29)n_on_{Ari} \quad (4.34)$$

$$\frac{dn_{O2i}}{dt} = k(1)n_en_{O2} - k(15)n_{O2i} - k(5)n_{O^-}n_{O2i} - k_r n_{O2i} + k(28)n_{O2}n_{Ari} \quad (4.35)$$

With the rf power on:

$$\frac{dn_{O^-}}{dt} = k(3)n_en_{O2} - k(5)n_{O2i}n_{O^-} - k(7)n_en_{O^-} - k(6)n_{O_i}n_{O^-} + k(24)n_{O^-}n_{Ari}. \quad (4.36)$$

With the rf power off:

$$\frac{dn_{O^-}}{dt} = k(3)n_en_{O2} - k(5)n_{O2i}n_{O^-} - k(7)n_en_{O^-} - k(6)n_{O_i}n_{O^-} + k(24)n_{O^-}n_{Ari} - k_r n_{O^-}. \quad (4.37)$$

$$\begin{aligned} \frac{dn_{O2}}{dt} = & source + k(15)n_{O2i} + k(5)n_{O^-}n_{O2i} - (k(1) + k(2) + k(3) + k(8))n_en_{O2} \\ & - k_r n_{O2} + k(16)n_{O}/2 + k(27)n_{O2}n_{Ard} + k(28)n_{O2}n_{Ari} \end{aligned} \quad (4.38)$$

$$\begin{aligned} \frac{dn_O}{dt} = & (k(2) + k(3) + 2k(8))n_en_{O2} + k(5)n_{O2i}n_{O^-} + 2k(6)n_{O_i}n_{O^-} + k(7)n_en_{O^-} \\ & + k(12)n_o^* - k_r n_O + k(10)n_{O2}n_o^* + k(11)n_on_o^* - k(9)n_en_o - k(4)n_en_o \\ & + k(14)n_{oi} - k(16)n_O + 2k(27)n_{O2}n_{Ard} \end{aligned} \quad (4.39)$$

$$\frac{dn_O^*}{dt} = k(2)n_en_{O2} + k(9)n_en_o - k(10)n_{O2}n_o^* - k(11)n_on_o^* - k(13)n_en_o^* - k(12)n_o^* - k_r n_O^* \quad (4.40)$$

$$\begin{aligned}
\frac{dn_{Ar}}{dt} = & k(17)n_e n_{Ari} - k(18)n_e n_{Ari} + k(20)n_e n_{Ard} + k(21)n_{Ard} n_{Ard} + k(22)n_{Ari} \\
& + k(23)n_{Ard} + k(24)n_o^- n_{Ari} + k(25)n_{Ard} n_{O2} + k(26)n_o n_{Ard} + \\
& + k(27)n_{O2} n_{Ard} + k(28)n_{O2} n_{Ari} - k_r n_{Ar} + k(29)n_o n_{Ari}
\end{aligned} \tag{4.41}$$

$$\begin{aligned}
\frac{dn_{Ard}}{dt} = & k(18)n_e n_{Ar} - k(19)n_e n_{Ard} - k(20)n_e n_{Ard} - k(21)n_{Ard} n_{Ard} - k(23)n_{Ard} \\
& - k(25)n_{O2} n_{Ard} - (k(26)n_o n_{Ard} - k_r n_{Ard} + k(27)n_{O2} n_{Ard}
\end{aligned} \tag{4.42}$$

$$\begin{aligned}
\frac{dn_{Ari}}{dt} = & k(17)n_e n_{Ar} + k(19)n_e n_{Ard} + k(21)n_{Ard} * n_{Ard} - k(22)n_{Ari} - k(24)n_o^- n_{Ari} \\
& - k(28)n_{O2} n_{Ari} - k_r n_{Ari} + k(29)n_o n_{Ari}
\end{aligned} \tag{4.43}$$

$$\begin{aligned}
\frac{dn_e T_e}{dt} = & (P_{abs} - eV \epsilon_{L1} k(4)n_e n_o - k(1)e \epsilon_{L2} n_e n_{O2} V - k(17)eV \epsilon_{L3} n_e n_{Ar} \\
& - n_{oi} e 6. T_e u b_{oi} * A_{eff} - n_{O2i} e 6 T_e u b_{O2i} A_{eff} - n_{Ari} e T_e u b_{Ari} A_{eff}) / (3/2 V e)
\end{aligned} \tag{4.44}$$

### 4.2.3 Pulsed Operation

In pulsed plasma simulation, different forms of the rf power input can be used to observe the particle density and electron temperature transients with modulated rf power. The simplest rf power input is a square envelope.

$$P_{abs} = P_{on}, \quad T < \alpha\tau,$$

$$P_{off} = 0 \quad \text{or} \quad P_{off} \neq 0 \quad T > \alpha\tau,$$

where  $\alpha$  is the pulse duty cycle and  $\tau$  is the pulse period. Because the initial electron temperature jump at the onset of the power pulse can induce severe damage, a continuously changing rf power may also be used to reduce the initial electron temperature jump.

## 4.3 Results and Discussion

### 4.3.1 CW plasma

There have been several previous studies for Ar and for  $O_2$  cw discharges, so we use the previous studies to benchmark the plasma chemistry computed by our models for Ar +  $O_2$  mixture in cw discharges. Fig. 4.1 shows the positive ion density

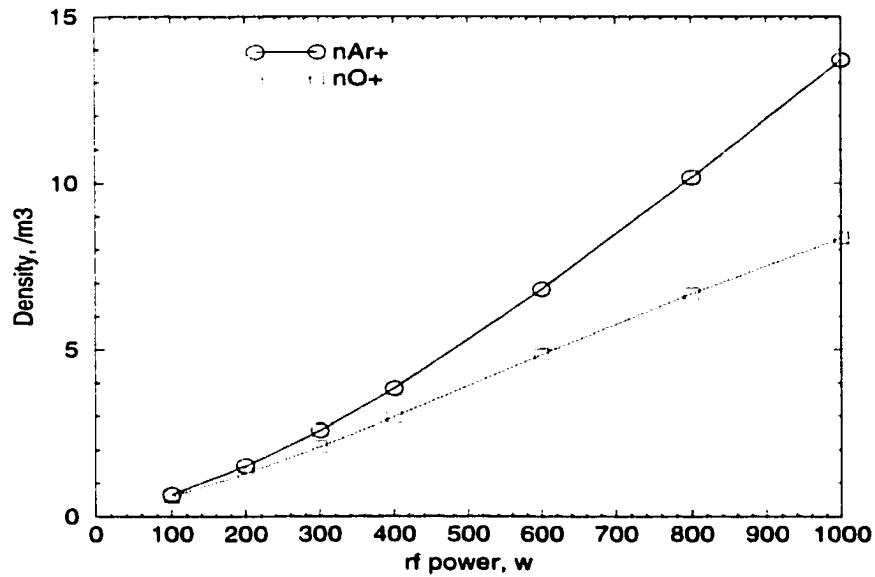


Figure 4.1: Calculated positive ion density,  $\times 10^{16} m^{-3}$  as a function of cw rf power for Ar +  $O_2$  discharge, Ar/ $O_2$ =1:10, 8mTorr

as a function of rf power. The positive ion densities for both Ar and atomic O increase with the rf power. However the Ar density increases much faster than the atomic oxygen density because more energy is need to generate oxygen atoms from oxygen molecules for the subsequent ionization, that is, 5.2 eV energy is required to



break the molecular bond between the two O atoms. Fig. 4.2 shows the molecular oxygen positive ion density and corresponding negative ion density variation as a function of rf power. The negative ion density decreases as the rf power increases, as does the  $O_2^+$  density because high rf power contributes to high dissociation rate of molecular oxygen. The electron attachment cross section  $\langle \sigma V_e \rangle$  is a function of electron temperature. It will decrease as the electron temperature rises. Because the electron temperature of the plasma does not change with rf power and because the negative ions are only generated through one channel(Eqn. 4.48), the decrease of parent molecules  $O_2$  to form negative ion with increased rf power results in the decreasing negative ion density.



Fig. 4.3, 4.4 show positive and negative ion densities respectively, as a function of discharge pressure. Fig. 4.5 shows the electron temperature as a function of the discharge pressure. Fig. 4.3 shows that Ar ion density increases with the discharge pressure. However, the O ion density has a maximum within this range of discharge

pressure. It is the function dependences of  $\varepsilon_L$  and  $A_{eff}$  with the discharge pressure that cause the above difference. It has been reported [56] that  $\varepsilon_L$  for oxygen is much larger than the  $\varepsilon_L$  of Ar because oxygen has more energy loss channels than does atomic Ar gas.  $\varepsilon_L$  generally increases with the discharge pressure. The effective loss area  $A_{eff}$ , on the other hand, decreases as the pressure increases because ions will be more confined by elastic collisions at higher pressures. Since these two factors varying in opposite directions, different behaviors for Ar and  $O_2$  plasmas are observed.

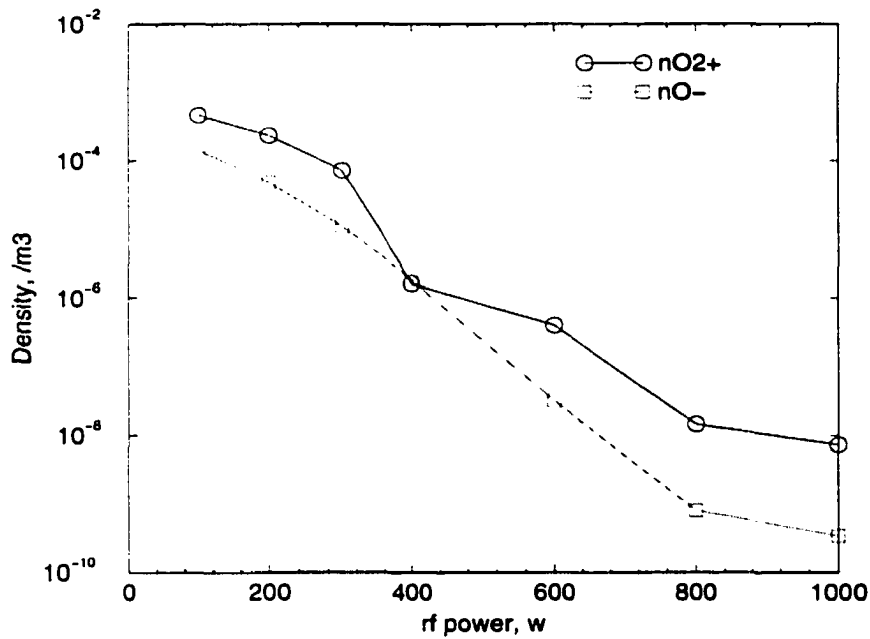


Figure 4.2: Negative ion density,  $\times 10^{16} m^{-3}$  as a function of cw rf power for Ar +  $O_2$  discharge

The electron temperature decreases as the pressure increases (Fig.4.5) because of increasing collisions at higher pressure. The low electron temperature and higher



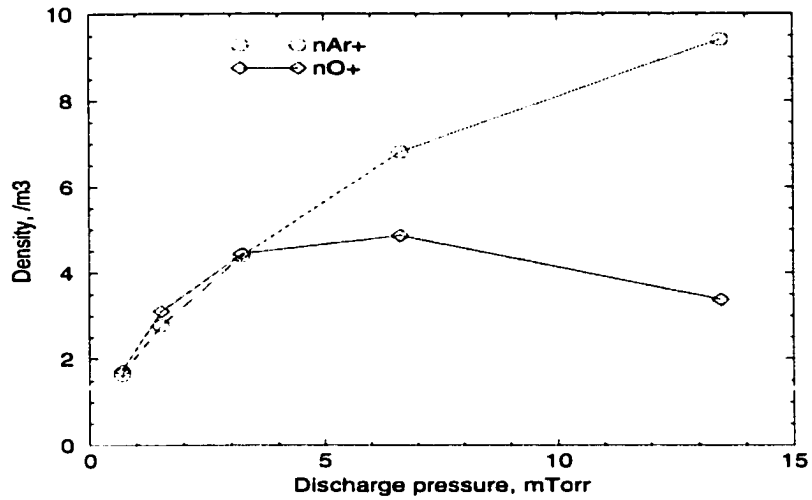


Figure 4.3: Calculated positive ion density,  $\times 10^{16} m^{-3}$  as a function of discharge pressure for Ar +  $O_2$  discharge, 400 W

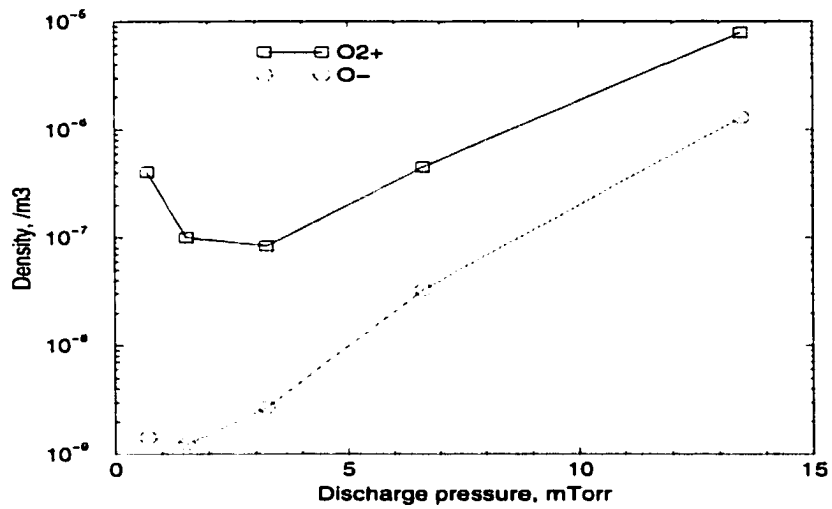


Figure 4.4: Calculated negative ion density,  $\times 10^{16} m^{-3}$  as a function of discharge pressure for Ar +  $O_2$  discharge, 400w

neutral particle density in the discharge contribute to a resulting increase of negative ion density. The above results, in good accord with previously published models and experiments for CW plasmas, give us a high degree of confidence in the correctness of our model. We then may use the model to examine the less well known territory of pulsed discharges.

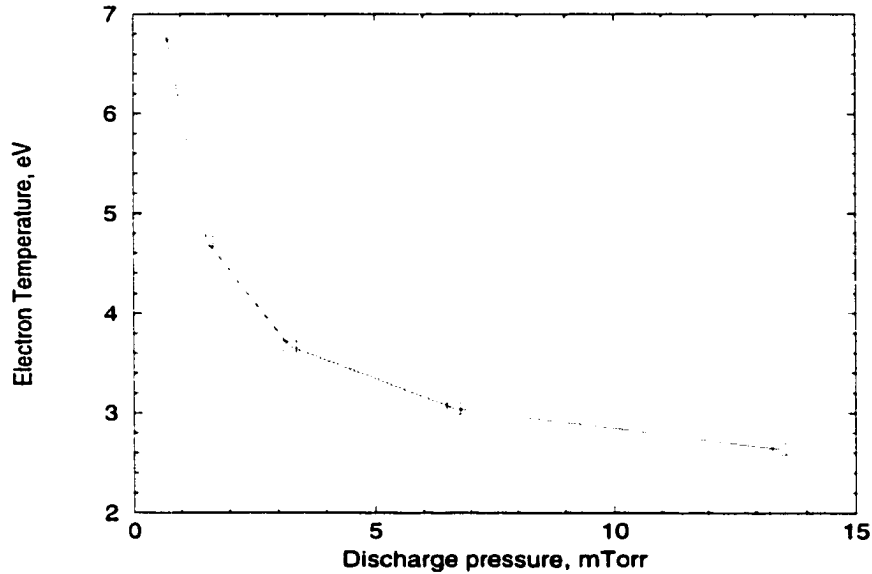


Figure 4.5: Calculated electron temperature as a function of discharge pressure for Ar +  $O_2$  discharge

### 4.3.2 Pulse-Modulated plasma

Fig. 4.6 and Fig. 4.7 show the electron temperature and particle species density transitions as a function of time for Ar discharges. The  $P_{off}$  equals zero unless otherwise stated. There is an electron temperature jump at the beginning of the rf pulse. This initial jump is attributed to the fact that there are few available

electrons to absorb and collisionally distribute the power at the start of the power pulse. This initial electron temperature jump is also observed in experiments. Because of experimental difficulties, double probes are not able to capture the transient time for this jump. However the simulation indicates this jump is on a scale of tens nanoseconds. The peak amplitude is less than 10 eV; however, such a jump can cause severe damage to a device. As the pulse frequency increases, the amplitude of this initial electron temperature jump gets smaller. At higher pulse frequencies, there is no observed electron temperature jump at the onset of the rf power pulse because a large number of ions remain present during the short pulse-off period. Another way to eliminate this problem is to apply a continuously changing rf power during the pulse-on period. Simulations for such “continuous” powers show a smooth electron

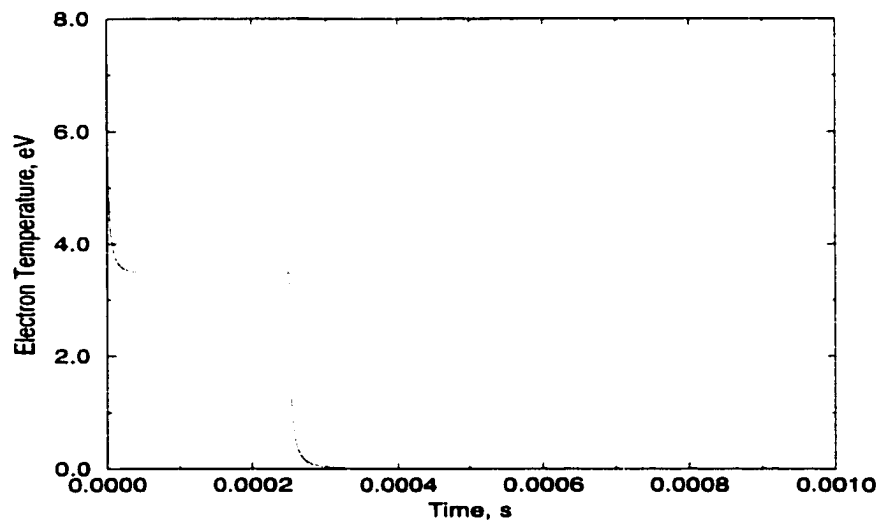


Figure 4.6: Calculated electron temperature transition for pulsed Ar discharges at 1kHz

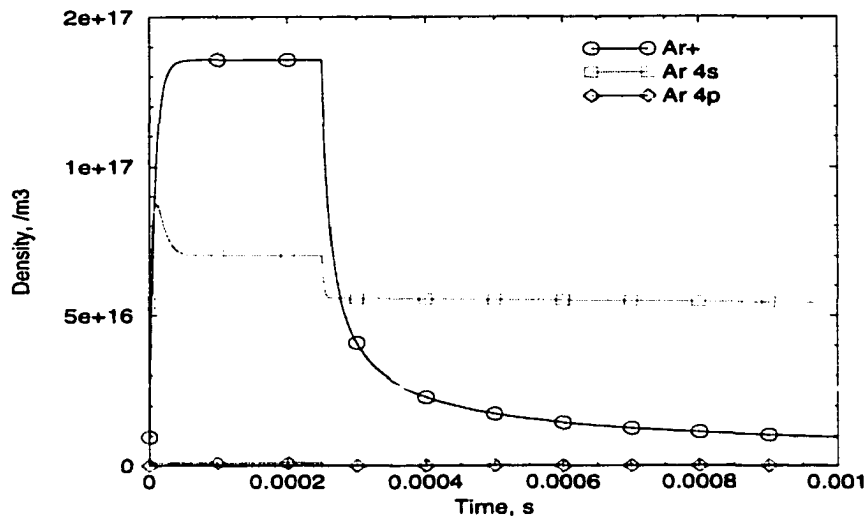


Figure 4.7: Calculated particle density transition for pulsed Ar discharges at 1kHz

temperature variation. The plasma density and other particle densities decay much slower than electron temperature does. The difference in particle generation and loss rates makes it possible to achieve a high average plasma density by changing the pulse frequencies, duty cycles, and pulse shape with the same time average rf power. As Ashida pointed out, [57] the particle generation rate has the similar transient behavior as the electron temperature because the ionization rate is a strong function of electron temperature. Our model shows that the time-average plasma density is higher than the cw plasma density with the same time average power at most frequencies. Pulsed oxygen discharges show the similar transient behavior for both electron temperature and positive ion densities with Ar discharges. Fig. 4.8 summarizes the time-average electron temperature as a function of the duty cycles in oxygen discharges. The time-average electron temperature increases as the duty cycle increases. It is possible to achieve a low time average electron temperature by reducing the duty cycle. However,

as the duty cycle decreases, the initial electron temperature jump gets much higher. This short transient behavior of electron temperature can cause severe damage to the features.

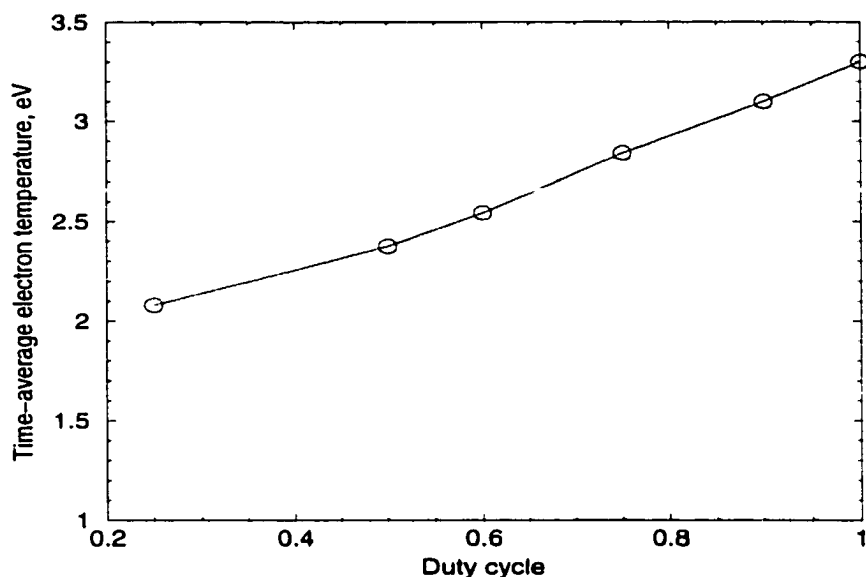


Figure 4.8: Time-average electron temperature as a function of duty cycles

Fig. 4.9 shows that the time-average positive ion density increases as the duty cycle decreases. However the atomic oxygen density is almost unaffected by the duty cycle changes. The time-average plasma density as a function of pulse frequency is shown in the Fig. 4.10. The model predicts that the time-average plasma density will have a maximum near 1kHz. Thus it is possible to pulse the plasma at that frequency to achieve the highest time-average plasma density. For different discharge geometry, this optimum pulse frequency value may change. This model then should provide guidance in finding optimal conditions for scaling this source to a genuine application. The negative ion density increases initially when the rf power is turned

off and then starts to decrease. The negative ions may help to reduce the damage.

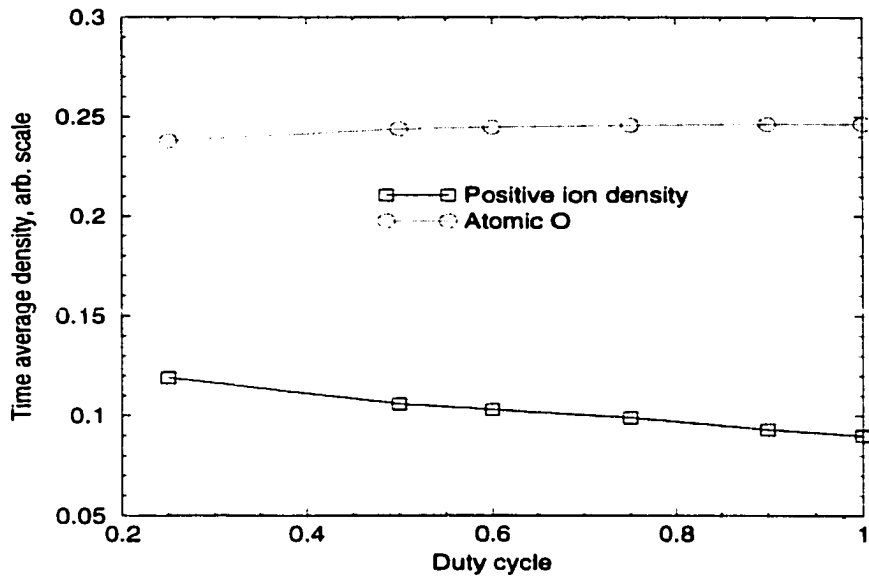


Figure 4.9: Time-average positive ion density as a function of duty cycles

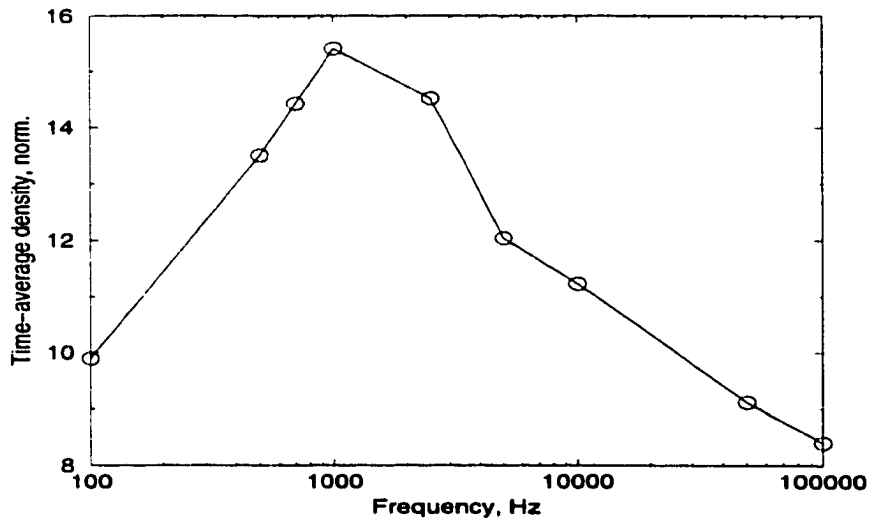


Figure 4.10: Time-average positive ion density as a function of pulse frequencies

Results for repetitive pulsing of Ar and oxygen mixture discharge results are shown

in Fig. 4.11 and Fig. 4.12. Fig. 4.11 shows positive ion density transient as a function

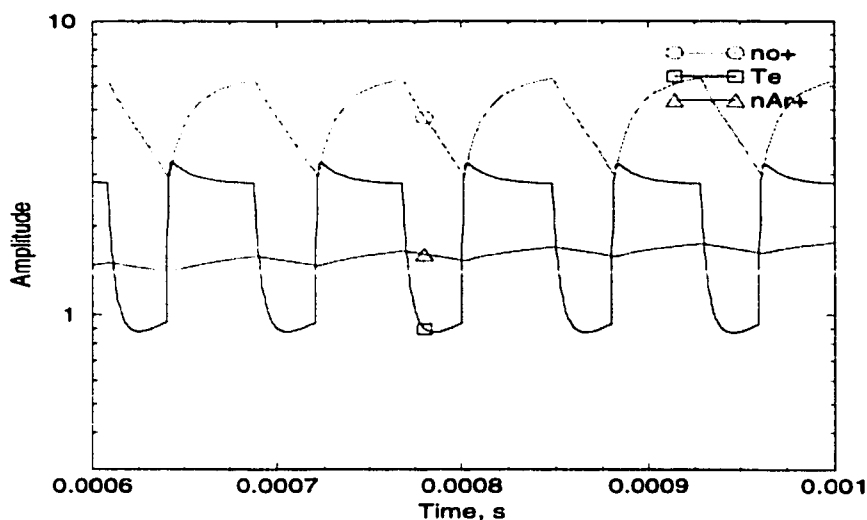


Figure 4.11: Positive ion density as a function of pulse frequencies for Ar +  $O_2$  mixture discharges, 800W, 7.8mTorr

of time while other species densities are shown in Fig. 4.12. The addition of Ar into the  $O_2$  discharge increase the total positive ion density because the ionization efficiency for Ar is comparatively higher than that of  $O_2$ . The negative ions show the same transient behaviour as in pure oxygen discharge. The pulse-off rf power is also set to nonzero values in the simulations. Fig. 4.13 shows simulated electron temperature transient as a function of time for a pulsed discharge with a fixed pulse-on rf power 600W. The electron temperature result with the lowest pulse-off power (60 W) has the highest electron temperature jump. In 60W and 300W pulse-off power cases, the electron temperatures drop quickly after the rf power is lowered and then climb back. With a large pulse-off rf power, the electron temperature recovers much faster. However, if we increase the pulse-off time for the 60 W case, the electron temperature

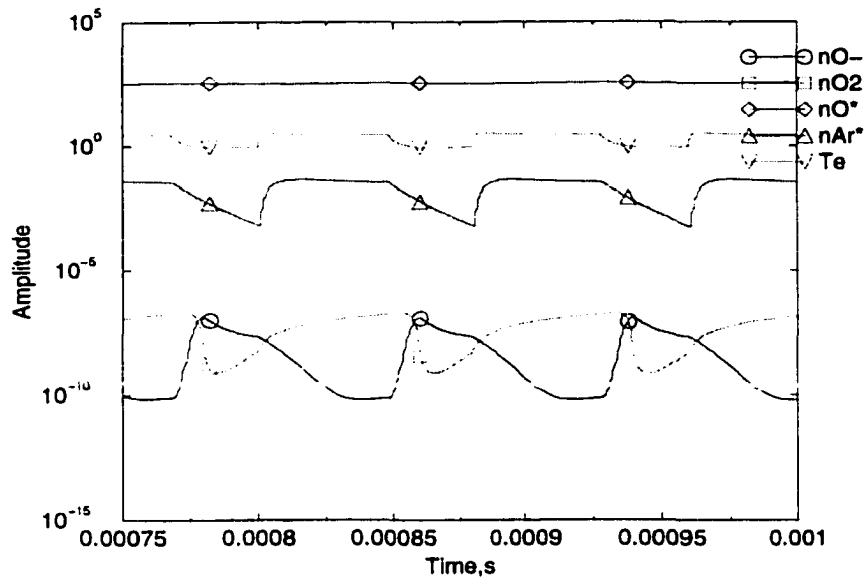


Figure 4.12: Particle species density as a function of pulse frequencies in Ar+ O<sub>2</sub> mixture discharges, 800 W, 7.8 mTorr

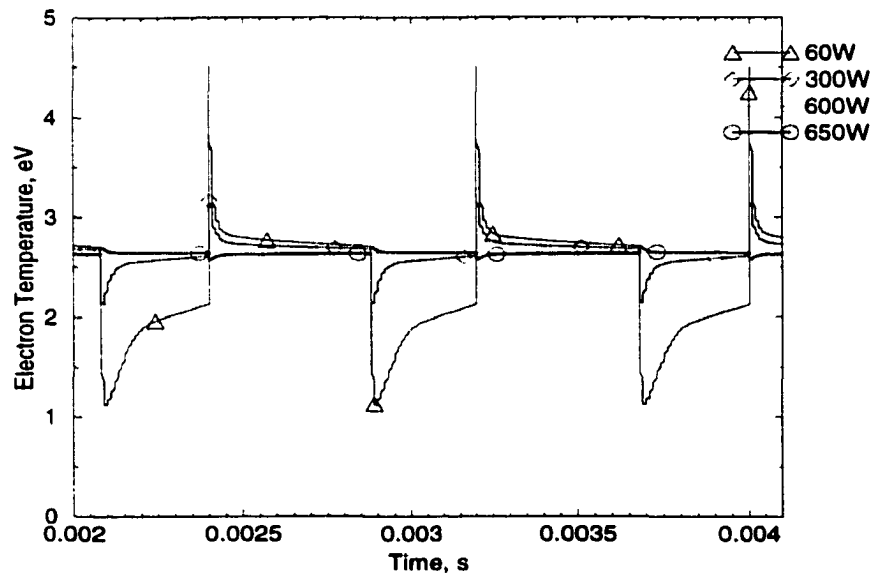


Figure 4.13: Electron temperature transient in pulsed Ar+ O<sub>2</sub> mixture discharges with nonzero rf power input during the pulse-off period, pulse-on power is fixed at 600W.



will eventually reach the steady-state value. Under these circumstances, we get the same electron temperature values for all pulse-off periods no matter what rf power (nonzero) is applied here. This agrees with our previous experimental results that the electron temperature is only a function of plasma discharge geometry at constant pressure. It is possible to lower the rf power further to a low limit so that the electron temperature will no longer rise.

## 4.4 Summary

We have performed a global average simulation model for both CW and pulsed plasmas. Studies indicate the time average electron temperature increases with duty cycle and pulse frequency. Simulations show a good agreement with experiments and previous work of others. It also has the predictive capability for arbitrary choices of cylindrical geometries. The positive ion density peak at certain pulse frequency and it decreases as the duty cycle increases. The atomic oxygen density increases with the duty cycle mainly caused by higher time average electron temperature. The negative ions reach the peak after the pulse is off. Results indicate that by pulsing the plasma, it is possible to achieve a high average plasma density and low electron temperature. The negative ions formed during the after-glow can be driven to neutralize the positive charge accumulation during the pulse on period.

# Chapter 5

## Stripping and cleaning of photo-resists using low energy neutrals

### 5.1 Introduction

The removal of residues after etching is a persistent problem in the semiconductor industry. Wet removal techniques [101], relying mostly on toxic acids, solvents, and dipping tanks have been, and continue to be used. Plasma ashing and cleaning can eliminate the handling and disposal of the toxic wastes, reduce the required footprint in the cleanroom, and provide abundant energetic and chemically activated species [102] that permit fast removal rates. Despite these advantages, plasma ashing processes, even remote or downstream, can induce severe damage to small features through several mechanisms [3,4]. The trend in semiconductor design towards thinner

gate oxides and smaller critical dimensions has made damage an increasingly important and critical issue. Among the potential mechanisms of damage is the presence of charged particle fluxes on sensitive structures. The search for selective, damage-free etching and stripping processes has prompted the consideration of neutral beams of atoms or molecules. Neutral stream processing is listed as one of the unsolved major items in the semiconductor industry association roadmap [103]. In order to examine the proof of concept for such processing, a few small-area neutral sources have been investigated. Giapis and Morre [104] developed a laser-driven neutral source for Si etching applications. Possible Si etching mechanisms by the hyper-thermal fluorine atomic beam were also discussed by Giapis *et al.*. Others studied small-area grid-neutralized ion sources [105]. However, these grid-neutralized sources have severe integrity and contamination problems during the operation. The low neutralization efficiency also limited their use. Our own group has studied small area surface reflection neutralization sources of high-density plasmas [10, 106]. Attempts to scale up such sources for large-area applications have been recently reported [12, 13]. In our previous work [13] on this broad-area source, Nichols and Manos presented a thorough description of the physics of this source, including a comprehensive numerical simulation of the performance issues. Simulations [13] predicted a trade off between the need for a high density plasma to create a higher neutral flux and increasing attenuation of the reflected neutral flux due to collisions in the plasma stream. In this chapter, experimental studies on cleaning applications for this broad-area inductively coupled plasma (ICP)-driven neutral source are reported and compared to the earlier simulation.

## 5.2 Experiment

### 5.2.1 Equipment setup

A schematic drawing of our apparatus is shown in Fig 5.1. The main chamber is an 8" six-way cross pumped by a 450 l/s Fomblin-prepared, turbomolecular pump. A variable-conductance valve between the chamber and the turbomolecular pump adjusts the discharge pressure. A gas mixing manifold with mass flow controllers introduces gases into the chamber. For pulsed-pressure operations, a Veeco-10 pulse valve is used. Convecatron, ionization gauges, and capacitance manometers are used to

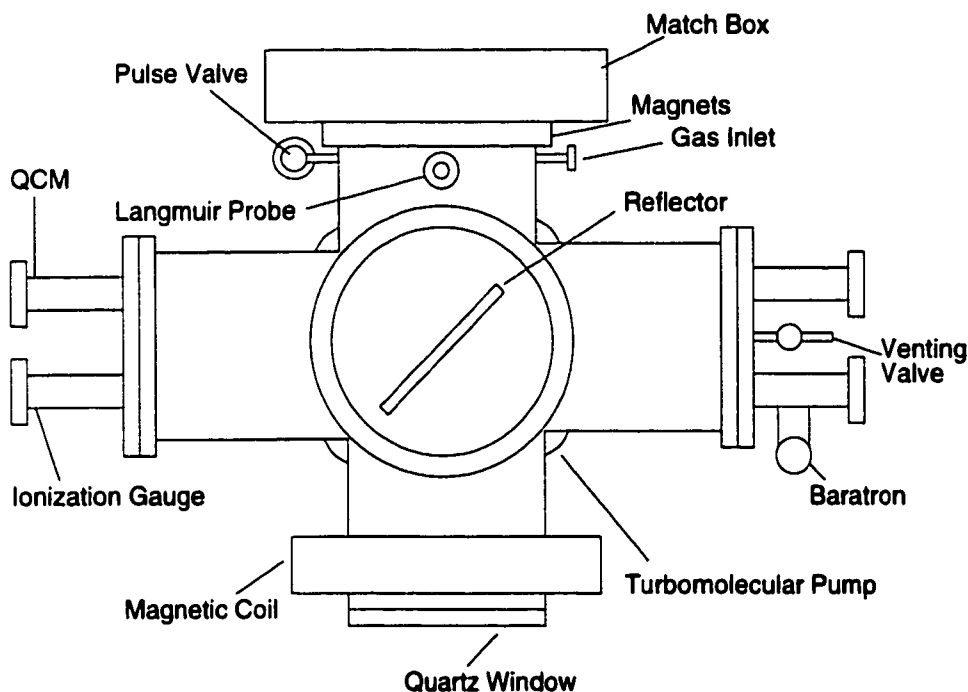


Figure 5.1: Schematic drawing of the low energy neutral beam

measure the chamber pressure (Fig. 5.1). In pulsed power applications, the variable

power supply is replaced by a wide-band, 600W linear amplifier driven by a programmable function generator. Frequency-tuned pulse trains of adjustable length can be used to provide variable duty-cycle power input to the modulated pressure pulses in the ICP zone. An angled reflector plate is located between the source region and the process region. A STM-100 quartz crystal microbalance is used in the downstream to measure the in-situ stripping rate. A ring of Nd-Fe-B magnets enhances the plasma confinement. The magnets also improve the radial uniformity of the plasma density. Resonant RF traps, along with careful attention to proper grounding and shielding are utilized to eliminate RF interferences.

The neutralization efficiency depends on the choice of plate materials. The physics of these processes has been previously described in our earlier papers [13]. The neutral energy and flux are selected as follows. The plasma potential ( $V_p$ ) and the reflector bias ( $V_{bias}$ ) determine the energy of the ions that strike the reflector. Ions accelerate to an energy that is approximately equal to  $(V_p - V_{bias})$  with  $V_{bias}$  usually negative. As a general guide, the average energy of the reflected neutral is about thirty to fifty percent of  $V_p - V_{bias}$ . Hence the energy of the reflected neutrals can be tuned by adjusting the reflector bias. Lower pressure is maintained between the plate and the process region so that neutrals are not depleted by elastic charge-exchange collisions. The angle between the normal of the reflector plate and the axis of plasma region is also variable, permitting variations of the neutral flux in the process region. Earlier studies [11, 14] have shown that angles in the range of 40-60 ° are optimal for maximum neutral flux output. The exact optimal angle depends on the discharge gases and the plate material composition [14]. The determination of the flux has

been performed by comparison of recession rates to known standards developed for space applications [11, 14]. The computational model previously published [13] also computed the angle and energy dependent flux, which was found to be in agreement with the recession measurements. For the range of operating conditions reported in this chapter, the flux was  $7 \pm 1 \times 10^{14}$  atoms.cm<sup>-2</sup>s<sup>-1</sup>. Fluences are calculated using this flux, multiplying by the appropriate period of time.

Neutrals stream towards a sample holder. The sample holder can be replaced by a water-cooled quartz crystal microbalance for in-situ removal rate measurements. A collimator can be placed in front of the sample holder. The collimator, shown in Fig. 5.2, contains both bias-able grids and stands for UV light filters. This allows detailed studies of the relative contribution of charged particles and deep UV to the removal rates.

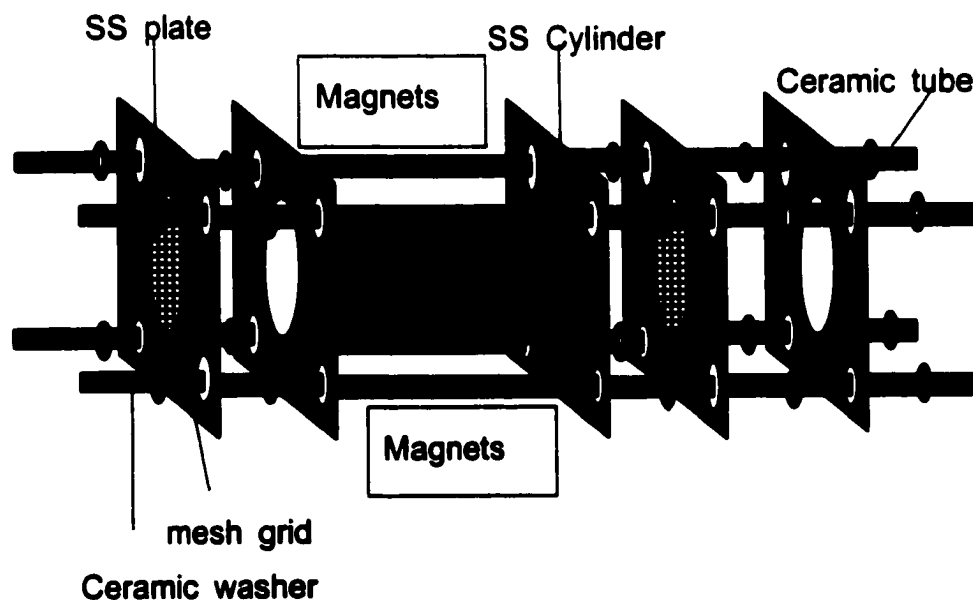


Figure 5.2: Schematic drawing of the ion and electron deflection neutral collimator

## 5.2.2 Experiment methods

### Plasma characterization

The performance of the ICP source was characterized primarily by Langmuir probe measurements. Radial profiles of the electron density  $n_e$  and the electron temperature  $T_e$  were derived from single- and double-probe current-voltage traces. These traces were interpreted using numerical fitting routines within the Laframboise's cylindrical probe model, correcting for sheath rectification effects [17]. In the downstream region, Langmuir probe and the plate ion saturation current measurements were compared to give a measure of ion density. Under certain conditions, plasma leakage into the process zone was measured using the collimator retarding grids shown in Fig 5.2. A picoammeter was used to measure the leakage current.

### Cleaning studies

Cleaning rates with different polymers by the neutral stream were studied with two classes of trials.

- The first class employed ex-situ measurements. The samples were fixed on the holder for exposure to the neutral flux. The gas composition, total pressure, reflector bias, and exposure time were varied. Post-exposure determination of the rates, and other aspects of the cleaning effectiveness, were evaluated by a variety of surface analytical techniques, including atomic force microscope (AFM), X-ray photoelectron spectroscopy (XPS), Auger spectroscopy, and variable-angle-spectroscopic ellipsometry (VASE).

- The second class of trials involved in-situ measurements of the cleaning rates

on spin-coated quartz crystal microbalance (QCM) samples. Both charge-particle filtering and neutral collection were applied.

In both classes of trials, the erosion rates and morphologies of a variety of spin-on materials and organic thin films were assessed. Commercial films, which had been previously established as a transfer standard by a number of oxygen-atom-beam research groups, were used in these experiments. These samples, and various spin-on samples of PMMA resists, were masked with 500× 500 line-per-inch W masks to evaluate undercutting and morphology.

## **5.3 Results and Discussion**

### **5.3.1 Neutral cleaning with the collimator**

Photoresist dimensions may be altered by etching from the background gases, or by shrinkage or direct mass loss of the photoresist from exposure to the uv light. Photoresist may also be removed by the directed neutral stream. To distinguish between these mechanisms, we covered one side of the sample with a 1 cm × 1 cm MgF<sub>2</sub> window held 2 mm above the sample to allow access from the thermalized background gas. This window transmits photons from the deep UV at about 1300 Å to the infrared and also allows thermalized neutral species to reach the sample, while blocking the fast neutrals to the sample. Fast neutral cleaning results on a silicon wafer covered by photoresist are shown in Fig. 5.3. The collimator was placed between the doped silicon and the reflector plate. Samples were exposed in the neutral beam to a





Figure 5.3: Comparison of the post-cleaned samples exposed to the neutral beams. 7 mTorr, Ar: 3.23sccm,  $O_2$ :9.32sccm, bias:-15 V, 500W. Left sample was exposed without  $MgF_2$  window, right sample was exposed with  $MgF_2$  window.

total estimated dose of  $8 \times 10^{17}$  O-atoms. $cm^{-2}$ . As seen in Fig. 5.3, the portion of sample exposed directly to the neutral beam source showed complete removal of the patterned polymer layer, while the portion behind the  $MgF_2$  window showed no removal. We have performed Auger, XPS, and EDX on the samples to assess the effectiveness of our beam in removing the photoresists. This effectiveness is verified by the comparison of the carbon level on the samples before and after cleaning. Fig. 5.4 shows representative XPS data. The 285 eV carbon (1s) peak, visible before cleaning, completely disappears after the process. On the other hand, the oxygen peaks (1s, 27.5eV and 2s, 533eV) increased significantly, along with the Si 2s and 2p peak intensities. Only a slight shift of the Si peaks toward to larger binding energy, consistent with oxidation, was observed. Fig. 5.4 also indicates no trace of

sputtered chamber (Fe, Ni, Cr, etc.) or reflector (W) materials on the sample. The Auger and XPS did not show these elements either. We conclude that resputtered materials were absent at a level of approximately 0.01 at% even after many hours of exposure. Previous results from our group showed that ions and electrons were completely removed from the stream by the collimator. So the source exclusively provided fast neutrals for the cleaning applications. The absence of erosion on the

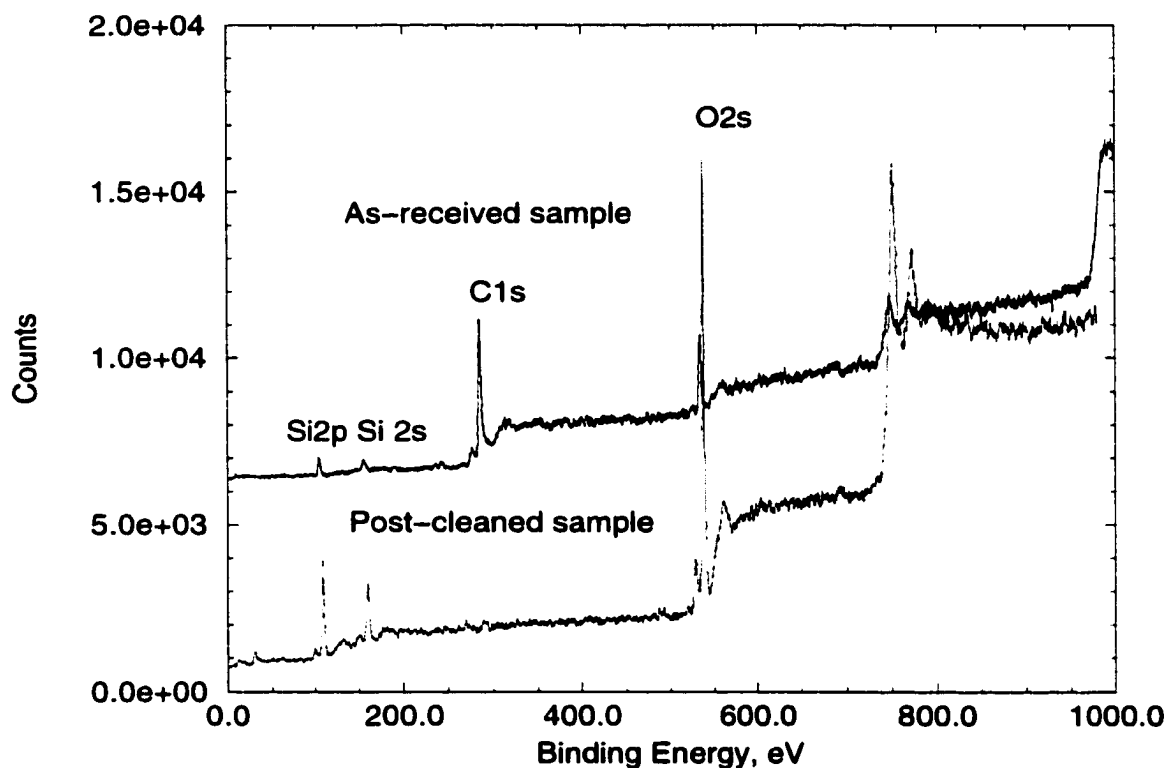


Figure 5.4: XPS spectra of the cleaning results for Si wafers with patterned photoresist residue

sample (Fig. 5.3), which was exposed to thermalized neutrals and uv photons, indicates that the reaction threshold is well above 0.025 eV. For most experiments

discussed in this paper, the plasma potential was at least a few volts. The reflector plate was biased at negative tens volts. So reflected neutrals should have an energy of 3~ 10 eV. This is high enough to remove the photoresist on the surface. Both thermal and non-thermal reactive channels contributed to the “soft” etching processes while the Langmuir-Hinshelwood mechanism played little role in our photoresist etching experiments. Other mechanisms such as collision-induced desorption, Eley-Rideal dynamics, and dynamic displacement mechanism all depend on the translational energy. With a low translational energy for neutrals, the dynamic displacement etching mechanism played little role [107]. The implication that the post-cleaned surface was atomically smooth, was confirmed by the AFM measurements. The surface roughness was less than 10.Å.

### **5.3.2 Cleaning rate measurements**

#### **In-situ cleaning rate measurements**

We measured removal rates of polymer PMMA with different rf power, reflector bias, gas composition and total pressure. Gold-covered quartz crystal microbalance sensors were spin-coated with PMMA, baked for one hour, and subsequently exposed in the process region. Fig. 5.5 summarizes the removal rates as a function of the rf power input at different discharge pressures without the collimator. The removal rates increased with the rf input power, but they did not increase monotonically with the total pressure. The removal rate at 18.4 mTorr had the lowest value. The highest removal rate appeared at 9.0 mTorr. The cleaning rate as a function of the rf power with the collimator installed is shown in Fig. 5.6. For different gas compositions, the

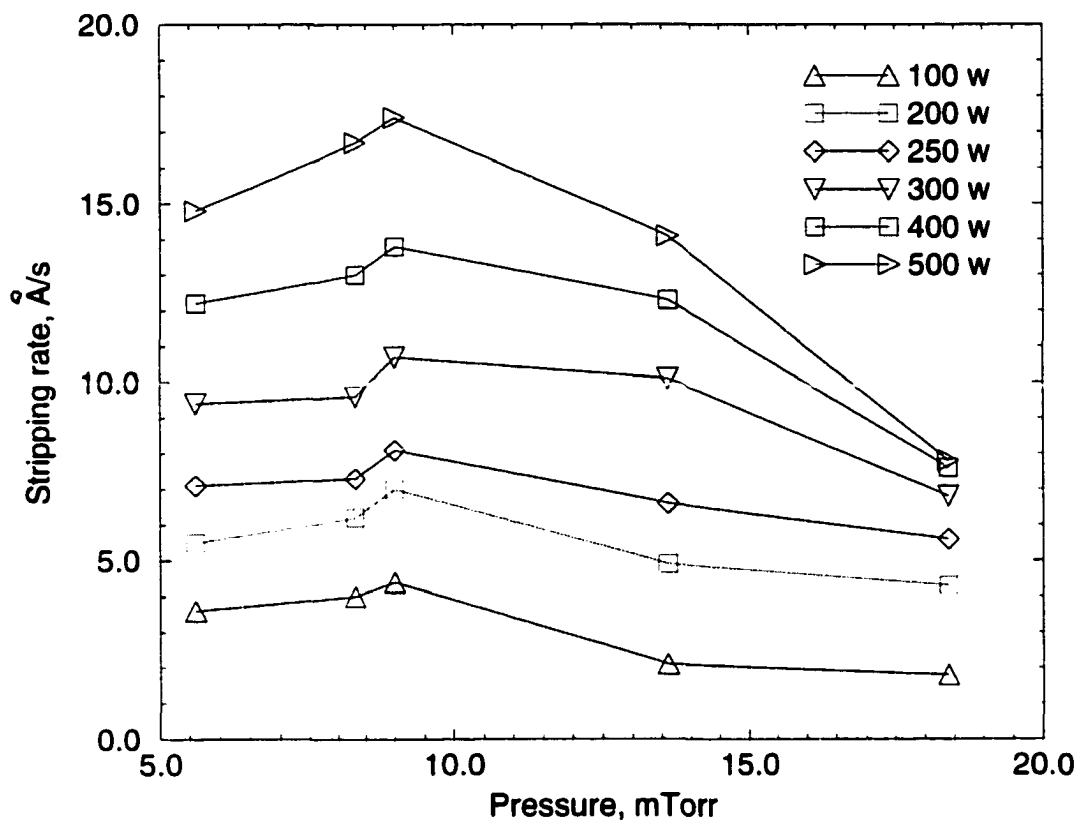


Figure 5.5: Stripping rates as functions of the rf power and total pressure.(Bias:-13.4 V, Ar: 3.66 sccm, $O_2$ : 8.23 sccm.)

cleaning rate(with the collimator), increased linearly with the rf power. It should be noted that the cleaning rate with the restriction of the collimator is much slower ( $< 1 \text{ \AA/s}$ ) at 500W than it is for the uncollimated case.

The photoresist etch rate with hyperthermal neutrals can be estimated quantitatively, as follows:

$$ER(x, y, z, E_n) = n(x, y, z, E_n) * \gamma(E_n) \quad (5.1)$$

where ER is the position and energy dependent etch rate, n is the neutral flux reaching

the wafer surface, which is a function of position  $(x,y,z)$  and the neutral energy,  $E_n$ . The etch yield,  $\gamma$  is also a function of the neutral energy. Etch rates were found by integrating the above equation over the energy distributions.

Higher rf power generally enhanced the neutral flux, which led to higher cleaning rates. Langmuir probe measurements in Chapter 2 indicated that the electron temperature varied little as the rf power was increased from 200W to 500W. Over the same power range, the plasma density increased by a factor of two, which was confirmed by a corresponding increase of the reflector plate current. As predicted by

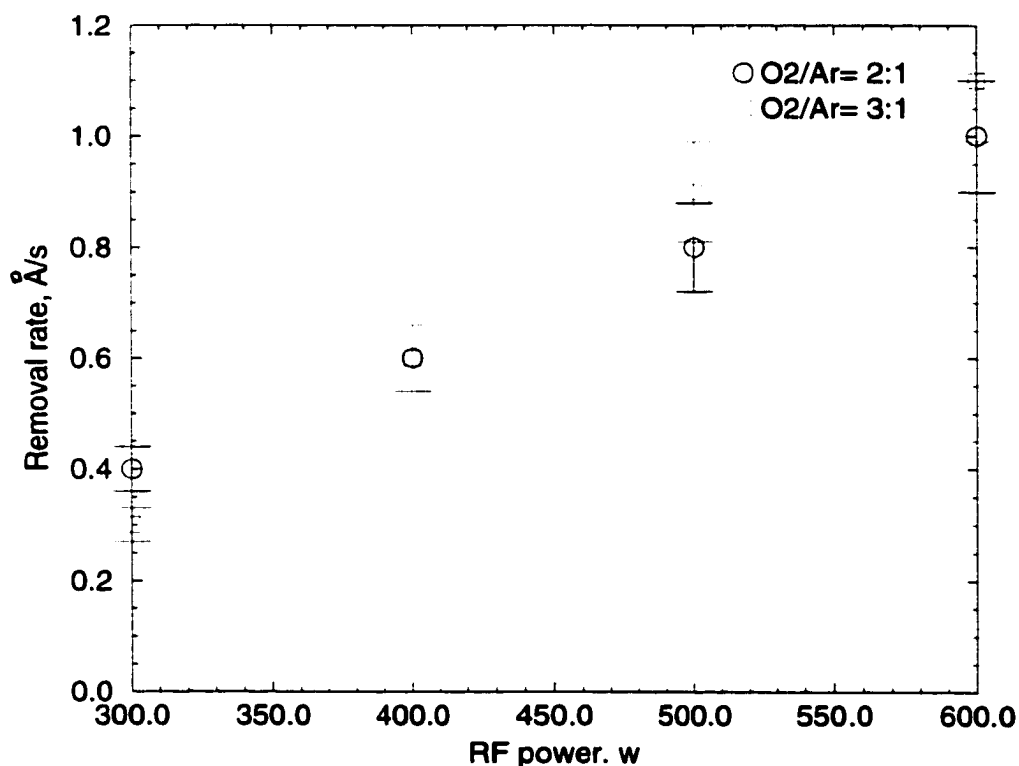


Figure 5.6: Neutral stream cleaning rates as a function of the rf power. (8mTorr, bias:-18.4V with collimator)

the earlier modeling of Nichols and Manos [14], these trends led to an observed increase of the removal rates.

The pressure dependence of the removal rate (Fig. 5.5) can be interpreted as a competition between increasing ion flux to the reflector plate as the pressure increased initially, and the attenuation of the reflected neutrals by charge-exchange and elastic scattering as the pressure increased further. The removal rate with the collimator also increased with the rf power (Fig. 5.6). The rate, however, was only about one tenth of the rate without the collimator. This was caused by a reduction of the off-axis neutral flux, in rough agreement with our previous calculation [13]. The cylindrical collimator has a length/diameter ratio of 2:1, giving a  $14^\circ$  angular acceptance from the source zone on the reflector. Integrating an assumed cosine distribution from  $0$  to  $14^\circ$  predicted a ratio of flux without and with the cylindrical collimator of about 6.6:1. Photo-resist removal rates by neutrals have been found to be lower for oblique incidence [108], thus the ratio of removal rates is expected to be higher than that of the fluxes, also in agreement with these observations.

One main advantage of this neutral beam source over conventional downstream sources is the ability to tune the neutral energy over a broad range to meet the threshold energy requirement for different processes such as Si etching, PR ashing, etc. The average energy of the fast neutrals is strongly affected by the interaction with the background in the process region. The effect of reflector bias on the PMMA removal rate is shown in the Fig. 5.7. The removal rate remained nearly constant as the bias varied from 0 to -30 volts.

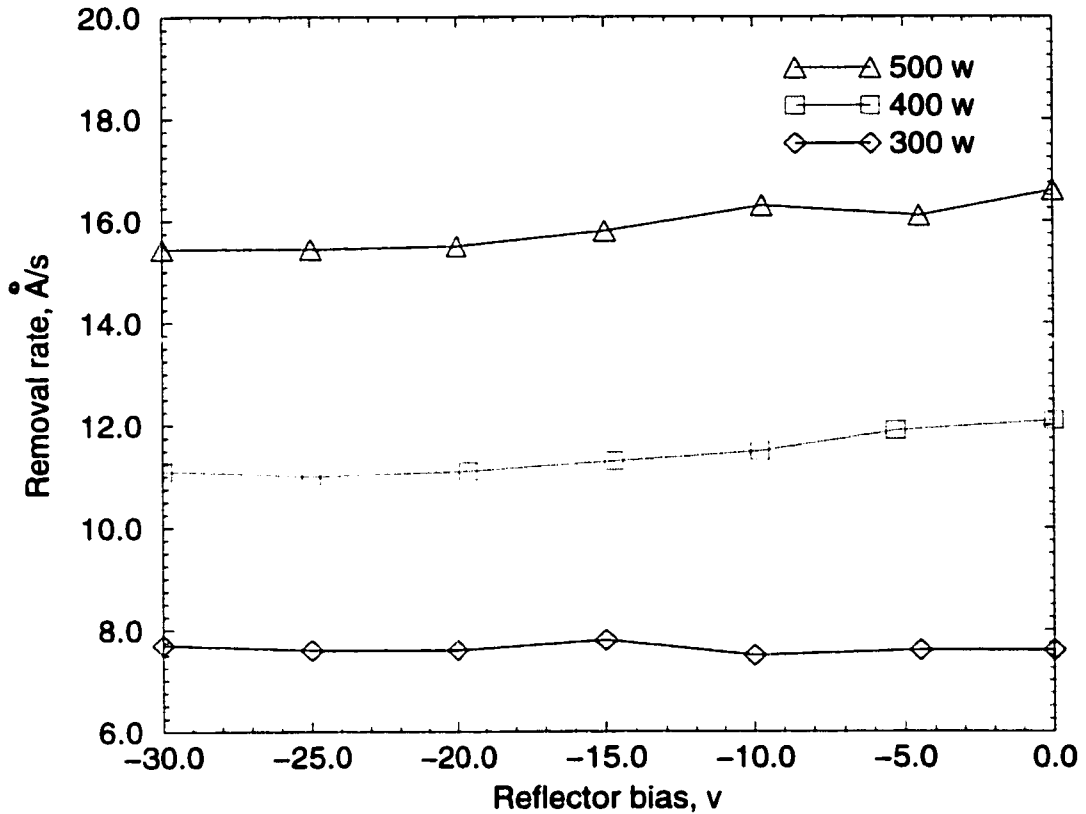


Figure 5.7: PMMA removal rate as a function of the reflector bias. (7.8mTorr, Ar:3.66sccm, O<sub>2</sub>:8.23sccm)

Polymethyl methacrylate (PMMA) used in the experiments has two different activation thresholds depending on whether the substrate temperature is above or below the glass transition temperature,  $T_g$  [15]. For PMMA,  $T_g \sim 60-90^\circ\text{C}$ , with  $E_a=0.2$  eV for  $T < T_g$  and  $E_a=0.4$ eV for  $T > T_g$  [15]. Measurements showed that the plasma potential decreased as the rf power increased, but stayed above 11 volts. This implied the minimum neutral energy was around 3-5 eV, well above the reaction threshold. Experimentally, we found that the ion flux to the reflector was nearly constant as the

bias was varied below -10 volts. Hence we expected that the neutral flux impinging

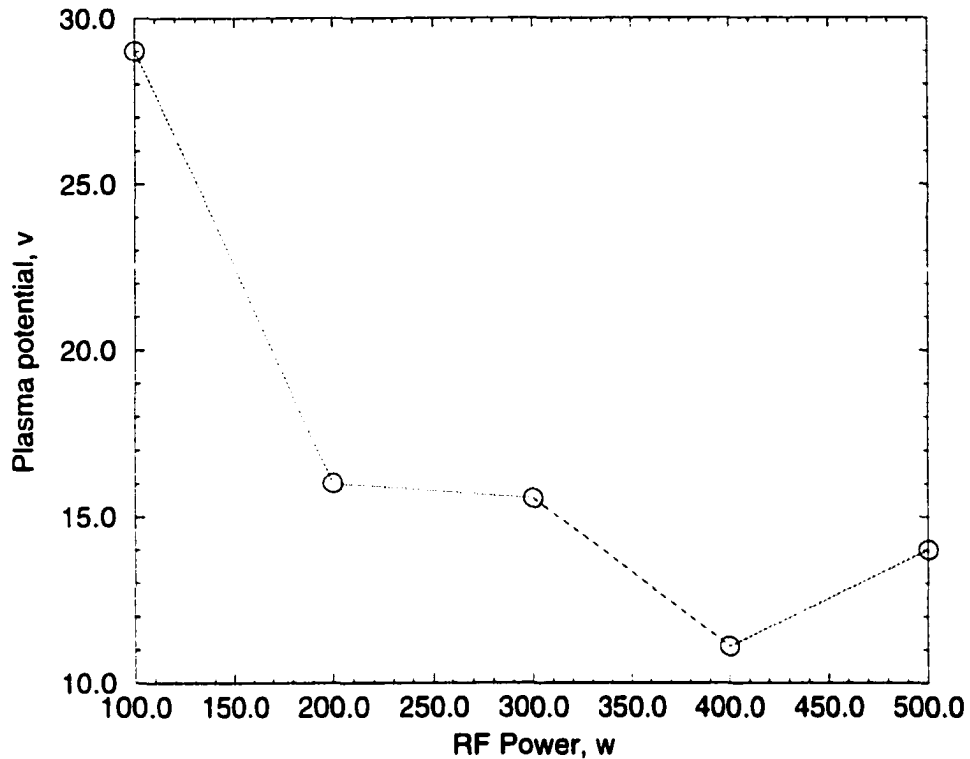


Figure 5.8: Calculated plasma potentials as a function of the rf power from the Langmuir probe data

on the PMMA remained unchanged. According to Cross [107], etch yields for hyperthermal oxygen neutrals on Kapton rise four orders of magnitude from thermal velocities up to 3 eV, where the etch yields begin to saturate. The etch yield at 3 eV is approximately two-thirds of the value at 5 eV. PMMA has a lower reaction threshold than that of Kapton, and the etch yield of PMMA tends to saturate at a lower translational energy. Thus in cases where the hyper-thermal neutral energy is well above 3 eV, the removal rate for PMMA does not vary significantly as the re-



flector bias changes. This may not be true for etching materials with higher reaction thresholds or different neutral source designs especially those using grid neutralizers. We expect that at much higher energy physical sputtering could enhance the removal rate, but with the risk of damaging the surface.

Experiments showed that the cleaning rate increased linearly with the value of  $O_2/(Ar+O_2)$  ratio over the range from 0 to 0.8 and remained constant over the range from 0.8 to 1.0. We found that pure oxygen had a cleaning rate of  $11.7 \text{ \AA}/s$  equal to the maximum, within the scatter of the data. This differed from the findings of Goecker *et al.* [12], who observed no cleaning effect using pure oxygen in their neutral source. The difference may result from a higher velocity in the reflected neutrals in our experiment, or perhaps represents an enhanced atomic to molecular recombination rate in the gridded neutralizer of their apparatus.

### **Ex-situ removal rate measurements with the collimator**

P-doped Si, spin-coated with PMMA, was dried in an oven for one hour at  $98^\circ C$ . Ellipsometry measurements indicated a film thickness of  $9000 \text{ \AA}$  prior to cleaning. Exposures to the neutrals were carried out during room temperature water cooling on the sample holder for periods up to 6 hours. The residue thickness was measured with AFM and ellipsometry. We found that the average removal rate was around  $0.8 \text{ \AA}/s$  with the collimator. Without the collimator, the removal rate increased to  $10.1 \text{ \AA}/s$ . Ex-situ measurements are in good agreement with the in-situ ones. Similar measurements were made on free-standing Kapton films for which the removal rate was  $9 \text{ \AA}/s$  without the collimator. With the collimator, the removal rate was reduced to  $1.89 \text{ \AA}/s$ . The small difference in rates implies a lack of selectivity for potential

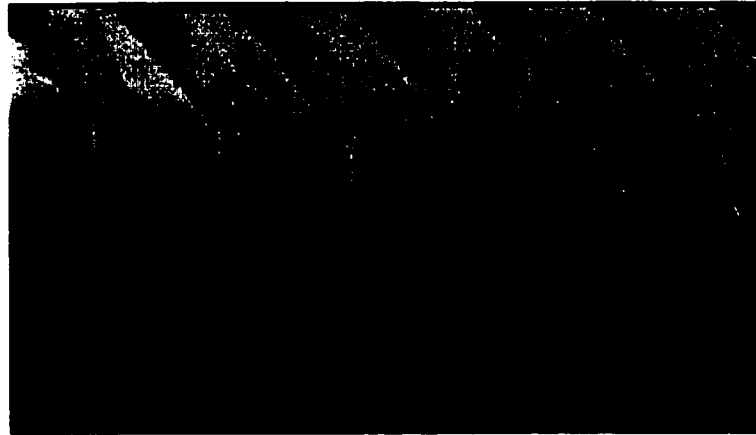
patterning applications.

### 5.3.3 Trench cleaning studies by the neutral beam

Cleaning of post-metal etch residues is difficult to do without wet steps, or without aggressive direct plasma exposure. Therefore, at the request of colleagues at IBM, we investigated the efficiency of our neutral stream for this application. Two types of trenches,  $1\ \mu\text{m}$  (width)  $\times$   $0.25\ \mu\text{m}$  (depth) and  $0.25\ \mu\text{m} \times 0.25\ \mu\text{m}$  were used in these experiments. These features were created by a post-metal etch process leaving W containing polymer residues on the bottom and sidewalls. After spin-coating with PMMA, they were baked in an oven at  $98^\circ\text{C}$  for one hour prior to exposure. Long exposures (3~4 hours) were performed to provide comparisons to damage studies during severe over-etch. Longer exposures (over 6 hours) were also required to assess critical dimension loss. The morphology of trenches after 6 hours in the neutral stream is shown in Fig. 5.9. Trenches with an aspect ratio of 1:4 achieved sharp edges (Fig. 5.9) and appeared to be free of residues. On the other hand, some residues may be seen at the bottom and on the sidewalls of trenches with an aspect ratio of 1:1 (Fig. 5.9b). To further examine possible contamination due to sputtering, we exposed an ultra-pure crystalline  $\text{MgF}_2$  sample to the neutral flux for a period of two hours. No trace of any metal elements (W, Cr, Fe, Ni) were found in surface spectra taken by XPS and Auger. The survey scans of cleaned trenches also indicated that no new compounds formed at the bottom or on the sidewalls, even though the sample had been exposed to the neutral stream for over six hours, yielding an over-etch of several hundred percent. In order to get information on the species present in the



**(a)  $0.25\mu\text{m} \times 1\mu\text{m}$  trenches**



**(b)  $0.25\mu\text{m} \times 0.25\mu\text{m}$  trenches**

**Figure 5.9: Scanning electron microscopy micrographs of trenches with different aspect ratios using the neutral source**

interior of the cleaned trenches after neutral processing, we tilted the sample to preferentially collect sidewall information under the X-ray source, taking care to account for possible variation of chemical bonding on the flat “lands” between trenches when the sample was tilted. A nonlinear fitting algorithm [109] was used to quantitatively analyze the Si 2p peaks. This analysis showed that SiO<sub>2</sub>/Si ratio increased as the rotation angle increased, indicating that a thin oxide film had formed on the top of the trench sidewalls. In general, the peak of carbon will shift to higher binding energies as the element reacts chemically with oxygen. The XPS spectra of the angled-resolved carbon peaks are shown in Fig. 5.10. As the tilting angle increased, the carbon peak

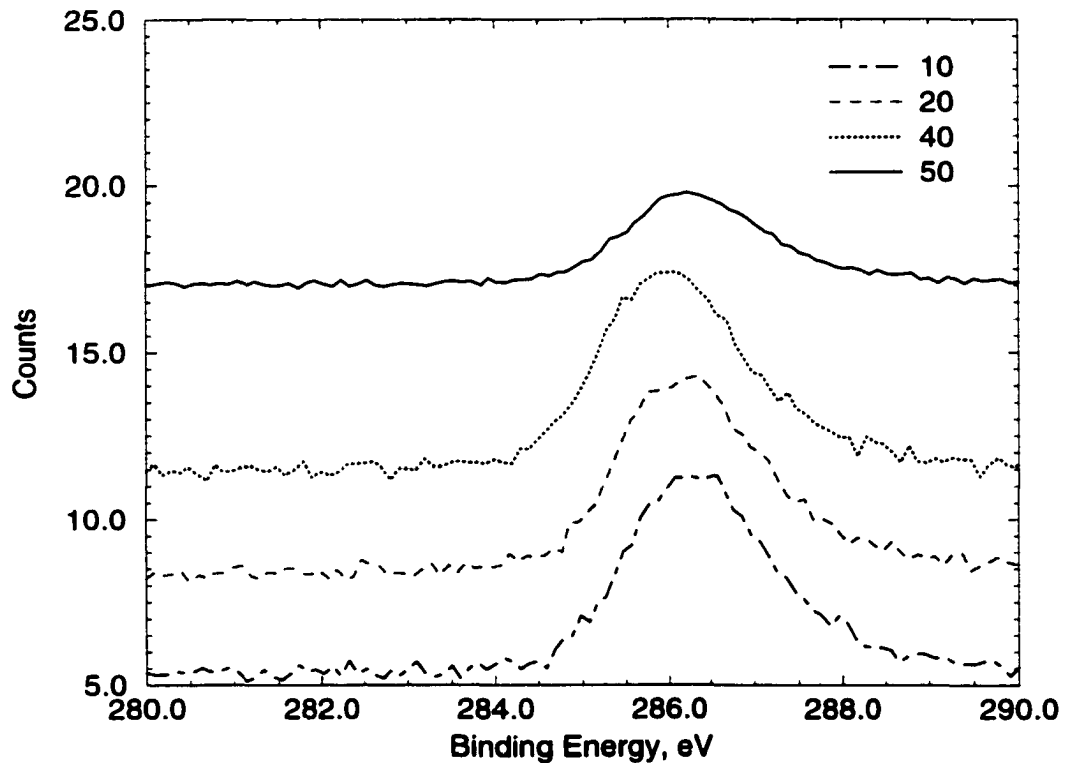


Figure 5.10: Angle-resolved XPS spectra of carbon peaks after neutral processing

shifted to lower energy first and then moved back to high binding energy. The data in Fig. 5.10 is consistent with the presence of unreacted carbon compounds on the sidewalls. We cannot say unequivocally whether these materials were sputtered from the bottom of trenches or whether they were post-processing residues, initially present on the sidewalls, that were not removed by directed beam of fast neutrals.

## 5.4 Summary

Our experiments demonstrated that a broad-area, reflection neutralization source can provide controllable fast neutrals for cleaning applications. The observations confirmed the predictions of our earlier computational models of this apparatus. The cleaned Si surface had a surface roughness less than 1 nm. In-situ and ex-situ measurements showed a removal rate of  $10 \text{ \AA/s}$  for PMMA, which is suitable for cleaning and soft-landing etching steps. The removal rate increased linearly with rf power and was nearly constant as the reflector bias varied from 0 to -30 volts. The total pressure affected the removal rate significantly. XPS studies showed no detectable contamination from the chamber or the reflector materials. Angle-resolved XPS spectra indicated the presence of unremoved carbon compounds on sidewalls and the formation of  $\text{SiO}_2$  on the top portion of trench sidewalls, consistent with a directional fast neutral flux.

# Chapter 6

## Neutral Stream Characterization of a Surface Reflection Materials Processing Source

### 6.1 Introduction

Neutral atomic and molecular beams have numerous applications. For example, neutral beams can be used to perform charge-free etching, deposition processes and molecular beam epitaxy. Neutral beams can also be used for surface reaction mechanism and beam interaction studies. Neutral sources such as nozzles [110], grid neutralization sources [105, 111], laser ablation [104], and surface reflection sources [11, 13] have been investigated exclusively for the semiconductor processing. Etching [104] and cleaning applications [12, 51] using such sources have been reported. However, a lack of information relating the plasma discharge to neu-

tral flux properties, including detailed measures of neutral flux and energy has slowed down the deployment of these sources. In this chapter, direct measurements of the neutral beam energy and flux as functions of plasma parameters are presented.

Such measurements have not been reported routinely because direct measure of a hyper-thermal beam is difficult. Time-of-flight [112] and quadrupole mass spectroscopic techniques [11], while difficult, have under special circumstance been able to provide information on neutral energy distributions. Direct particle measurement using photo-resist ashing, recession rates of photo-resist [113], metal oxidation [114] and catalytic thermocouple probes [115] have yielded some flux measurements.

Such studies have worked only for specially selected systems because they rely on the accurate knowledge of process constants, such as the etch yield. In most cases, it has been difficult to precisely determine the absolute flux density of the beams. This problem is compounded when the beams are composed of high-energy particles, or reactive and/or condensible species. For example, the hyper-thermal atomic oxygen fluxes could be determined by exposing a thin strip of silver deposited on a non-conducting, non-reactive substrate to the beams. Measuring the electrical resistance of the silver strip as a function of time was used to determine the rate of material conversion to a non-conducting oxide. However, flux measurements made using this technique have large uncertainties because of following assumptions for the calculation: the sticking probability of oxygen atoms on bare polycrystalline silver is unity and independent of the degree of oxide formation; the nearest neighbor distance of atoms in polycrystalline silver is that of silver face-centered-cubic structure; and  $O_2$  molecules in the beam do not react with the silver to form silver oxide.

Most of above methods developed for measuring the flux of the beams have proven to be expensive, time consuming, limited to a small class of molecular beams, and generally yield results with large uncertainties. Recently, Cook *et al.* [116, 117] developed a specialized torsion balance which is capable of measuring directly the absolute flux density of hyper-thermal beams in an ultra high vacuum environment. Torsion balances measure the absolute flux densities of molecular beams composed of non-reactive gases by measuring the forces exerted by the beams on plates mounted on the lever arms of the balances. With accurate measurements of balance rotations of  $10^{-9}$  rad, for a lever arm length of 5 cm, a torsion balance could measure forces of less than  $10^{-20}$  N. This means that this set up is capable of measuring the neutral flux at the order of  $10^{10} \text{ cm}^{-2} \text{ s}^{-1}$  with neutral energy over 2.5 eV.

A similar, highly sensitive torsion balance was built and used in the measurements reported here for the neutral flux measurement. A micro-calorimeter was used for energy measurements of the neutrals. With this combination, we are able to derive both the neutral energy and neutral flux.

To our knowledge, no previous studies have combined such flux and energy measurements for a neutral processing source. We also correlated these neutral flux and energy measurements for  $O_2$  plasmas to our previous cleaning rate measurements (Chapter 4) by QCM to provide an independent consistency check on the methods.



## 6.2 Experiment Setup and Methods

### 6.2.1 Vacuum system

The experiments were carried out in the apparatus shown in Fig. 6.1. The apparatus consists of three 8" CF six-way crosses. The plasma source chamber has been described in Fig. 5.1. The intermediate chamber was pumped by a 450 l/s turbomolecular pump while the test chamber is pumped by a 360 l/s turbopump. The base pressures in these chambers were monitored by three ionization gauges. During the discharge, the capacitance manometer was turned on in place of the ionization gauge. A micro-calorimeter is located in the source region. An vacuum compatible torsion balance is placed in the test chamber.

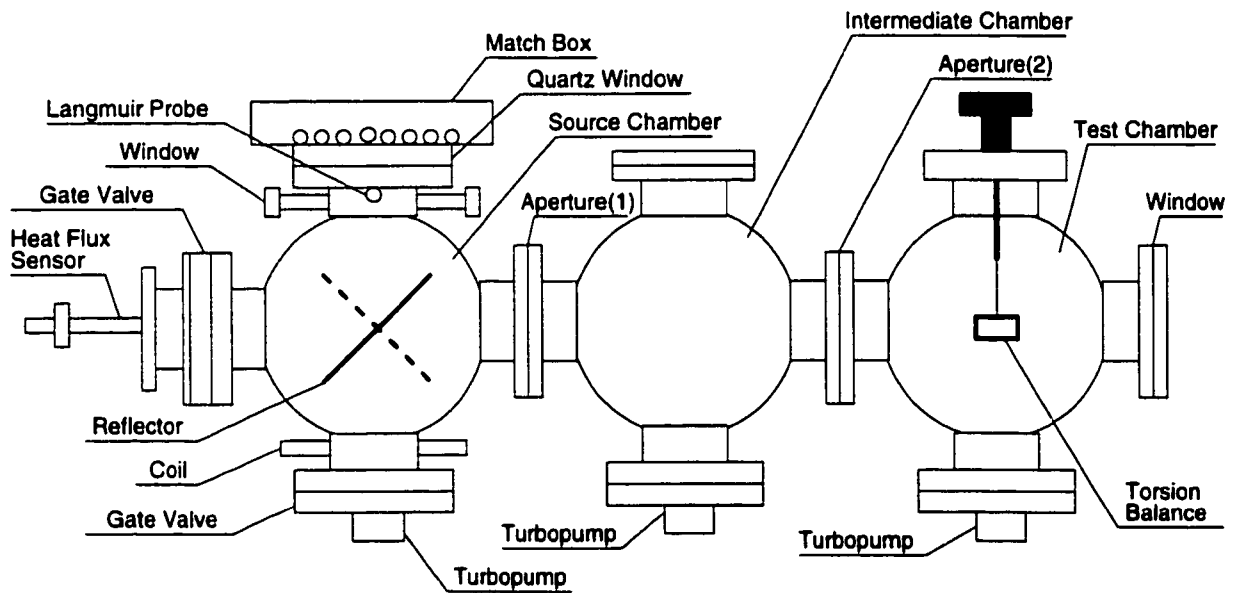


Figure 6.1: Vacuum system for the neutral beam characterization

## 6.2.2 Torsion balance

Fig. 6.2 shows the schematic drawings of the torsion balance. The molecular beam loses its momentum to the torsion balance by impinging on a rough flat plate mounted on the torsion balance lever arm. The ideal situation is that the beam scatters off of the plate diffusely with complete thermal accommodation. One approach is to arrange for a simple reflection of incident neutral beam to the flat plate on the torsion balance while an alternative approach is to use a beam trap such as an aluminum foil sphere with a small aperture to trap the incident beams. However, the exit flux through the aperture in the sphere might not equal the entrance flux, and the general relationship between the exit and entrance fluxes will most likely be unknown. Other methods such as directing the beam into a chamber through a knife edge aperture and then measuring the pressure increase in the chamber due to the incoming molecules can also provide the flux value. The special beam catcher designed by Cook *et al.* [116, 117] allows the incident particles to reach thermal equilibrium completely in the beam catcher. In our apparatus, this is combined with a micro-calorimeter to extract both the neutral flux and neutral energy measurements.

Particles enter the beam stop and impinge upon a flat surface at a large incident angle. The angle between the surface normal and the beam was  $76^\circ$ , and the solid angle subtended by the entrance aperture of the beam stop from the impingement point was small, 0.027 sr. Very few incident particles will reflect directly back out through the entrance aperture, and those that do not react with or stick to the inner surface will reach thermal equilibrium with the beam stop by making, on average, many collisions with the walls before exiting. Particles then exit both apertures

diffusely with identical velocity distributions. The average momentum of particles exiting the entrance aperture will be the same in magnitude as the average momentum of particles exiting the other aperture. To increase the sensitivity of the torsion balance, most components of the torsion balance were constructed from aluminum sheet to reduce their contribution to the total moment of inertia. The beam stop had a length of 10cm, a diameter of 2.8cm, and a wall thickness of 0.12 mm. The beam stop end caps were constructed from 0.12-mm-thick shim stock, and had aperture diameters of 0.89cm on both ends. The cross beam and central axis of the torsion balance were constructed from a 0.3-cm-diam cylindrical rod. The central axis length was 12.5cm, and the torsion balance lever arm length, defined to be the distance from the axis of rotation to the center of the beam stop was 3.796cm. The damping disk was circular, with a diameter of 6.25cm, and was constructed from 0.38-mm-thick shim stock. The overall mass of the torsion balance was approximately 24.5g. Gold-coated tungsten suspension wires were used that had diameters of  $15\mu\text{m}$  or  $25\mu\text{m}$  and lengths of about 10 cm were used in the calibration and measurements. The torsion balance was situated in the differentially-pumped test chamber. The apparatus is configured so that the reflector plate can be rotated to direct the neutral stream toward different analysis or processing zones. For momentum measurements, the reflected neutral flux travels through a 0.8 mm diam. aperture, the intermediate drift chamber, and through a 2 mm aperture into the test chamber. The apertures are optically aligned so that all of the analyzed neutral flux entered the particle catcher of the torsion balance. During the operation of the source chamber at pressures from 1~ 10 mTorr, the pressure in the analysis chamber does not exceed  $1.5 \times 10^{-7}$  Torr. This assured

that the attenuation of the reflected neutral flux due to charge-exchange or elastic scattering was less than 1%.

The energy carried by the reflected flux is measured by rotating the reflector plate toward a micro-calorimeter positioned in a sidearm connected to the source chamber. The calorimeter has a time response of  $6 \mu s$  and a sensitivity of  $150 \mu W cm^{-2}$ . In the same sidearm, approximately 1 cm in front of the calorimeter we have placed a multi-grid electrostatic deflector capable of keeping charged particles from striking the detector, and a  $MgF_2$  beam stop capable of permitting only uv photons to reach the detector. Heat flux readings with and without such filtering are then used to determine the energy carried by the neutral components. Proper accounting for the filter's reduction of the angular acceptance of the detector is required.

### 6.3 Theory of torsion balance operation

With a particle beam scatters off of a surface, the force exerted on that surface by the beam is:

$$F_{beam} = A\Phi m\bar{v} - N_r m\bar{v}_r, \quad (6.1)$$

where  $A$  and  $\Phi$  are the cross-sectional area and flux of the beam, respectively;  $N_r$  is the number of particles scattering off of the surface per unit time;  $\bar{v}$  and  $\bar{v}_r$  are the flux-weighted average velocities of the incident beam and scattered molecules, respectively; and  $m$  is the mass of the beam. The flux-weighted average velocity is defined by Cook,  $f_\Phi(\nu)$ , for a one-dimensional beam of molecules by letting  $f_\Phi(\nu)d\nu$  represent the number of molecules in the beam that cross a unit surface area per unit

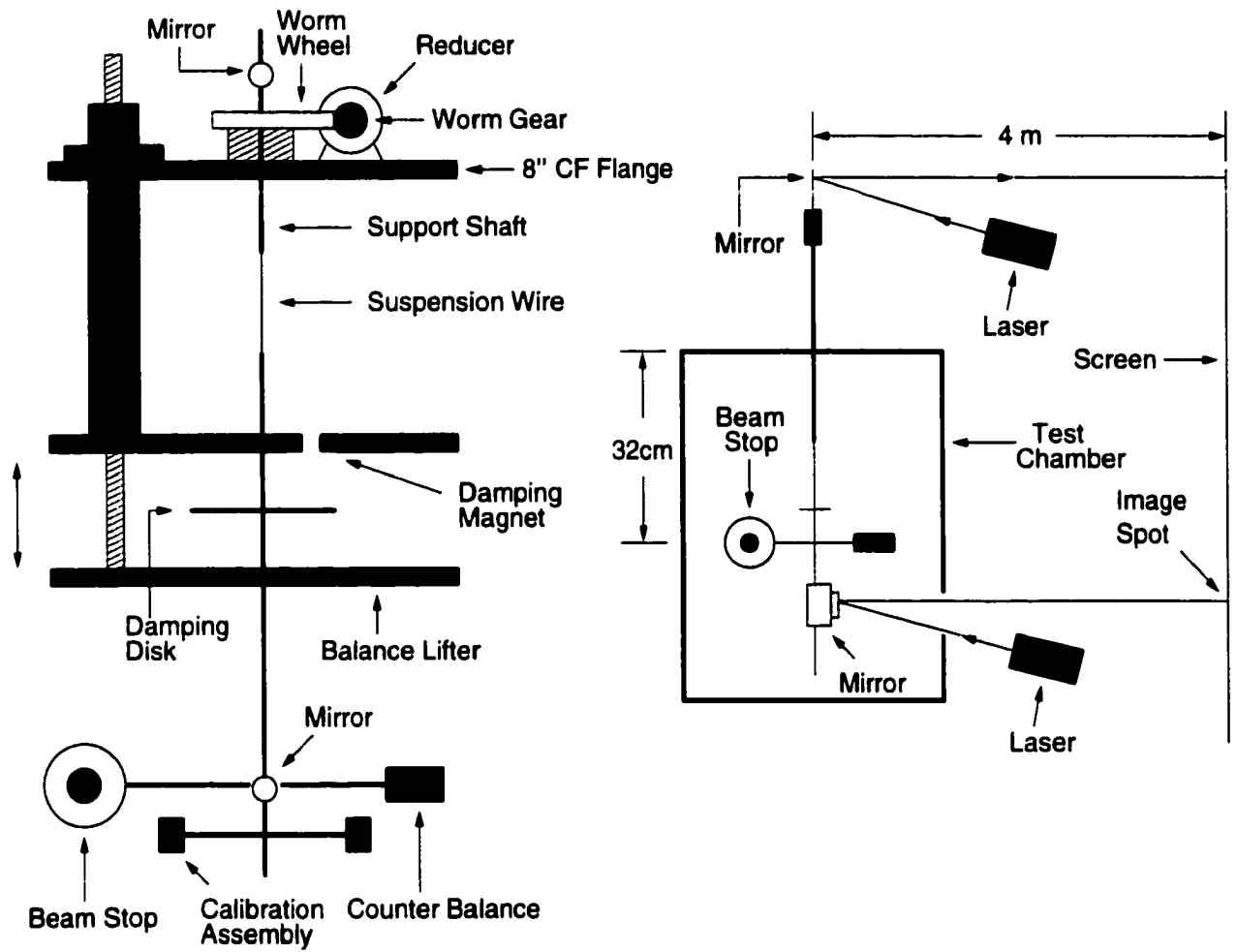


Figure 6.2: Schematic drawing of the torsion balance

time with velocities between  $\nu$  and  $\nu + d\nu$ . The flux of the beam is then given by

$$\Phi = \int_0^{\infty} f_{\Phi}(\nu) d\nu. \quad (6.2)$$

and the flux-weighted average velocity of the beam is defined as [117]

$$\bar{\nu} = \frac{1}{\Phi} \int_0^{\infty} \nu f_{\Phi}(\nu) d\nu. \quad (6.3)$$

The average velocity of the exiting particles,  $\bar{\nu}_r$ , was assumed to be zero with the special beam catcher.

$$F_{beam} = \Phi A m \bar{\nu}. \quad (6.4)$$

The aperture  $A$  must collimate the beam to a small enough diameter so that the entire beam passing through the aperture enters the beam stop.

When the beam enters the beam stop,  $F_{beam}$  causes the torsion balance to rotate by producing a torque about the axis of rotation, defined by an imaginary line through the symmetry axis of the suspension wire. The torque,  $\Gamma_{beam}$ , is equal to  $F_{beam}$  times the lever arm length  $l$ . A restoring torque was applied to the shaft to return the balance to its original angular position by twisting the suspension wire in the opposite direction. The torque applied by the twisted wire,  $\Gamma_{wire}$ , for small rotations is given by

$$\Gamma_{wire} = k\xi = \left(\frac{S\pi R^4}{2d}\right)\xi, \quad (6.5)$$

where  $S$ ,  $R$ , and  $d$  are the shear modulus, radius, and length of the suspension wire, respectively, and  $\xi$  is the angle through which the suspension wire was rotated.  $\Gamma_{wire}$  is the torque required to return the balance to its original angular position. The

parameter  $k$  is the torsion constant of the suspension wire. At equilibrium, the net torque on the balance is zero. Therefore, the torque applied by the incident beam was equal in magnitude to the torque applied by the twisted wire, or

$$lF_{beam} = k\xi. \quad (6.6)$$

### 6.3.1 Suspension wire rotation angle measurement

The rotation angle  $\xi$  was measured using two HeNe laser beams. A HeNe laser beam reflected off of a mirror mounted on the torsion balance was focused onto a distant wall. As the balance rotates due to the torque produced by the incident beam, the laser image spot position moves along the screen. The suspension wire was then twisted in the opposite direction by turning the suspension shaft feed-through with a worm gear until the spot was returned to its original position. Because the balance had been returned to its original position, the angle the suspension shaft was rotated through equals  $\xi$ . The angle was measured by reflecting a second laser beam off of a mirror mounted on the suspension shaft feed-through and focusing it onto the same distant wall as before. The distance from the axis of rotation of the torsion balance to the laser beam spot detection wall,  $D$ , was 4.00 m. The relationship between  $a$ , defined to be the distance the spot moves along the wall in restoring the balance to its original position,  $D$ , and the angle  $\xi$  is

$$\xi = \frac{1}{2} \tan^{-1}\left(\frac{a}{D}\right). \quad (6.7)$$

### 6.3.2 Torsion constant calibration

The suspension wire was calibrated to determine the torsion constant, knowledge of the shear modulus, radius, and length of the suspension wire under actual load conditions would be required. However, since these quantities would be difficult to measure accurately, the torsion constant was experimentally determined by measuring the oscillation period of the torsion balance. The only torque applied to the balance was the one produced by the suspension wire, and the equation of motion that describes the balance is given by [116]:

$$I\ddot{\xi} = -k\xi, \quad (6.8)$$

where  $I$  is the moment of inertia of the torsion balance.

$$\xi(t) = \Theta \cos(\sqrt{\frac{k}{I}}t + \xi), \quad (6.9)$$

where  $\Theta$  is the oscillation amplitude,  $\xi$  is the phase constant, and  $\sqrt{k/I}$  is the angular frequency. The oscillation period of the torsion balance,  $T$ , given by

$$T = 2\pi\sqrt{\frac{I}{k}}. \quad (6.10)$$

Due to torsion balance's complicated geometry, the torsion constant cannot be uniquely determined. By attaching a calibration dumbbell assembly with a known moment of inertia,  $I_d$ , to the balance, the oscillation period becomes

$$T_d = 2\pi\sqrt{\frac{I + I_d}{k}}. \quad (6.11)$$

The calibration dumbbell assembly could also be removed and replaced with a cylinder of equal mass but a much smaller known moment of inertia  $I_c$ . With the cylinder



attached, the oscillation period is

$$T_c = 2\pi\sqrt{\frac{I + I_c}{k}}. \quad (6.12)$$

Using above equations to eliminate  $I$ , the torsion constant is given by

$$k = 4\pi^2 \frac{I_d - I_c}{T_d^2 - T_c^2}. \quad (6.13)$$

### 6.3.3 Torsion balance damping

Without external damping, any perturbing torque acting upon the torsion balance would cause it to oscillate about its axis of rotation for many hours. An external damping mechanism was developed utilizing faraday's law of electromagnetic induction. A permanent magnet was suspended approximately 2.5 mm above the damping disk on the torsion balance as shown. When the balance rotated, the changing magnetic flux through the disk produced eddy currents that converted the rotational energy into heat. Since the magnetic flux through the disk was constant when the balance was stationary, damping torques only occurred when the balance was rotating. The damping mechanism was specifically designed so that the torque it exerted on the balance would be zero at equilibrium. Since this torque would most likely change in an unpredictable manner each time equilibrium was reached, additional uncertainty of  $F_{beam}$  would result.

## 6.4 Results and Discussion

### 6.4.1 Neutral Energy and Flux Measurement

The accuracy of the momentum measurement strongly depends on the calibration of the torsion constant. The details of this calibration can be found in the papers of Cook and coworkers [116, 117], whose methods we used to calibrate the torsion constant. We also did a secondary calibration using an effusive source of known particles and momentum flux. The measured torsion constant is  $2.9 \pm 0.4 \times 10^{-8}$  N.m/rad. The force equation becomes :

$$F_{beam} = \Phi A m \bar{v} = \frac{k\xi}{L}, \quad (6.14)$$

where  $\xi$  is the angle through which the suspension wire must be rotated to return the balance to its original angular position and  $L$  is the particle catcher arm length (3.796 cm). This force measurement is used in the calculated momentum below. The neutral heat flux is derived as follows. In an Ar plasma, Ar atoms are the only fast neutral species coming from the reflector; prior work has shown that no sputtering or fast desorbed species are released from the plate. The total measured heat flux can be written:

$$Q = Q_{photons} + Q_{charged\ particles} + Q_{thermalized\ neutrals} + Q_{fast\ neutrals} \quad (6.15)$$

where  $Q_{photons} + Q_{thermalized\ neutrals}$  were measured by placing the  $MgF_2$  filter 1cm in front of the sensor head. Further filter experiments, using the ion and electron deflector, showed no detectable heat flux contribution from charged particles. This is as expected from our earlier work, which indicated that the charged fraction of

the neutral stream in the process zone was below our detection limit of 0.1%. The detected heat flux from fast neutrals can be written:

$$Q_{fast\ neutral} = \phi \cdot (1 - \gamma) \cdot E_{incident}, \quad (6.16)$$

where

$$E_{incident} \approx \frac{1}{2} m \bar{v}^2, \quad (6.17)$$

and  $\gamma$  is the ratio of scattered neutrals to incident fast neutrals at the detector. Assuming that the energy accommodation coefficient of the fast neutrals at the detector is unity, we arrive at the equation for the flux-weighted average velocity:

$$\bar{v}_{Ar} = \frac{2Q_{fast\ neutral} AL}{k\xi}. \quad (6.18)$$

This is combined with momentum measurements to yield a consistent value for the neutral flux. Fig 6.3 shows results for pure argon and for oxygen plasmas for varying rf power. The measured fast neutral energy does not vary much at fixed reflector bias,  $V_b$ , as the rf power increases because the plasma potential,  $V_p$ , is nearly constant for bias voltages below - 5 V.

As the rf power increases, the plasma density increase causes the neutral flux to increase accordingly. These results are in good agreement with previous inference from etch rate measurements and model simulations [13, 51].

For oxygen plasmas, in addition to the kinetic energy contributions from fast atomic and molecular oxygen neutrals, heat can be released from the recombination of atomic oxygen fast neutrals on the sensor surface. We can assume that the composition ratio of  $O$  and  $O_2$  fast neutrals is the same as the corresponding ionic ratio,

$\eta = O_2^+/O^+$ , in the source region. We calculated the value using a global average model developed by Lieberman and his co-workers [15]. Taking this additional heat contribution into account, we can write an expression containing the flux-weighted average velocity of the neutral O atoms:

$$\frac{F}{Q} = \frac{Am_{O_2}\bar{v}_o(\frac{1.414\eta+1}{2(\eta+1)})}{\frac{1}{4}m_{O_2}\bar{v}_O^2 + \delta\frac{E_{rec}}{2(\eta+1)}} \quad (6.19)$$

where  $\delta$  is the surface recombination coefficient for atomic oxygen atoms on the sensor surface. Assuming a surface recombination coefficient of 1 at the sensor will yield an estimate of the lower bound for the neutral flux. Fig 6.3 shows the oxygen neutral flux and energy estimated in this way. The neutral energy value, around 6 eV, is close to what is expected from our previous Monte-Carlo modeling at bias levels of -10 to -15 V [13].

The oxygen neutral flux increases with the rf power. Fig. 6.4 shows argon neutral energy and flux as a function of the reflector bias. As seen in previous work [118] with such a biased downstream boundary, operation at zero reflector bias should be avoided since a negative voltage (5-10 volts) is required to establish stable reflex electron confinement for  $T_e \sim 5\text{ev}$ . Discounting this “special” point, we see that the flux has a nearly constant value of  $\sim 1.4 \times 10^{15} \text{cm}^{-2}\text{s}^{-1}$  with reflector bias changes. The fast neutral energy is a roughly linear function of the  $V_b - V_p$ . The earlier Monte-Carlo model of Nichols’s thesis [13] and presented by Nichols and Manos [14] discussed the transport of reflected neutrals in detail.

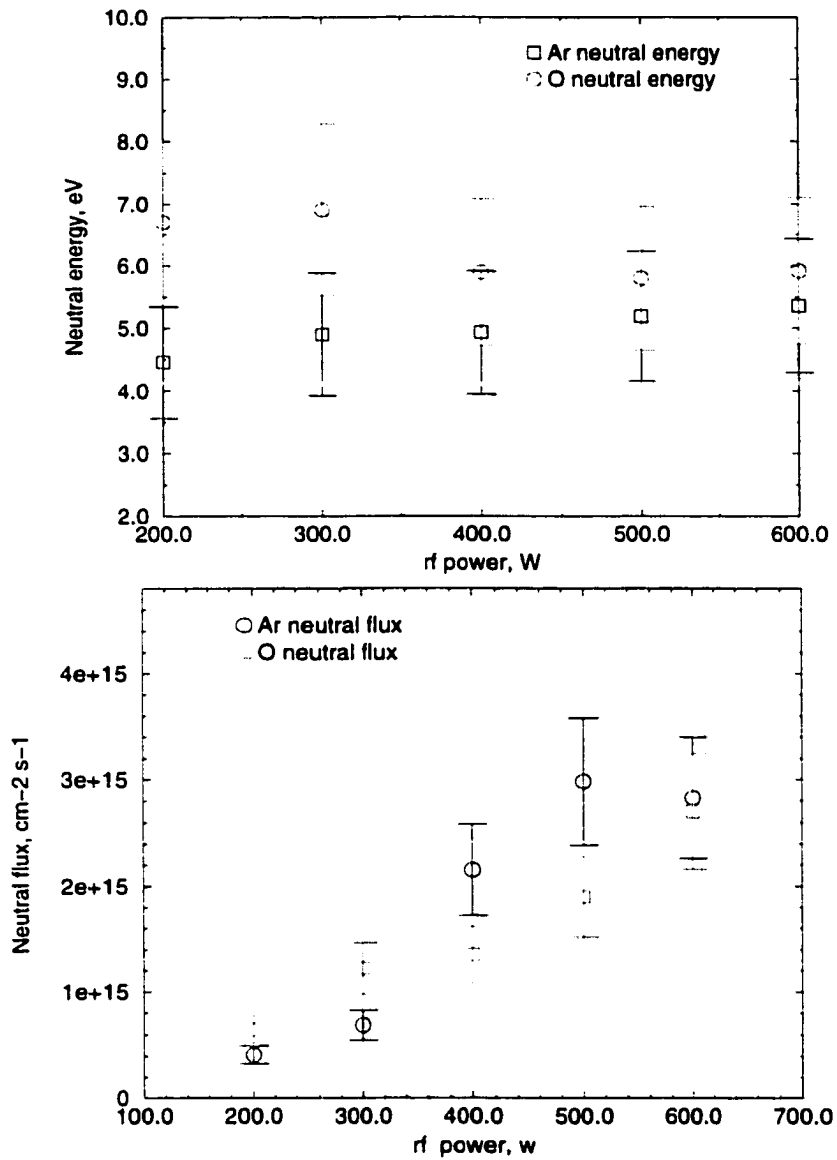


Figure 6.3: Neutral flux and energy measurement as a function of the rf power for pure Ar and  $O_2$  plasmas. (Ar plasma: 4.54 mTorr;  $O_2$  plasma: 5.6 mTorr, the reflector bias: -25 V)

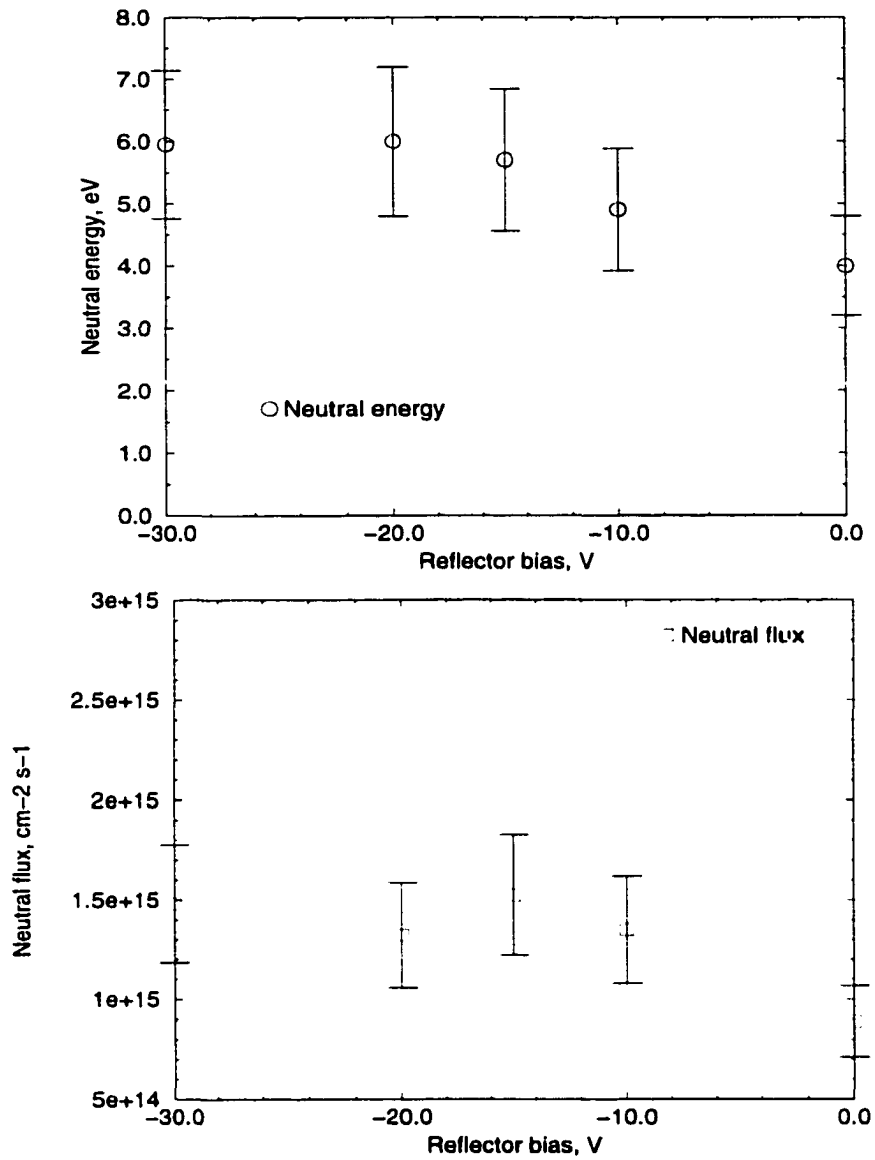


Figure 6.4: Ar neutral energy and flux as a function of the reflector bias in Ar plasmas ( 500 W, 5.77mTorr, 8.75 sccm)

Our observed energy range 3~6 eV is in excellent agreement with those calculations. The reflected neutral flux measured as the rf power and reflector bias are changed is observed to be proportional to the ion flux collected by the reflector plate. The neutral flux density in the downstream region is 0.5% to 1% of the ion flux density at the reflector plate. From the neutral flux and energy measurements, we can use the etch yield data of Cross *et al.* [107] to calculate stripping rates. Fig. 6.6 shows these calculated stripping rates compared to our previous experimental rates obtained using coated quartz crystals in a micro-balance.

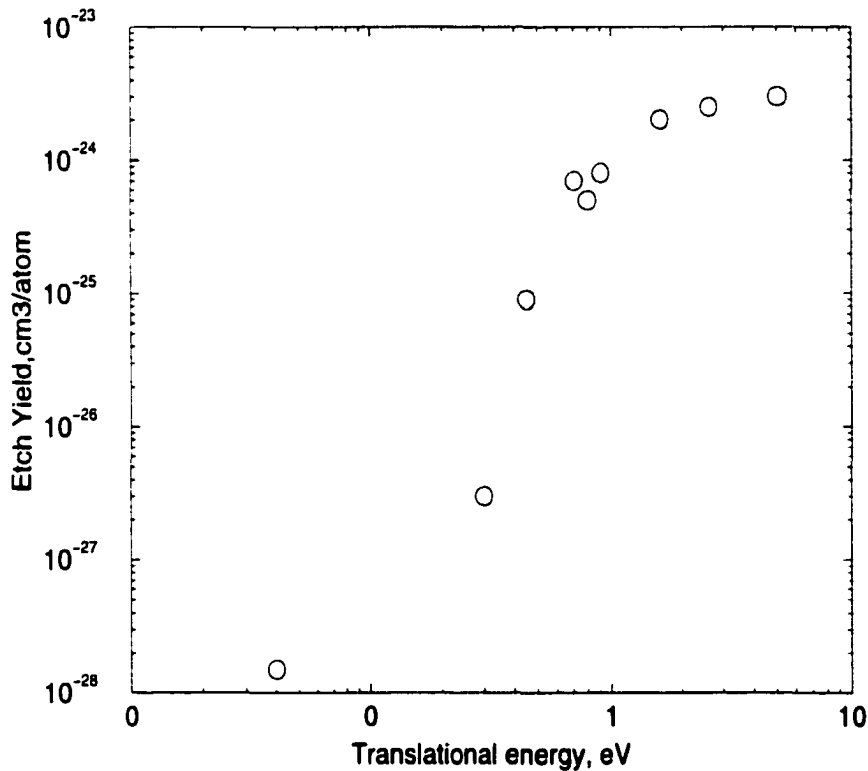


Figure 6.5: Etch yield as a function of neutral translational energy (reproduced with permission from J.Cross[107])

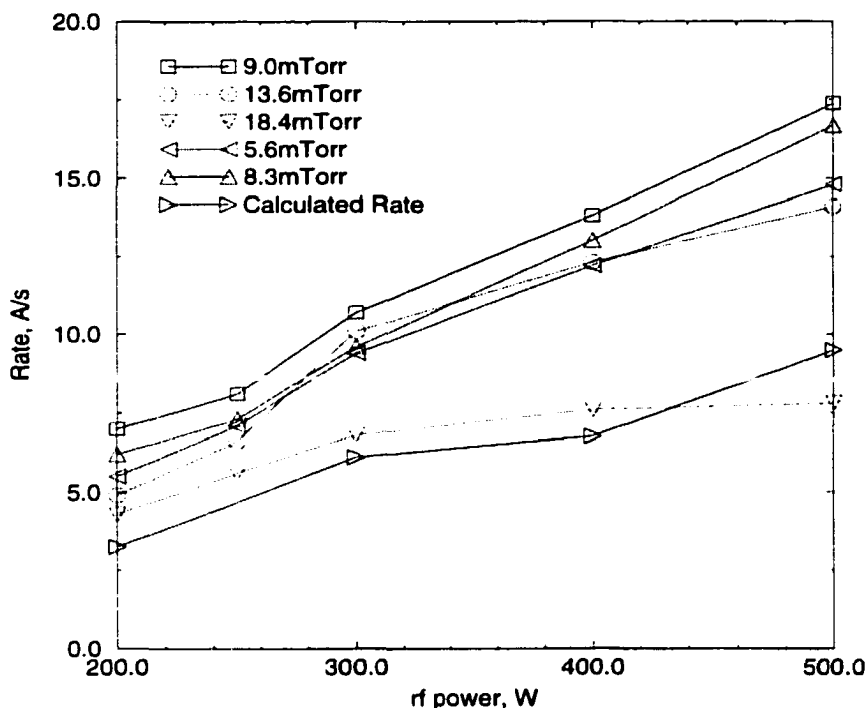


Figure 6.6: Comparison of the stripping rates as a function of the rf power. (stripping rates at different pressures were measured under following experimental conditions: the reflector bias: -13.4 V; Ar:3.66 sccm;  $O_2$ : 8.33sccm)

The observed rate is approximately twice as high as the calculated rate for any value of the rf power. The fact that the calculated rate is lower than experimental is consistent with the fact that our oxygen flux estimate must be a lower bound to the actual flux for the reasons discussed in detail above. The correct value of the O atom recombination coefficient could be less than 1 under these conditions. Another possibility is that the neutral energy reflection coefficient is varying with varying oxygen coverage of the reflector plate. It is also quite possible that the experimental rates are enhanced by as much as a factor of two by deep UV flux.



## 6.5 Summary

We have performed both the neutral energy and flux measurement of the surface reflection neutral energy sources. This technique combines the momentum and heat flux measurements together. Measurements show that the neutral flux is on the order of  $10^{15} \text{cm}^{-2} \text{s}^{-1}$  and neutral energy is tunable over a certain range (3~6 eV). The neutral flux increases with rf power. The measured neutral energy increases less than linearly with reflector bias. The etch rates calculated from the measured neutral flux and experimental rates are in good agreement.

# Chapter 7

## Process damage assessment of a low energy inductively coupled plasma-based neutral source

### 7.1 Introduction

High density plasma sources induce a certain amount of damage. Generic process-induced damage includes the degradation of integrity of dielectric layers [119,120], structural damage, contamination [121], and others. This process damage depends strongly on the process type and the feature geometry [122]. Current damage studies center on the damage assessment in etching and post-etch ashing or cleaning processes using a variety of sensors, such as CHARM-2 [123], SPORT [124, 125], M-NOS transistors, contact or non-contact surface potential difference [126], and micro-electro-mechanical cantilever structures [127]. Experimental results [119, 120, 128]

and computational simulations [129, 130] indicate that in these processes, damage is mainly caused by the current stress from plasma non-uniformity [131, 132] and by direct particle bombardment during plasma-wafer interactions. Photo-resist residue on the surface features [4, 133, 134] in post-etch ashing processes also might be a major source of damage. The current stress damage appears to be less important when the device features are scaled down to  $0.5\mu\text{m}$  where the topographic-dependent electron shading damage (ESD) [135, 136] and VUV radiation [137] damage become the main concern. However, as the features further scale down towards  $0.1\mu\text{m}$  and below, all of these sources of damage [138, 139] are expected to become very serious.

Many plasma source and process modifications to reduce process damage have been reported [140]. These include choosing optimal dc bias [141], reducing the production of ions, uv exposure [142, 143], and removing damage by post-treatments [144–146]. Experiments [147, 148] also indicate that pulsing (ICP and ECR) plasmas can improve the etch selectivity and greatly reduce ESD damage. Complete elimination of the electron shading damage and other damage is possible, at least in principle, using neutral beams instead of plasma treatments for selected processes [103]. Three major types of neutral sources have been examined [12, 13, 104, 105]. Early work on  $1\mu\text{m}$  features in our group [106] showed that in a wave-based, small-area, low-energy reflection neutral beam source, UV photons contributed almost all of the damage for  $\text{O}_2$  photo-resist patterning and that this damage was annealable. Goeckner *et al.* [149] showed that the residual charged particle flux could be made at least several orders of magnitude smaller than the hyper-thermal neutral flux in a multiple reflection neutral stream. We have described a large-area transformer coupled plasma

(TCP)-based neutral source and the use of this neutral source for photo-resist cleaning applications [14,51]. In this chapter, we report quantitatively damage studies using this large area TCP-based surface reflection neutralization source to examine direct plasma exposure damage and neutral stream photo-resist ashing damage of metal-oxide-semiconductor (MOS) capacitors. The process damage was characterized as a function of the reflector bias(neutral energy), gas composition, and rf power. The damage caused by direct exposure to the plasma in cw and pulsed mode was also studied for comparison.

## **7.2 Experiment**

### **7.2.1 CW, Pulsed ICP plasma setup and Surface reflection neutralization source**

A schematic drawing of the apparatus and detail descriptions are shown in Fig. 5.1. The collimator contains magnets and biasable grids to filter out charged particles in the downstream zone and allows for the addition of uv light filters. This permits us to de-convolve the relative contribution of neutrals, charged particles, and UV light to the device damage.

### **7.2.2 Damage Measurement**

We used standard gate-oxide integrity (GOI) monitor wafers supplied by Sandia National Labs for the damage evaluation. These wafers have three different size (500 $\mu\text{m}$ ,1000 $\mu\text{m}$ , and 3500 $\mu\text{m}$  diameter) metal-oxide-semiconductor (MOS) dot ca-

capacitors, consisting of the p-type, B-doped silicon substrate, either 100 angstroms or 1000 angstroms of  $SiO_2$  dielectric, and Al top electrode dots. The backs of the wafers were stripped of oxides and diffused with Al to allow back contact. Prior to exposure in our apparatus, the wafers were annealed in forming gas,  $N_2 + H_2$ , at 350°C for 30 minutes.

Exposures in our neutral streams were studied with two classes of trials. In the first class, samples were exposed to the neutral flux with different reflector bias, exposure time, rf power, and gas composition. To distinguish uv photon, ion-, and electron-induced damage from the fast-neutral induced damage, an  $MgF_2$  window and the collimator, with and without the  $MgF_2$  window, were placed in front of samples. The  $MgF_2$  window permits vacuum uv light to strike the sample, but stops all particle bombardment. The reflector plate current under these experiment conditions was also collected. In the second class of trials, samples were coated with PMMA, baked in an oven at 98°C for one hour, and exposed to the neutral stream for very long times (over 3 hours). In both classes of experiments, we used both cw plasmas and pulsed plasmas having the same time-average rf power. Discharge gas composition was varied in both classes of experiments. The flux of ions striking the reflector was directly measured as the “reflector current”, which is directly proportional to the resulting neutral beam intensity.

Simultaneous quasi-static and high frequency CV measurements were carried out on a Keithley Model 82 system. I-V measurements were carried out using the same system. Post-exposure samples were examined by a variety of techniques, including atomic force microscopy (AFM) and X-ray photoelectron spectroscopy (XPS).

## 7.3 Results

### 7.3.1 Class 1: Neutral Damage Measurements without PM-MA overlayer

Fig. 7.1 shows quasi-static CV results for the as-received sample and for samples exposed with and without the collimator. Quasi-static CV results for samples exposed with and without the  $MgF_2$  window are shown in Fig. 7.2. The high-frequency

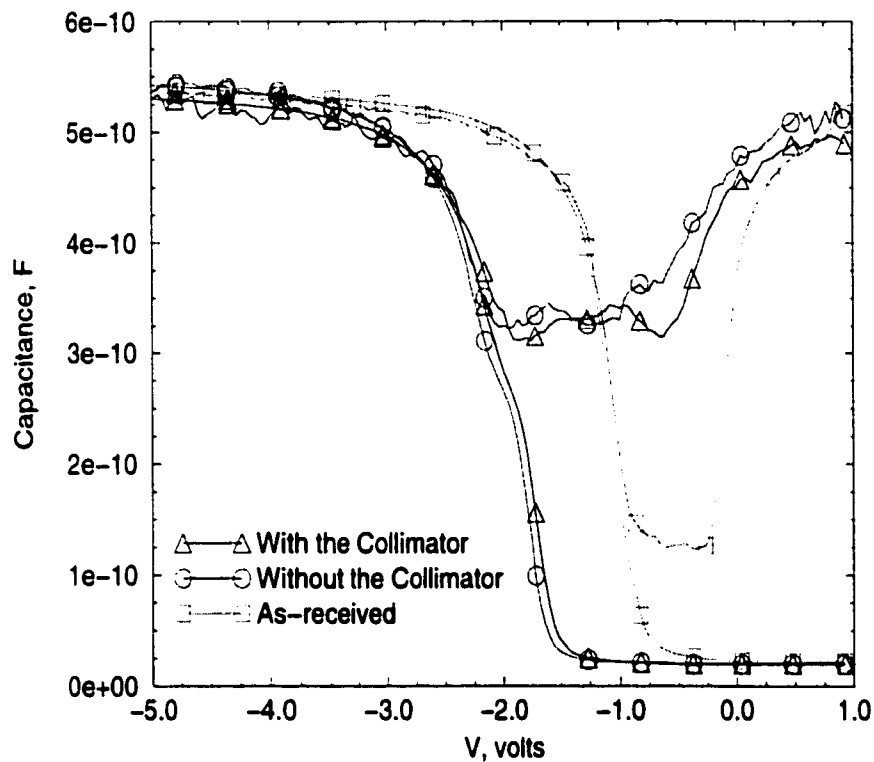


Figure 7.1: Quasi-static and high frequency CV results of neutral stream processing with and without the collimator. (a) As-received, (b) Sample with the collimator, (c) Sample without the collimator (130 w,  $O_2$ ,  $V_b = -20$  V).

CV curves of the two exposed samples in Fig. 7.2 are shifted toward the negative gate bias direction after the neutral stream exposure. These shifts allow us to calculate the increased density of positive charges in the oxide, see below. With the collimator in place, Fig. 7.1 shows that the shift becomes less pronounced. The two sets of CV traces in Fig. 7.2 for samples exposed with and without the  $MgF_2$  window show no relative shifts. As discussed below, with the  $MgF_2$  window in place, only the UV photons with energy less than  $\sim 11$  eV reach the samples to contribute to the damage.

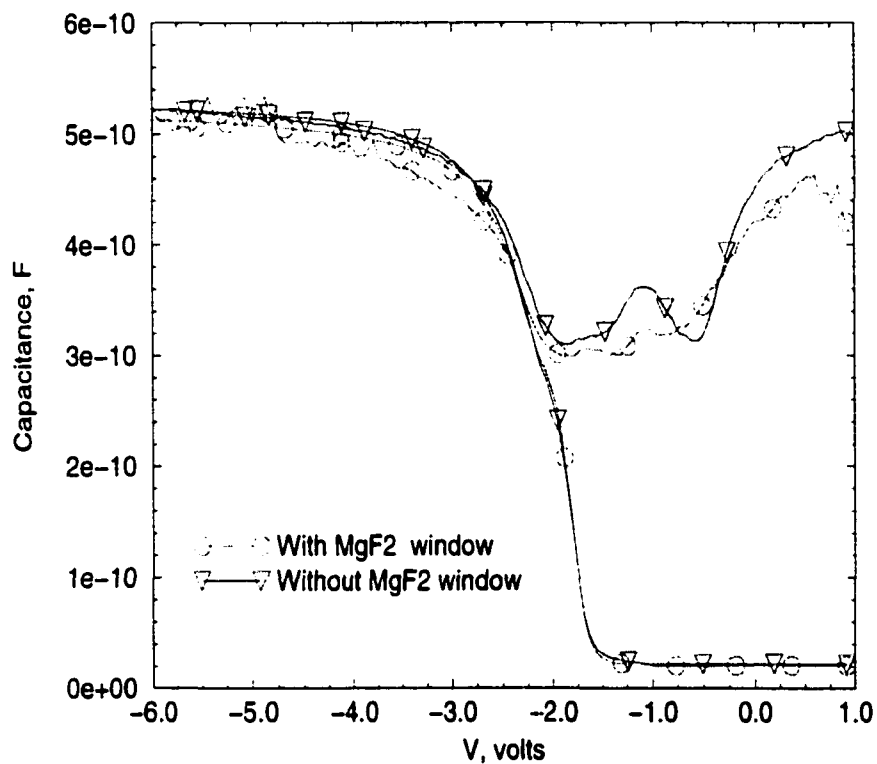


Figure 7.2: Quasi-static and high frequency CV results of exposure to neutral streams with and without  $MgF_2$  window (8.9mTorr,  $O_2$ ,  $V_b = -20V$ , 5 min.)

Fig. 7.3 shows the dependence of the observed flatband voltage shift, a measure

of damage described below, as the reflector bias is changed. The figure also shows

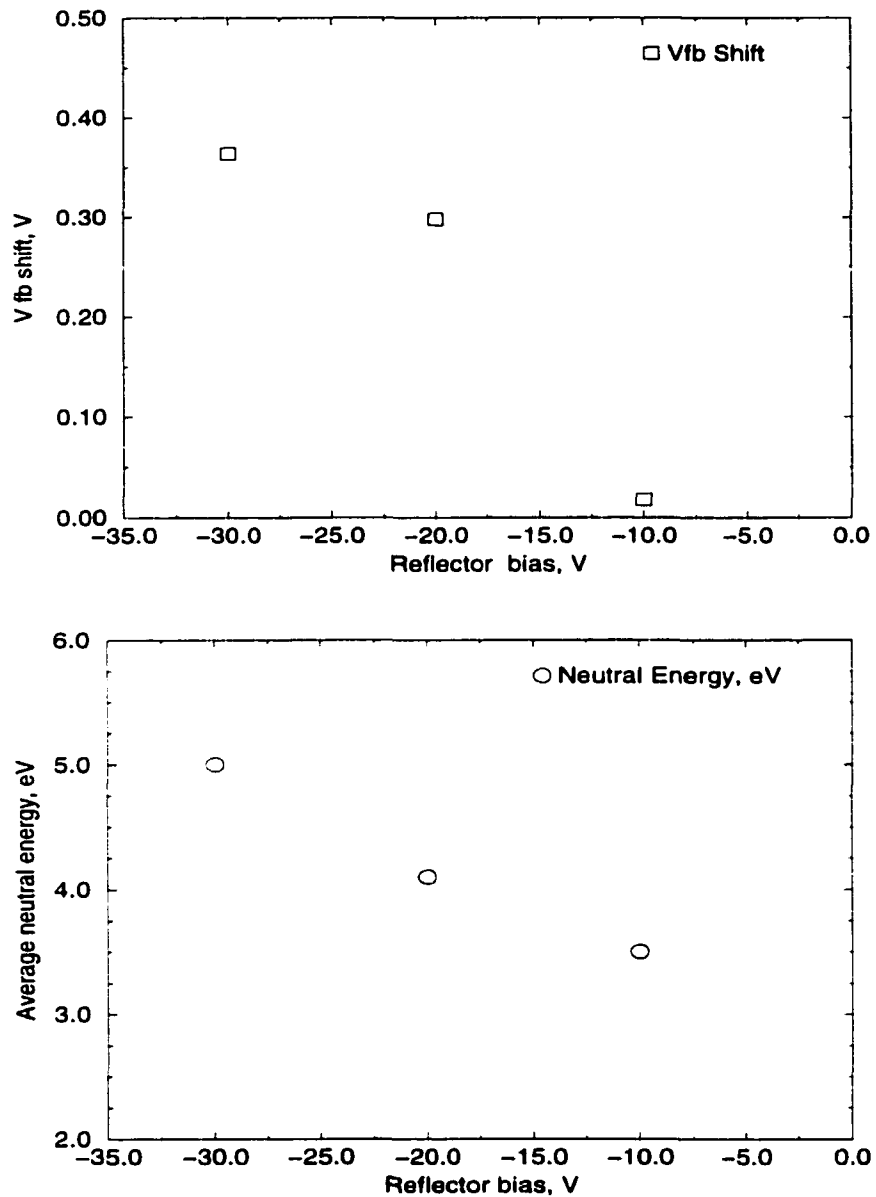


Figure 7.3: The flatband voltage shift and average fast neutral energy as a function of the reflector bias in neutral stream. (8.40mTorr,  $O_2$ , 130 w, 5min)



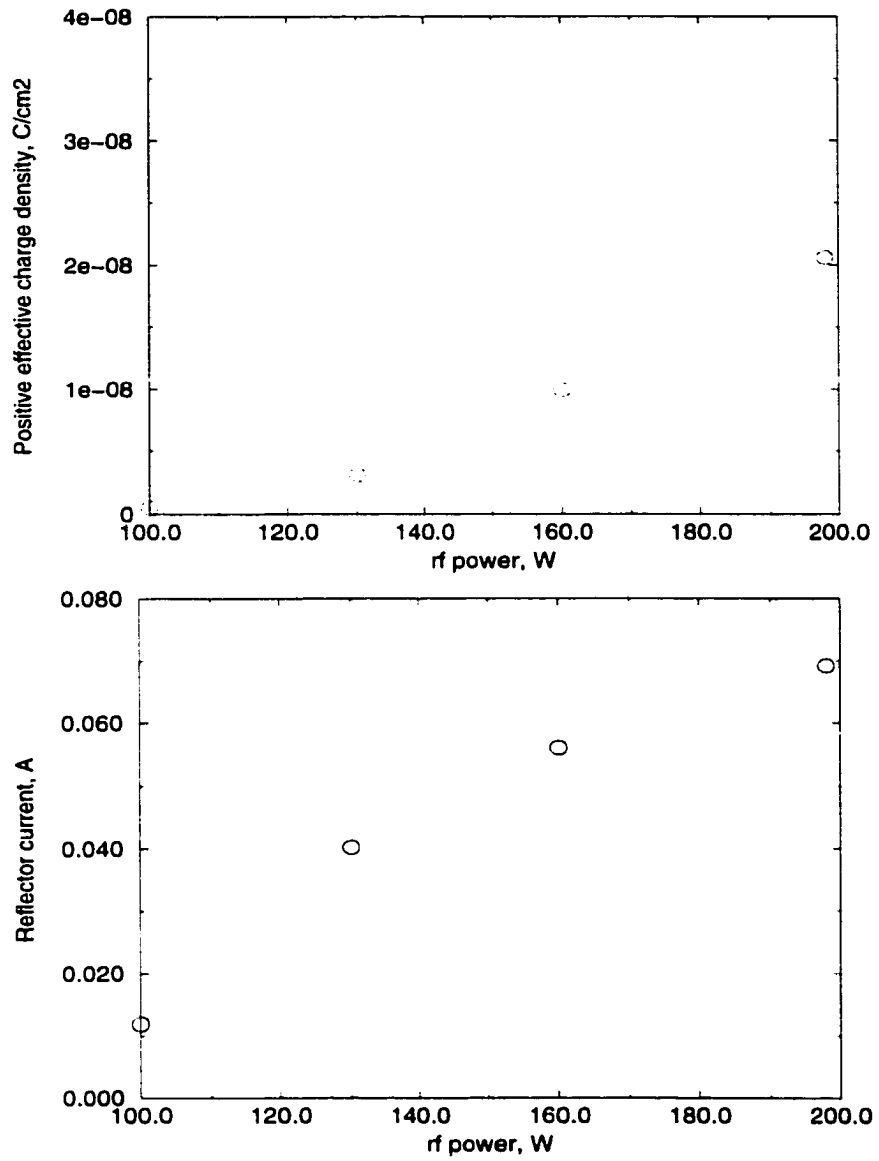


Figure 7.4: The positive effective charge increase and reflector current as a function of the rf power. ( $O_2$ ,  $V_{reflector} = -20$  V, 8.90mTorr)

the calculated average reflected neutral energy reaching the process zone, taking into account the velocity moderating collisions between the reflected neutrals and the background. Fig. 7.4 shows the reflector current as the rf power increases; the increase correlates to an increase in the neutral flux. To study the variation of damage with location in the process region we identified several locations at which to make damage measurements on the wafer. These measurement points are shown in Fig. 7.5.

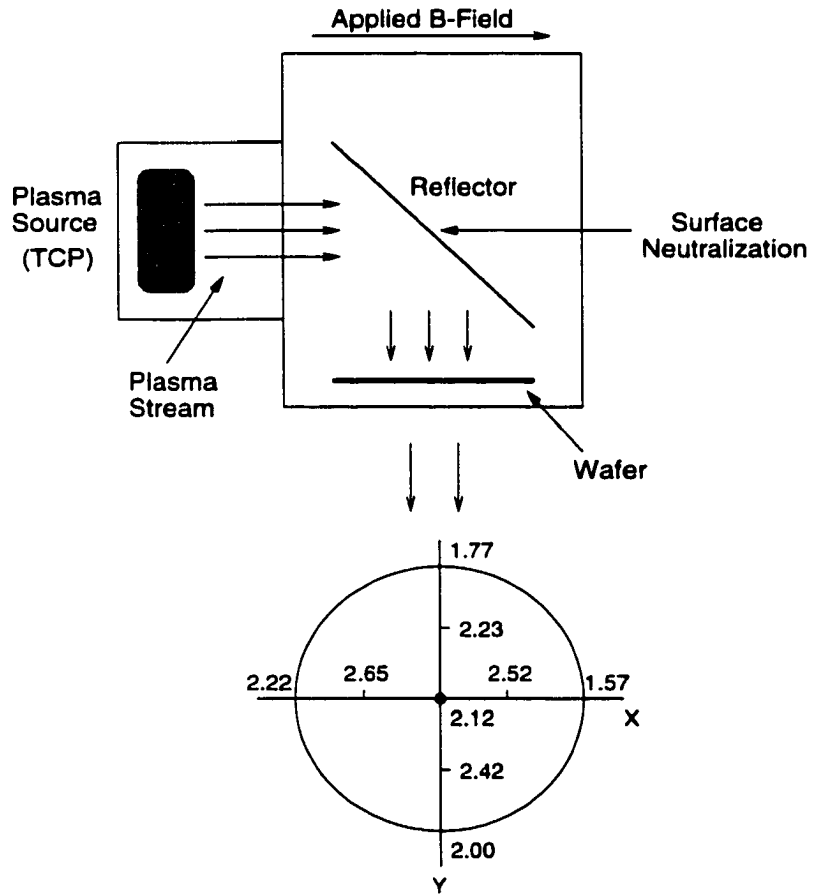


Figure 7.5: Numerical values of positive charge density ( $\times 10^{-7} C/cm^3$ ) increase at different locations after neutral processing (130 w, bias:-20 V, 5min, note: this data has not been corrected for the contribution from UV photons)

The correlation of damage with composition of the plasma was also studied. Fig. 7.6 shows C-V measurements at the wafer center for varying the ratio of  $Ar/O_2$  in the plasma.

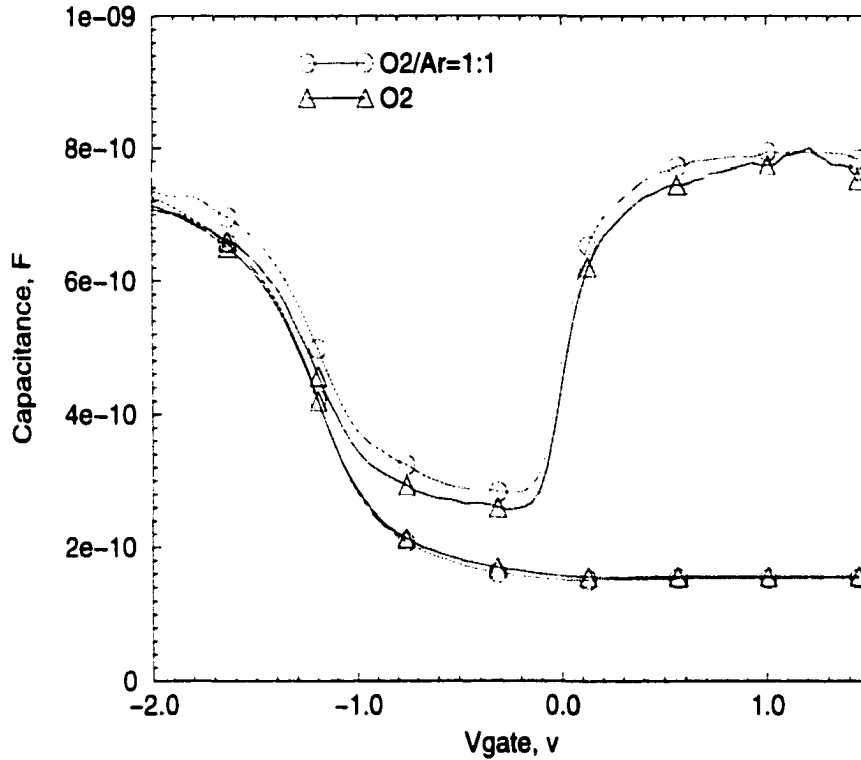


Figure 7.6: Quasi-static and high frequency CV results of the MOS samples exposed to neutral streams. (7.32mTorr,130 W,bias:-25V,(a) $O_2/Ar = 1 : 1$ , (b) $O_2$ )

### 7.3.2 Class 2: Damage with PMMA overlayer

Similar studies were performed on wafers which were given a  $\sim 1 \mu m$  PMMA baked overcoat. In addition, these samples were exposed for periods intended to represent overetches of several hundred to one thousand percent. Table 7.1 shows ashing process damage by neutral, cw, and pulsed plasma processes.

<i>Type</i>	<i>Neutral Processes</i>	<i>CW Plasma Processes</i>	<i>Pulsed Plasma Processes</i>		
Experimental conditions	$O_2$ 7.44 sccm, 130 W	$O_2$ 7.44 sccm, 65 W	878Hz 65 W	1000Hz 65 W	5000Hz 65 W
Time	3h	30 min	30min	30min	30min
$\Delta Q_{eff}, c/cm^2$	$2.2 \times 10^{-7}$	$1.0 \times 10^{-7}$	$1.2 \times 10^{-7}$	$3.9 \times 10^{-7}$	$2.3 \times 10^{-7}$

Table 7.1: Comparison of the photo-resist ashing process damage by different plasma processes

## 7.4 Discussion

### 7.4.1 Class 1

All plasma components, such as electrons [150], ions [151], UV photons [152], and neutrals [153, 154], are capable of inducing process damage. In a non-ideal process, we expect to observe a variety of sources of damage such as Fowler-Nordheim current stress damage between the gate electrode and *Si* substrate and vacuum UV radiation damage. As samples are placed out of the plasma source zone and the collimator is placed in the downstream region, effectively preventing charged particles from reaching the samples in our configuration, current stress damage can be minimized. But damage by uv photons still remains a concern. These high energy uv photons can create electron-hole pairs in the gate oxide. If the vuv photon energy is high enough, photoelectrons may be ejected from the surface, causing surface charge build-up. Photons with energies lower than the  $SiO_2$  energy gap but greater than 4.2 eV (the height of minimum energy barrier between the Si substrate valence band and oxide conduction band) can cause the injection of the stress current from *Si* into

the thin gate oxide. Charge build up can cause holes to drift toward the  $SiO_2/Si$  interface where they either appear as trapped positive charges or release energy on recombinations with electrons, breaking chemical bonds and creating additional interface trapping sites [155]. The measured values of capacitance and C-V shifts can be used to arrive at quantitative estimates of the oxide damage.

The effective positive charge in  $SiO_2$  is calculated from

$$Q_{eff} = C_{ox} * (W_{ms} - V_{fb})/A, \quad (7.1)$$

$$W_{ms} = W_m - (W_s + E_{bg}/2 - \phi), \quad (7.2)$$

where  $W_m$  and  $W_s$  are work functions of the metal and the semiconductor material respectively,  $E_{bg}$  is the band gap.  $\phi$  is the bulk potential, and  $C_{ox}$  is the measured oxide capacitance. The interface trap density is calculated from :

$$D_{it} = (1/(1/C_q - 1/C_{ox})) - (1/(1/C_h - 1/C_{ox}))/A * e, \quad (7.3)$$

where A is the electrode area.  $C_q$  and  $C_h$  are the quasi-static capacitance and high frequency capacitance respectively. Using the data of Fig.7.2, these calculations show that uv photons contribute at least over 83 percent of the positive charge increase in the oxide and at least 74 percent of interface trap density increase overall.

We can use the calculated interfacial positive charge to estimate the absolute vuv radiation intensity. Generally, there are two steps involved in interfacial positive charge generation in  $SiO_2$ : hole generation and hole transport and capture at  $Si/SiO_2$  interface. The experimental interfacial generation rate takes both processes into consideration [156]. The interfacial positive charge generation rate (charge/photon) in a

$SiO_2$  specimen, irradiated by vuv photons having energies between 8.8 eV to 22 eV has been estimated to be in the range of  $10^{-3}$  to  $10^{-2}$  [156] with zero applied electric field. The corresponding interfacial charge generation rate under an applied electric field can be calculated from the Smoluchowski equation [155, 157].

$$\frac{\partial P(r, t)}{\partial t} = D\{\nabla^2 P(r, t) - (\frac{e}{kT}) \cdot [\epsilon P(r, t)]\}, \quad (7.4)$$

where  $P(r, t)$  is the probability density of forming a single electron about a single positive charge. The generation rate under applied fields was found to be a higher, but still less than 0.1 [158]. For low pressure argon and oxygen plasmas, the dominant atomic emission lines have photon energy of around 10 ev. From our measured positive charge increase, we can infer a vuv photon flux of about  $1. \times 10^{10} cm^{-2} s^{-1}$ . This value is much lower than values reported by other studies, for example, those of Woodworth *et al.* [159] because of the extreme “remote plasma” aspect of our geometry.

Assuming reflection of O atoms from a polycrystalline tungsten plate hold at a bias between -10 to -30 volts, nascent fast neutrals are expected to carry kinetic energies of  $0.3 \sim 0.5(V_p - V_{bias})$  eV, only modestly larger than 8.8 eV ( $SiO_2$  band gap). A fast neutral generates fewer electron-hole pairs than does an ion with the same translational energy. This is because an ion must also dump the energy associated with neutralization within a few Å of its point of impact. Nevertheless, uv photons and fast neutrals in a neutral source can contribute to the areal dependent current stress damage of dielectric layers and to the edge-dependent damage on the electrode edge.

We expect then to see an increase of these sources of damage as the flux of photons or neutrals increases. We note again that in Fig. 7.3 and Fig. 7.4, the con-

tribution from uv photons has been subtracted from the total changes. The flatband voltage shift increases dramatically as the reflector bias changes from -10 to -30 V even though the corresponding reflected neutral energy reaching the process zone increases only from about 3 eV to 5 eV. As the reflector bias is changed from -10 to -30 volts, the vuv radiation intensity does not change much. The observed change in flatband voltage is therefore contributed by the increasing neutral flux.

We assume that the process damage can be characterized by the positive charge increase,  $\Delta Q_{eff}$ . Then damage will be a function of the generation yield, discussed above, and the irradiation dose:

$$\Delta Q_{eff} = \gamma_{fast\ neutral} * \Phi_{fast\ neutral} + \gamma_{uv\ photons} * \Phi_{uv\ photons}, \quad (7.5)$$

where  $\gamma$  represents the positive charge generation yield for neutrals and photons and  $\Phi$  is the total irradiation dose. After subtraction of the uv photon contribution, our fast neutral process damage data corresponds to:

$$\Delta Q'_{eff} = \gamma_{fast\ neutrals} * \Phi_{fast\ neutrals}, \quad (7.6)$$

and the flatband voltage shift observed is

$$\Delta V_{fb} = \frac{C_{ox} \Delta Q'_{eff}}{A}. \quad (7.7)$$

Although the neutral energy increase associated with changing the reflector bias is small, it is still capable of causing an increase of the positive charge generation yield. A substantial initial increase is observed for increasing both the fast neutral energy (slowly) and the neutral flux (rapidly) from 0 to -20 volts of reflector bias. The flux then saturates, yielding a slow increase in the damage as voltage changes further.

This damage increase in MOS capacitors may be associated with the dependence of the generation yield on the neutral energy.

The above Eqn. 7.6 is confirmed by the results of increased rf power. According to a global average plasma model (see Chapter 4) for ICP plasmas, the plasma density in our source region increases linearly with the rf power, while the electron temperature (and thus the plasma potential) remains nearly constant. This causes an increase of the reflector plate current thereby increasing the neutral flux without changing the neutral energy in the process region [160]. This is consistent, after correction of vuv damage, with the positive charge increase, seen in Fig. 7.4, as the rf power increases.

Earlier simulations of the neutral flux, energy, and angles of incidence as functions of the location on the wafer suggested that peak flux for a flat 45-50 degree reflector plate is not on the center of the wafer. The results shown in Fig 7.5 are in excellent agreement with these calculations. Although the etch rate has been found to depend on composition in earlier studies, the lack of dependence of damage seen in Fig. 7.6, is also consistent with the above interpretation.

#### **7.4.2 Class 2**

Table 7.1 [161] shows that the worst process damage occurs when the plasma is pulsed at 1000Hz frequency. Time-average plasma density measurements and the model of Chapter 3 and 4 show that the average plasma density is highest at a pulse frequency of 1000Hz. It appears that there is a damage contribution that depends mainly on the integrated flux of particles striking the oxides. Less damage



is found in pulsed plasmas at other frequencies with the same time-average power. Post exposure analysis of these samples indicates that no PMMA residue remains on the surface of the MOS capacitors exposed either to the neutral stream or exposed directly to the 1000Hz pulsed plasma. However, there is a small amount of PMMA residue on the devices exposed to the pulsed plasma at 878Hz and 5000Hz and for the cw case. It is likely that damage only starts to accumulate after the regions of PMMA are completely removed allowing the Al electrode to be exposed to the process environment. For fast neutral processing, the damage shows no dependence on the gas composition (Fig. 7.6). In contrast, pulsed plasma process damage does depend on discharge gas composition [162]. The reason, while not entirely clear, may depend on differences in plasma chemistry as well as radiative excitations in the pulsed cases, where initial populations of hot electrons may be important [163] in pulsed plasmas.

## 7.5 Summary

This chapter has presented a damage evaluation of fast neutral processes based on a surface reflection neutralization ICP based source. The results show that most of the process damage is caused by the uv photons. The much smaller amount of fast-neutral induced process damage increases with the reflector bias and rf power in neutral processing. Compared to both pulsed plasmas and to cw plasmas with same time average power, neutral processes induce far less damage. This improved behavior is attributed to the absence of ions and electrons during the processes.

# Chapter 8

## Conclusion

### 8.1 Summary

In this work, the scaling and the operation of a surface reflection neutralization method for the semiconductor processing have been examined. Experiments show that this method can provide enough fast neutrals for cleaning application. The neutral beam characterization shows that the neutral flux value is about  $10^{15} \text{cm}^{-2} \text{s}^{-1}$  and the neutral energy is tunable about 3~6 eV. Systematic Langmuir probe and optical emission studies indicate a mode transition from CCP -ICP mode. The OES studies also show that there is no visible change in the OES spectra with changing reflector bias. Damage assessment with different processes, such as cw plasma process, pulsed plasma processes, and low energy neutral processes have been performed with MOS capacitors. Results show that the neutral process damage is a function of reflector bias and rf power. The low energy neutral processing induces much less damage than pulsed plasma. Most of the damage is caused by uv photons. Another type

of low damage process-pulsed processes was investigated in this dissertation. Double probe and corresponding data analysis routine are developed to reliably characterize the plasma transients in a pulsed Ar discharge. The results shows that by changing the pulse duty cycle and pulse frequency, it is possible to optimize the time average plasma density and electron temperature.

A global average simulation model is performed to simulate the pulse discharge. The simulation demonstrates that by pulsing the plasma at certain frequencies, a high average density can be achieved. The simulation yields good agreement with data from CW and rf pulsed operation of our source and provides us with a very important design tools for future optimization of reflection sources.

## 8.2 Future Work

Future work are suggested in following areas:

- New application development: so far, most work with this source are related with ashing or etching application. Using this neutral beam to grow charge-free films will also be very promising. Etching application using  $CF_4$  gas will also be useful to understand the etching mechanism.
- Reflection efficiency studies: As we discovered in these studies, at a highly negative reflector bias, the energy reflection efficiency seems to be lower than the value at a lower reflector bias. Further studies on degradation or recombination on the reflector are needed to understand the mechanism.
- Pulsed plasma characterization : double probe set up and data analysis can be used to investigate pulsed electro-negative discharges, such as oxygen.

- Simulation model : the global average simulation model can be further improved to include more particle species such as  $O_3^-$  and more loss and generation channels. More studies should also be performed to understand other discharges such as  $O_2$ ,  $CF_4$  and  $CHF_3$ .

- Technical improvement: the accuracy of torsion balance measurement can be further improved. Modification of the damping system is required to reduce measurement time. A better way to measure the resolution of angle measurements will also greatly improve the sensitivity of torsion balance.

# Bibliography

- [1] R. Behrisch, G. Maderlechner, B. M. .U. Scherzer, and M. T. Robinson. The sputtering mechanism for low energy light ions. *Applied Physics*, 18:391, 1979.
- [2] J. C. Arnold and H. H. Sawin. Charging of pattern features during plasma etching. *J. Appl. Phys.*, 70:5314, 1991.
- [3] C. T. Gabriel and J. P. McVittie. How plasma etching damages thin gate oxides. *Solid State Technol.*, 35:81, 1992.
- [4] H. Shin, N. Jha, X. Qian, G. W. Hills, and C. Hu. Plasma etching charge-up damage to thin oxides. *Solid State Technol.*, 36:29, 1993.
- [5] K. Yonekura, M. Kiritani, S. Sakamori, and T. Yokoi. Effects of charge build-up of underlying layer by high aspect ratio etching. *Jpn J. Appl. Phys.*, 37:2314–2320, 1998.
- [6] T. Mizutani and T. Yunogami. Neutral beam assisted etching of  $SiO_2$ . *Jpn J. Appl. Phys.*, 29:2220, 1990.
- [7] Q. Han, I. L. Berry, J. Shi, T. W. Mountsier, and M.A.Plano. Enabling low-

- $\kappa$  material integration through low-ion plasma dry strip process. *Micro*, Oct:51, 1999.
- [8] C. Boitnott. Downstream plasma processing: Considerations for selective etch and other processes. *Solid State Technology*, Oct:51, 1994.
- [9] D. M. Manos, J. E. Stevens, and J.L.Cecchi. *SEMATECH report No.93071752A-XFR*. Sematech, TX, 1993.
- [10] R. M. Motley, D. M. Manos, W. D. Langer, and S. A. Langer. Neutral particle surface alteration. *U.S.Patent*, (4,662,977), 1995.
- [11] J. W. Cuthbertson. *Reflection of Plasma Ions from Metals*. PhD thesis, Princeton University, Princeton, NJ, 1991.
- [12] M. J. Goecker, T. K. Bennett, and S. A. Cohen. A source of hyperthermal neutrals for materials processing. *Applied Physics Letter*, 17:980, 1997.
- [13] C. A. Nichols and D. M. Manos. Simulation of a surface-reflection neutral stream source. *J. Appl. Phys.*, 80:2643, 1996.
- [14] C. A. Nichols. *Surface Reflection Hyperthermal Neutral Stream Source*. PhD thesis, The College of William Mary, Williamsburg, VA, 1996.
- [15] M. A. Lieberman and A. J. Lichtenberg. *Principles of Plasma Discharges and Materials Processing*. Wiley, New York, 1994.
- [16] M. A. Lieberman and R. A. Gottscho. *Design of high density plasma sources for materials processing*. Edited by M.H.Francombe and J.L.Vossen, Physics of Thin Films, Vol 18, Academic Press, San Diego, 1994.

- [17] D. M. Manos and D. L. Flamm. *An Introduction to Plasma Etching*(New York: Academic), chapter 4. Academic, New York, 1989.
- [18] D. A. Hope, T. I. Cox, and V. G. I. Deshmukh. Optical emission spectroscopy of reactive plasma: a method for correlating emission intensities to a reactive particle. *Vacuum*, 37:275, 1987.
- [19] M. V. Malyshev. *Advanced plasma diagnostics for plasma processing*. PhD thesis, Princeton University, Princeton, NJ, 1997.
- [20] J. W. Coburn and M. Chen. Optical emission spectroscopy of reactive plasma: a method for correlating emission intensities to reactive particle. *J. Appl. Phys.*, 51:3134, 1980.
- [21] R. d. Agostino, V. Colaprico, and F. Cramarossa. The use of actinometer gases in optical density diagnostics of plasma etching mixtures  $SF_6 - O_2$ . *Plasma Chem. Plasma Process*, 1:365, 1981.
- [22] V. M. Donnelly, D. L. Flamm, and G. Collins. Laser diagnostics of plasma etching: measurement of  $Cl_2$  in a chlorine discharge. *J. Vac. Sci. Technol. A*, 21:817, 1982.
- [23] M. V. Malyshev and V. M. Donnelly. Determination of electron temperatures in plasmas by multiple rare gas optical emission, and implications for advanced actinometry. *J. Vac. Sci. Technol. A*, 15:550, 1997.
- [24] CH. Steinbruchel, B. J. Curtis, H. W. Lehmann, and R. Widmer. Diagnostics of low-pressure oxygen rf plasmas and the mechanism for polymer etching:

- a comparison of reactive sputter etching and magnetron sputter etching. *IEEE Trans. Plasma Sci.*, PS-14:137, 1986.
- [25] K. L. Junck and W. D. Getty. Comparison of *Ar* electron-cyclotron-resonance plasmas in three magnetic field configurations. I. electron temperature and plasma density. *J. Vac. Sci. Technol. A*, 12:2767, 1994.
- [26] A. Granier, D. Chemreau, K. Henda, R. Safari, and P. Leprince. Validity of actinometry to monitor oxygen atom concentration in microwave discharges created by surface wave in  $O_2 - N_2$  mixtures. *J. Appl. Phys.*, 75:104, 1994.
- [27] T. Mehdi, P. B. Legrand, J. P. Dauchot, M. Wautelt, and M. Heeq. Optical emission diagnostics of an rf magnetron sputtering discharge. *Spectrochim. Acta B*, 48B:1023, 1993.
- [28] W. L. Wiese, W. M. Smith, and B. M. Miles. *Atomic Transition Probabilities National Standard Reference Data Series*, chapter Vol 2, chpt 2. National Bureau of Standards, Washington D.C., 1969.
- [29] P. V. Feltsan. *Ukr. Fiz. Zh.*, 12:1423, 1967.
- [30] I. P. Zapesochnyi and P. V. Feltsan. On the excitation cross sections of 2p levels of argon, krypton, and xenon. *Opt. Spectrosc.*, 20:291, 1966.
- [31] J. K. Ballou, C. C. Lin, and F. E. Fajen. Electron-impact excitation of argon atoms. *Phys. Rev. A*, 8:1797, 1973.
- [32] R. E. Walkup, K. L. Saenger, and G. S. Selwyn. Studies of atomic oxygen in  $O_2 + CF_4$  rf discharges by two-photon laser-induced fluorescence and optical emission spectroscopy. *J. Chem. Phys.*, 84:2668, 1986.



- [33] T. Sawada and P. S. Ganas. Distorted-wave calculation of electron-impact excitation of atomic oxygen. *Phys. Rev. A*, 7:617, 1973.
- [34] G. M. Lawrence. Dissociative excitation of some oxygen-containing molecules: lifetimes and electron impact cross sections. *Phys. Rev. A*, 2:397, 1970.
- [35] C. J. Mogab, A. C. Adams, and D. L. Flamm. Plasma etching of *Si* and *SiO<sub>2</sub>* the effect of oxygen additions to *CF<sub>4</sub>* plasmas. *J. Appl. Phys.*, 49(7):2668, 1978.
- [36] S. Samukawa. Highly selective and highly anisotropic *SiO<sub>2</sub>/Si* etching in pulse-time modulated electron cyclotron resonance plasma. *Jpn J. Appl. Phys.*, 33:2133, 1994.
- [37] K. S. Shin, K. K. Chi, C. J. Kang, C. Jung, C. O. Jung, J. T. Moon, and M. Y. Lee. Enhancement of mask selectivity in *SiO<sub>2</sub>* etching with a phase-controlled pulsed inductively coupled plasma. *Jpn J. Appl. Phys.*, 37:2349, 1998.
- [38] G. S. Hwang and K. P. Giapis. Mechanism of charging reduction in pulsed plasma etching. *Jpn J. Appl. Phys.*, 37:291, 1998.
- [39] N. Fujiwara, T. Maruyama, and H. Miyatake. Influence of pulsed electron cyclotron resonance plasma on gate electrode etching. *Jpn J. Appl. Phys.*, 37:2302, 1998.
- [40] L. J. Overzert, J. H. Beberman, and J. T. Verdeyen. Enhancement of the

- negative ion flux to surfaces from radio frequency processing discharges. *J. Appl. Phys.*, 66:1622, 1989.
- [41] J. P. Booth and N. Sadeghi. Oxygen and fluorine atom kinetics in electron cyclotron resonance plasmas by time-resolved actinometry. *J. Appl. Phys.*, 70:611, 1991.
- [42] A. Kono. Temporal behaviour of the electron and negative ion densities in a pulsed radio-frequency  $CF_4$  discharge. *J. Appl. Phys.*, 70:2939, 1991.
- [43] S. Ashida, M. R. Shim, and M. A. Lieberman. Measurements of pulsed-power modulated argon plasmas in an inductively coupled plasma source. *J. Vac. Sci. Technol. A*, 14:391, 1996.
- [44] M. A. Lieberman and S. Ashida. Global models of pulse-power-modulated high-density, low-pressure discharges. *Plasma Sources Sci. Technol.*, 5:145, 1996.
- [45] L. J. Overzet and J. Kleber. Time resolved measurements of pulsed discharges: the role of metastable atoms in the afterglow. *Presented at NATO Advanced Research Workshop on Electron Kinetics in Plasmas (St Petersburg, 1997)*.
- [46] S. P. Fusselman and H. K. Yasuda. Spatial distributions of electron density and temperature in audio frequency and radio frequency magnetron glow discharges. *J. Vac. Sci. Technol. A*, 12:3115, 1994.
- [47] B. A. Boegger and A. Bulliard. Double probe circuit used in pulsed plasma diagnostics. *Rev. Sci. Instrum.*, 51:735-7, 1980.
- [48] B. A. Smith and L. J. Overzet. Improvements to the floating double probe

- for time-resolved measurements in pulsed rf plasmas. *Rev. Sci. Instrum.*, 69:1372, 1998.
- [49] B. A. Smith and L. J. Overzet. Observation of the ion-ion transition in an  $SF_6$  discharge using a fast floating double probe. *Plasma Sources Sci. Technol.*, 8:82–90, 1999.
- [50] N. Hershkowitz. *How Langmuir Probes Work-Plasma Diagnostics Discharge Parameters and Chemistry*, chapter 113-83. Academic, New York, 1989.
- [51] X. Tang, C. A. Nichols, and D. M. Manos. Stripping and cleaning of photoresist using low energy neutrals. *J. Appl. Phys.*, 86:2419, 1999.
- [52] D. M. Manos, J. L. Cecchi, C. W. Cheah, and H. F. Dylla. Diagnostics of low temperature plasmas: the electron component. *Thin Solid Films*, 195:319–336, 1991.
- [53] R. Budny and D. Manos. Particle and heat flux measurements in *PDX* edge plasmas. *J. Nucl. Mater.*, 121:41–7, 1984.
- [54] D. M. Manos, R. V. Budny, S. Kilpatrick, P. Stangeby, and S. Zweben. Probes for edge plasma studies of *TFTR* (invited). *Rev. Sci. Instrum.*, 57:2107, 1986.
- [55] C. W. Cheah. *Plasma diagnostics for the characterization of etching and deposition reactors*. PhD thesis, Princeton University, Princeton, NJ, 1993.
- [56] C. Lee and M. A. Lieberman. Global model of  $Ar$ ,  $O_2$ ,  $Cl_2$ , and  $Ar/O_2$  high-density plasma discharges. *J. Vac. Sci. Technol. A*, 13:368, 1995.
- [57] S. Ashida, C. Lee, and M. A. Lieberman. Spatially averaged (global) model

- of time modulated high density argon plasmas. *J. Vac. Sci. Technol. A*, 13:2498, 1995.
- [58] H. Sugai and K. Nakamura. Diagnostics and control of radicals in an inductively coupled etching reactor. *J. Vac. Sci. Technol. A*, 13:887, 1995.
- [59] P. N. Wainman, M. A. Lieberman, and A. J. Lichtenberg. Characterization at different aspect ratios(radius/length) of a radio frequency inductively coupled plasma source. *J. Vac. Sci. Technol. A*, 13:2464, 1995.
- [60] J. B. Caughman. *The distribution of ion energies incident on an ICRH antenna Farady shield*. PhD thesis, University of Illinois at Urbana-Champaign, Urban-Champaign, IL, 1989.
- [61] J. D. Swift and M. J. R. Schwar. *Electrical probes for plasma diagnostics*. American Elsevier, London, 1969.
- [62] M. P. Chung, L. Talbot, and J. K. Touryan. *Electric Probes in Stationary and Flowing Plasma*. Springer, New York, 1975.
- [63] J. Hopwood, C. R. Guarnier, and J. J. Cuomo. Langmuir probe measurements of a radio frequency induction plasma. *J. Vac. Sci. Technol. A*, 11:152, 1993.
- [64] K. N. Ruzic and J. L. Wilson. Time-resolved electric probe techniques in radio frequency plasmas. *J. Vac. Sci. Technol. A*, 8:3746, 1990.
- [65] J. L. Wilson, J. B. O. Caughman, P. L. Nguyen, and D. N. Ruzic. Measurements of time varying plasma potential temperature, and density in a 13.56MHz radio-frequency discharge. *J. Vac. Sci. Technol. A*, 7:972, 1989.
- [66] T. I. Cox, V. G. Deshmukh, D. A. Hope, A. J. Hydes, N. St. J. Braithwaite,

- and N. P. Benjamin. The use of Langmuir probes and optical emission spectroscopy to measure electron energy distribution functions in rf-generated argon plasmas. *J. Phys. D:Appl. Phys.*, 20:820, 1987.
- [67] J. T. Gudmundsson, T. Kimura, and M. A. Lieberman. Experimental studies of  $O_2/Ar$  plasma in a planar inductive discharge. *Plasma Sources Sci. Technol.*, 8:22–30, 1992.
- [68] F. W. Crawford. Modulated Langmuir probe characteristics. *J. Appl. Phys.*, 34:1897, 1963.
- [69] B. E. Cherrington. The use of electrostatic probes for plasma diagnostics—a review. *Plasma Chem. Plasma Process.*, 2:113–40, 1982.
- [70] J. A. Stittsworth and A. E. Wendt. Reactor geometry and plasma uniformity in a planar inductively coupled radio frequency argon discharge. *Plasma Sources Sci. Technol.*, 5:429–35, 1996.
- [71] V. A. Godyak and R. B. Piejak. Probe measurements of the space potential in a radio frequency discharge. *J. Appl. Phys.*, 68:3157, 1990.
- [72] N. St. J. Braithwaite, N. M. Benjamin, and J. E. Allen. An electrostatic probe technique for rf plasma. *J. Phys. E:Sci. Instrum.*, 20:1046, 1987.
- [73] N. St. J. Braithwaite, P. N. Benjamin, and J. E. Allen. *Proc. Int. Symp. Plasma Chemistry(Eindhoven)*, 2(IUPAC):564, 1985.
- [74] C. Lai, R. A. Breun, P. W. Sandstrom, A. E. Wendt, N. Hershkowitz, and R. C. Woods. Langmuir probe measurements of electron temperature and density

- scaling in multidipole radio frequency plasmas. *J. Vac. Sci. Technol. A*, 11:1199, 1993.
- [75] A. P. Paranjpe, J. P. McVitte, and S. A. Self. A tuned Langmuir probe for measurements in rf flow discharges. *J. Appl. Phys.*, 67:6718, 1990.
- [76] J. G. Laframboise. *Report 100 Institute of Aerospace Studies, University of Toronto*, 1966.
- [77] J. R. Sanmartin and R. E. Estes. The orbital-motion-limited regime of cylindrical langmuir probes. *Phys. Plasmas*, 6:395, 1999.
- [78] J. E. Allen, R. F. Boyd, and P. Reynolds. The collection of positive ions by a probe immersed in a plasma. *Proc. Phys. Soc. B*, 70:297, 1957.
- [79] F. F. Chen. Numerical computations for ion probe characteristic in a collisionless plasma. *Plasma Phys.*, 7:47, 1965.
- [80] A. E. Wendt and W. N. G. Hitchon. Electron heating by sheaths in radio frequency discharges. *J. Appl. Phys.*, 71:4718, 1992.
- [81] V. A. Godyak, R. B. Piejak, and N. Sternberg. A comparison of rf electrode sheath models. *IEEE Trans. Plasma Sci.*, 21:378, 1993.
- [82] V. A. Godyak and N. Sternberg. Dynamical model of the electrode sheaths in symmetrically driven rf discharge. *Phys. Rev. A*, 42:2299, 1990.
- [83] M. A. Lieberman. Analytical solution for capacitive rf sheath. *IEEE Trans. Plasma Sci.*, 16:638, 1988.
- [84] D. N. Ruzic. Electric probes for low temperature plasmas. *Am. Vac. Soc. Monograph*, pages M-13, 1994.

- [85] G. Ding, J. E. Schlarer, and K. L. Kelly. Effects of rapidly decaying plasmas on langmuir probe measurements. *J. Appl. Phys.*, 84:1236, 1998.
- [86] R. M. Clements. Plasma diagnostics with electric probes. *J. Vac. Sci. Technol. A*, 15:193, 1978.
- [87] A. Brockhaus, C. Borchardt, and J. Engemann. Langmuir probe measurements in commercial plasma plants. *Plasma Sources Sci. Technol.*, 3:539, 1994.
- [88] H. B. Valentini, E. Glauche, and D. Wolff. Modelling of sheaths, presheaths, current-voltage characteristics and double probes in low-pressure plasmas in coaxial and concentric geometries. *Plasma Sources Sci. Technol.*, 4:353–65, 1995.
- [89] C. M. Nairn, B. M. Annaratone, and J. E. Allen. Theory of double probes in the absence of ion saturation. *Plasma Sources Sci. Technol.*, 4:416, 1995.
- [90] D. M. Manos, P. C. Stangeby, R. V. Budny, S. A. Cohen, S. Kilpatrick, and T. Satake. Studies of the edge plasma of rf heated *PLT* discharges. *J. Nucl. Mater.*, 129:319–24, 1984.
- [91] B. M. Annaratone, M. W. Allen, and J. E. Allen. Ion currents to cylindrical langmuir probes in rf plasmas. *J. Phys. D: Appl. Phys.*, 25:417–24, 1992.
- [92] B. M. Annaratone, G. F. Counsell, H. Kawano, and J. E. Alle. On the use of double probes in rf discharges. *Plasma Sources Sci. Technol.*, 1:232–41, 1992.
- [93] E. O. Johnson and L. Malter. A floating double probe method for measurements in gas discharges. *Phys. Rev.*, 80:58, 1950.

- [94] E. O. Peterson and L. Talbot. Collisionless electrostatic single-probe and double-probe measurements. 8:2215, 1970.
- [95] A. Yokozawa, H. Ohtake, and S. Samukawa. Simulation of a pulse time-modulated bulk plasma in  $Cl_2$ . *Jpn J. Appl. Phys.*, 35:2433, 1996.
- [96] J. A. Meyer and A. E. Wendt. Measurements of electromagnetic fields in a planar radio-frequency inductively coupled plasma sources. *J. Appl. Phys.*, 78:90, 1995.
- [97] A. E. Wendt. The physics of inductively coupled plasma sources. *AIP Conf. Proc.*, 403:435, 1997.
- [98] T. H. Ahn, K. Nakamura, and H. Sugai. A new technology for negative ion detection and the rapid electron cooling in a pulsed high-density etching plasma. *Jpn J. Appl. Phys.*, 34(2):L1405, 1995.
- [99] W. H. Press, S. A. Teukolsky, W. T. Vetterling, and B. P. Flannery. *Numerical Recipes - the Art of Scientific Computing*. Cambridge University, University of Cambridge, 1992.
- [100] J. O. Hirschfelder, C. F. Curtiss, and R. B. Bird. *Molecular Theory of Gases and Liquids*. Wiley, New York, 1954.
- [101] W. Kern. Radiochemical study of semiconductor surface contamination. *RCA Rev.*, 31(2):655, 1973.
- [102] H. Myers. Analysis of electron swarm experiments in oxygen. *J. Phys. B*, 2:393, 1969.



- [103] The national technology roadmap for semiconductors. Semiconductor Industry Association(SEMATECH, Austin, TX), 1997.
- [104] K. P. Giapis and T. A. Morre. Hyperthermal neutral beam etching. *J. Vac. Sci. Technol. A*, 13:959, 1995.
- [105] K. B. Matsuo and G. S. Oehrlein. Sematech report, no.95092964a-min, 1995.
- [106] W. E. Mlynko, S. R. Kasi, and K. M. Manos. Oxide degradaton effects in dry patterning of resist using neutral beams. *Mater. Res. Soc. Symp. Proc.*, 268:41, 1992.
- [107] J. Cross, S. L. Koontz, J. C. Gregory, and M. J. Edgell. *Hyperthermal atomic oxygen reactions with kapton and polyethylene Plasma Diagnostics Discharge Parameters and Chemistry*. The Minerals, Metals and Materials Society, pp1-14, Milwaukee, 1990.
- [108] S. T. Ceyer. New mechanisms for chemistry at surfaces. *Science*, 294:133, 1990.
- [109] A. Ananda. *Propagation of Rayleigh waves in thin films*. PhD thesis, The College of William and Mary, Williamsburg, VA, 1997.
- [110] D. M. Manos and J. M. Parson. Crossed molecular beam study of chemiluminescent reactions of group *IIIb* atoms with oxygen. *J. Chem. Phys.*, 63:3575, 1975.
- [111] J. B. Cross, M. Hoffbauer, T. K. Minton, K. P. Giapis, G. P. Kota, J. W. Coburn, and D. B. Graves. *SEMATECH report No.95062863A-ENG*. Sematech, TX, 1995.

- [112] K. P. Giapis and T. K. Minton. *SEMATECH report No.95062879A-MIN*. Sematech, TX, 1995.
- [113] J. B. Cross and N. C. Blairs. *Rarefied Gas Dynamics: Space-related Studies*, edited by E. P. Muntz, D. P. Weaver, and D. H. Campbell, *Progress in Astronautics and Aeronautics*. 1989.
- [114] D. B. Oakes, R. H. Krech, B. L. Upschulte, and G. E. Caledonia. Oxidation of polycrystalline silver films by hyperthermal oxygen atoms. *J. Appl. Phys.*, 77:2166, 1995.
- [115] M. R. Carruth, R. F. DeHaye, J. K. Norwood, and A. F. Whitaker. Method for determination of neutral atomic oxygen flux. *Rev. Sci. Instrum.*, 61:1211, 1990.
- [116] S. R. Cook, M. A. Hoffbauer, and J. B. Cross. A specialized torsion balance designed to measure the absolute flux density of hyperthermal molecular beams containing reactive species. *Rev. Sci. Instrum.*, 67:1781, 1996.
- [117] S. R. Cook. *Molecular Beam Measurements of Absolute Momentum Accommodation of Spacecraft Surfaces using a specialized Torsion Balance*. PhD thesis, University of Texas-Austin, Austin, TX, 1995.
- [118] D. M. Manos, T. Bennett, M. Herzer, and J. Schwarzmann. Laboratory studies of spectroscopic markers for the characterization of erosion by plasmas. *J. Nucl. Mater.*, 196-198:933, 1992.
- [119] C. T. Gabriel and Y. Melaku. Gate oxide damage in a high density inductively coupled plasma. *J. Vac. Sci. Technol. B*, 12:454, 1994.

- [120] A. K. Stamper, J. B. Lasky, and J. W. Adkisson. Plasma-induced gate-oxide charging issues for sub-0.5 $\mu\text{m}$  complementary metal-oxide-semiconductor technologies. *J. Vac. Sci. Technol. A*, 13:905, 1995.
- [121] H. Kim, W. Nam, G. Yeom, H. Lee, J. Kim, and K. Whang. Study of radiation damage and contamination by magnetized inductively coupled plasma etching. *J. Vac. Sci. Technol. A*, 14:1062, 1996.
- [122] D. Park and C. Hu. Plasma charging damage on ultrathin gate oxides. *IEEE Electron Device Letters.*, 19:1, 1998.
- [123] W. Lukaszek. *1997 2nd International Symposium on Plasma Process-Induced Damage*. American Vacuum Society, Monterey, CA, 1997.
- [124] S. Ma and J. McVittie. Effect of wafer temperature during plasma exposure on charging damage. *J. Vac. Sci. Technol. B*, 14:566, 1996.
- [125] S. Ma, J. McVittie, and K. Saraswat. Prediction of plasma charging induced gate oxide damage by plasma charging probe. *IEEE Electron Device Letters.*, 18:468, 1997.
- [126] K. Nauka, J. Theil, and J. Lagowski. *1997 2nd International Symposium on Plasma Process-Induced Damage*. American Vacuum Society, Monterey, CA, 1997.
- [127] K. Pangal. *1997 2nd International Symposium on Plasma Process-Induced Damage*. American Vacuum Society, Monterey, CA, 1997.
- [128] S. Fang and J. P. McVittie. Thin-oxide damage from gate charging. *IEEE Electron Device Letters.*, 13:288, 1992.

- [129] S. Fang and J. P. McVittie. A model and experiments for thin oxide damage from wafer charging in magnetron plasmas. *IEEE Electron Device Letters.*, 13:347, 1992.
- [130] W. En, B. P. Linder, and N. W. Cheung. Modeling of oxide charging effects in plasma processing. *J. Vac. Sci. Technol. B*, 14:552, 1996.
- [131] S. Samukawa. Dependence of gate oxide breakdown frequency on ion current density distributions during election cyclotron resonance plasma etching. *Jpn J. Appl. Phys.*, 30:L1902, 1991.
- [132] S. Samukawa. Damage caused by stored charge during ecr plasma etching. *Jpn J. Appl. Phys.*, 29:980, 1990.
- [133] C. Chein, C. Chang, H. Lin, S. Chiou, T. Huang, T. Chang, and S. Hsien. The role of resist for ultrathin gate oxide degradation during  $O_2$  plasma ashing. *IEEE Electron Device Letters.*, 18:203, 1997.
- [134] C. Chein, C. Chang, H. Lin, S. Chiou, T. Huang, T. Chang, and S. Hsien. Resist-related damage on ultrathin gate oxide during plasma ashing. *IEEE Electron Device Letters.*, 18:33, 1997.
- [135] V. Vahedi, N. Benjamin, and A. Perry. *1997 2nd International Symposium on Plasma Process-Induced Damage*. American Vacuum Society, Monterey, CA, 1997.
- [136] G. S. Hwang and K. P. Giapis. Mechanism of charging reduction in pulsed plasma etching. *Jpn J. Appl. Phys.*, 37:2291, 1998.
- [137] T. Tatsumi, S. Fukuda, and S. Kadomura. Radiation damage of  $SiO_2$  surface

induced by vacuum ultraviolet photons of high-density plasma. *Jpn J. Appl. Phys.*, 33:2175, 1994.

- [138] J. P. McVittie. *1997 2nd International Symposium on Plasma Process-Induced Damage*. American Vacuum Society, Monterey, CA, 1997.
- [139] C. T. Gabriel. Gate oxide damage: Testing approaches and methodologies. *J. Vac. Sci. Technol. A*, 17:1494, 1999.
- [140] C. T. Gabriel. Gate oxide damage from polysilicon etching. *J. Vac. Sci. Technol. B*, 9:370, 1991.
- [141] B. Li, L. Cao, and J. H. Zhao. Evaluation of damage induced by inductively coupled plasma etching of 6h-sic using au schottky barrier diodes. *Applied Physics Letter*, 73:653, 1998.
- [142] S. Savas. *1996 1nd International Symposium on Plasma Process-Induced Damage*. American Vacuum Society, Santa Clara, CA, 1996.
- [143] T. Brozek. Comparison of damage created by a chemical downstream etcher and plasma-immersion system in metal-oxide-semiconductor capacitor. *J. Vac. Sci. Technol. B*, 14:577, 1996.
- [144] C. B. Brooks, M. J. Buie, and K. J. Vaidya. Plasma process induced surface damage removal. *J. Vac. Sci. Technol. A*, 16:260, 1998.
- [145] W. Nam, G. Yeom, J. Kin, K. Whang, and J. Yoon. Physical damage and contamination by magnetized inductively coupled plasmas and effects of various cleaning and annealing methods. *J. Vac. Sci. Technol. A*, 15:590, 1997.

- [146] M. Matsui, F. Uchida, M. Kojima, K. Yamazaki, K. Katsuyama, and H. Arai. in-situ after-treatment using low-energy dry-etching with a  $CF_4 - O_2$  gas mixture to remove reactive ion etching damage. *Jpn J. Appl. Phys.*, 37:2330, 1998.
- [147] S. Sakamori, T. Maruyama, N. Fujiwara, and H. Miyatake. Effect of electron shading on gate oxide degradation. *Jpn J. Appl. Phys.*, 37:2321, 1998.
- [148] N. Fujiwara, T. Maruyama, and M. Yoneda. Pulsed plasma processing for reduction of profile distortion induced by charge buildup in electron cyclotron resonance plasma. *Jpn J. Appl. Phys.*, 35:2450, 1996.
- [149] M. J. Goecker, T. K. Bennett, J. Park, Z. Wang, and S. A. Cohen. *1997 2nd International Symposium on Plasma Process-Induced Damage*. American Vacuum Society, Monterey, CA, 1997.
- [150] T. Yunogami, Y. Yajima, and T. Mizutani. Radiation damage in  $SiO_2/Si$  induced by low-energy electrons via plasmon excitation. *J. Appl. Phys.*, 73:8184, 1993.
- [151] K. Yokogawa, Y. Yajima, and T. Mizutani. Mechanism of  $E'$  center generation in  $SiO_2$  film by ion and neutral beam bombardment. *Jpn J. Appl. Phys.*, 30:3199, 1991.
- [152] T. Mizutani, S. Nishimatsu, and T. Yunogami. *Mater. Res. Soc. Symp. Proc.*, 128:605, 1989.
- [153] T. Ono, N. Itabashi, I. Ochiai, S. Yamamoto, and K. Mochiji. Positive charge

- generation at  $SiO_2/Si$  interface due to bombardment with metastable atoms. *Jpn J. Appl. Phys.*, 36:6718, 1997.
- [154] T. Mizutani and S. Nishimatsu. Generation of low-energy neutral beams and radiation damage of  $SiO_2/Si$  by neutral bombardment. *J. Vac. Sci. Technol. B*, 7:547, 1989.
- [155] T. P. Ma and P. V. Dressendorfer. *Ionizing Radiation Effects in MOS Devices and Circuits*. Wiley Interscience, New York, 1989.
- [156] T. Yunogami, T. Mizutani, K. Suzuki, and S. Nishimatsu. Mechanism of radiation damage in  $SiO_2/Si$  induced by vuv photons. *Jpn J. Appl. Phys.*, 28:2172, 1989.
- [157] L. Onsager. Initial recombination of ions. *Phys. Rev.*, 54:554, 1938.
- [158] G. A. Ausman. *Harry Diamond Laboratories Report No.2097*. Harry Diamond Laboratories, Adelphi,MD, 1986.
- [159] J.R.Woodworth, M. G. Blain, R. L. Jarecki, T. W. Hamilton, and B. P. Aragon. Absolute intensities of the vacuum ultraviolet spectra in a metal-etch plasma processing discharge. *J. Vac. Sci. Technol. A*, 17:3209, 1999.
- [160] X. Tang and D. M. Manos. Optical emission studies and neutral stream characterization of a surface reflection materials processing source. *J. Vac. Sci. Technol. A*, July,2000, in press.
- [161] X. Tang, Q. Wang, and D. M. Manos. Process damage assessment of a low energy neutral stream source. *J. Vac. Sci. Technol. B*, May, 2000, in press.
- [162] X. Tang, Q. Wang, and D. M. Manos. *1999 4th International Symposium on*

*Plasma Process-Induced Damage*. American Vacuum Society, Monterey, CA, 1999.

- [163] X. Tang and D. M. Manos. Time-resolved electrostatic probe studies of a pulsed argon plasma. *Plasma Sources Sci. Technol.*, 8:594, 1999.



# Vita

Xianmin Tang

Xianmin was born in Wuhan city in People's Republic of China on 12/10/69. He graduated with a M.S. degree in Materials Science and Engineering at Huazhong University of Science and Technology in May, 1994. After one years of teaching in Department of Physics at Wuhan University, he entered Applied Science program at College of William and Mary in August,1995. He will start a process engineer position in Applied Materials in June 2000.